Two-photon absorption based detection in semiconductor microcavities

by

John O'Dowd

Thesis submitted for the degree of Doctor in Philosophy

under the supervision of
Prof. John F. Donegan

School of Physics
Trinity College Dublin

April, 2009

Declaration

I declare that the work in this thesis has not been previously submitted as an exercise for a degree to this or any other university.

The work described herein is entirely my own, except for the assistance mentioned in the acknowledgements and collaborative work mentioned in the list of publications.

I agree that Trinity college library may lend or copy this thesis upon request.

For my parents, and grandparents

A lot done, a lot more to do.

Bertie Ahern

Abstract

The most important feature of a two-photon absorption microcavity (TPAM) is that of its enhancement of the optical field which enhances the level of two-photon absorption (TPA) for a particular input optical power incident on the detector. The TPAM is shown to not only enhance the level of TPA but also to suppress the level of residual single photon absorption (SPA) relative to the level of TPA. This allows a TPA dominated signal to be accessed at much lower incident optical powers than would be possible for a similar GaAs absorbing region which was not sandwiched between two highly reflective distributed Bragg reflectors (DBR's). The TPA coefficient is estimated to be approximately 15 cm/GW at 1560 nm in (001) GaAs. The residual SPA coefficient in the unintentionally doped GaAs active layer of the TPAM (which is grown by metal-organic chemical vapour deposition) is approximately 1.0×10^{-4} cm^{-1}.

Even with the enhancement provided by the TPAM it is still necessary to focus the input beam onto the TPAM in order to operate in the TPA dominated absorption regime at low optical input powers. A TPAM has a limited acceptance angle and so different angular components have different levels of enhancement in the cavity. For a TPAM, this results in an asymmetrical cavity spectral response and also an asymmetrical response to the focus position of the input signal. The influence of the acceptance angle on the TPAM means that to optimize the level of TPA generated in a TPAM, the optimal spot size for the microcavity must be calculated. An optimised incident focused spot diameter of 7 μm has been calculated as being the optimal value for maximising the generated TPA photocurrent for the $R = 0.956$ (R = average cavity reflectivity) TPAM under test. The theory described allows for the calculation of an optimal incident focused spot size for cavities with different cavity reflectivities. With increasing microcavity cavity reflectivity the dependence on incident angle becomes increasingly important and as such the optimal incident spot size will increase.

The polarisation dependence of a TPAM has been investigated. The deviation in the dependence of the detector response from that of bulk GaAs is shown to be due to the birefringence of the cavity. A theoretical model based on the convolution of the cavity birefringence and the polarisation dependence of TPA in GaAs is described and shown to match the measured polarisation dependence of the TPAM very well.

The level of TPA generated by polarised band limited amplified spontaneous emission (BL-ASE) noise has been shown analytically and experimentally to have the same mean power dependence as an on-off modulated signal with a generalised duty cycle equal to 50 %. A simple formula is derived which describes the TPA dependence on the optical signal to noise ratio (OSNR) for an optically amplified signal with polarised BL-ASE noise. The theory was validated by carrying out an OSNR measurement using a TPAM and the theory was shown to fit the measured data very well.

TPA based optical channel identification is demonstrated as being capable of differentiating between different types of signals as well as between different signals and BL-ASE. Also shown in chapter 8 is that a TPAM can easily be tuned across a 5 nm range by changing the temperature from 10 to 50 ^{0}C. Furthermore, it is shown that unlike Silicon avalanche photodiodes (APDs) a TPAM is be highly stable with varying temperature as only the resonant wavelength of the detector changes. Using temperature tuning it will be possible to monitor a dense wavelength division multiplexed (DWDM) system across the entire C band using approximately 3-4 detectors at fixed angles and then temperature tuning each device to pick out individual channels. While the temperature control circuit demonstrated in this thesis allowed only a relatively narrow temperature tuning range of just over 40 ^{0}C, lasers in modern networks commonly operate from -40 ^{0}C to 85 ^{0}C. This increased tuning range would allow the single TPA microcavity device discussed above to be tuned thermally by > 15 nm.

Publications and presentations

1. P. Maguire, L. P. Barry, T. Krug, J. O'Dowd, M. Lynch, A. L. Bradley, J. F. Donegan, and H. Folliot, "Direct measurement of a high-speed (>100Gbit/s) OTDM data signal utilising two-photon absorption in a semiconductor microcavity," in Lasers and Electro-Optics Society. LEOS, 2005), 142-143.
2. T. Krug, W. H. Guo, J. O'Dowd, M. Lynch, A. L. Bradley, J. F. Donegan, P. J. Maguire, L. P. Barry, and H. Folliot, "Resonance tuning of two-photon absorption microcavities for wavelength-selective pulse monitoring," IEEE Photon. Technol. Lett. 18, 433-435 (2006).
3. P. Maguire, K. Bondarczuk, L. P. Barry, J. O'Dowd, W. H. Guo, M. Lynch, A. L. Bradley, J. F. Donegan, and H. Folliot, "Dispersion monitoring for high-speed WDM networks via two-photon absorption in a semiconductor microcavity," in ICTON, 2006),
4. J. O'Dowd, W. H. Guo, M. Lynch, A. L. Bradley, and J. F. Donegan, "Investigation of residual Single Photon Absorption in Two Photon Absorption Semiconductor Microcavities," in ISOPL, 2006),
5. P. J. Maguire, L. P. Barry, T. Krug, W. H. Guo, J. O'Dowd, M. Lynch, A. L. Bradley, J. F. Donegan, and H. Folliot, "Optical signal processing via two-photon absorption in a semiconductor microcavity for the next generation of high-speed optical communications network," J. Lightwave Technol. 24, 2683-2692 (2006).
6. K. Bondarczuk, P. J. Maguire, L. P. Barry, J. O'Dowd, W. H. Guo, M. Lynch, A. L. Bradley, J. F. Donegan, and H. Folliot, "Chromatic dispersion monitoring of 80-Gb/s OTDM data signal via two-photon absorption in a semiconductor microcavity," IEEE Photon. Technol. Lett. 19, 21-23 (2007).
7. W. H. Guo, J. O'Dowd, M. Lynch, A. L. Bradley, J. F. Donegan, and L. P. Barry, "Influence of cavity lifetime on high-finesse microcavity two-

photon absorption photodetectors," IEEE Photon. Technol. Lett. 19, 432-434 (2007).

8. F. Smyth, J. O'Dowd, D. C. Kilper, J. E. Simsarian, L. P. Barry, B. Roycroft, and B. Corbett, "10Gbit/s modulation of a fast switching slotted fabry-parot tunable laser," in Lasers and Electro-Optics, and the International Quantum Electronics Conference. CLEOE-IQEC. European Conference on, 2007), 1-1.
9. J. O'Dowd, D. C. Kilper, W. H. Guo, J. F. Donegan, and S. Chandrasekhar, "Optical channel monitoring using two photon absorption," in Lasers and Electro-Optics, and the International Quantum Electronics Conference. CLEOE-IQEC. European Conference on, 2007), 1-1.
10. K. Bondarczuk, P. J. Maguire, L. P. Barry, J. O'Dowd, W. H. Guo, M. Lynch, A. L. Bradley, J. F. Donegan, and H. Folliot, "Wavelength tuneable pulse monitoring using a two-photon-absorption microcavity," in Lasers and Electro-Optics, and the International Quantum Electronics Conference. CLEOE-IQEC. European Conference on, 2007), 1-1.
11. J. O'Dowd, W. H. Guo, E. Flood, M. Lynch, A. L. Bradley, J. F. Donegan, and L. P. Barry, "Temperature tuning of two-photon absorption microcavity photodetectors for wavelength selective pulse monitoring," Electron. Lett. 44, 989-991 (2008).
12. W. H. Guo, J. O'Dowd, E. Flood, T. Quinlan, M. Lynch, A. L. Bradley, J. F. Donegan, K. Bondarczuk, P. J. Maguire, and L. P. Barry, "Suppression of residual single-photon absorption relative to two-photon absorption in high finesse planar microcavities," IEEE Photon. Technol. Lett. 20, 1426-1428 (2008).
13. W. H. Guo, J. O'Dowd, M. Lynch, A. L. Bradley, J. F. Donegan, L. P. Barry, and D. C. Kilper, "Two-photon absorption generated by optically amplified signals," Electron. Lett. 44, 1087-1088 (2008).
14. J. O'Dowd, W. H. Guo, E. Flood, M. Lynch, A. L. Bradley, L. P. Barry, and J. F. Donegan, "Polarization dependence of a GaAs-based two-photon

absorption microcavity photodetector," Opt. Express 16, 17682-17688 (2008).

15. K. Bondarczuk, P. J. Maguire, L. P. Barry, J. O'Dowd, W. H. Guo, M. Lynch, A. L. Bradley, and J. F. Donegan, "High-speed chromatic dispersion monitoring of a two-channel WDM system using a single TPA microcavity," in Lasers and Electro-Optics, Conference on Quantum Electronics and Laser Science. CLEO/QELS. Conference on, 2008), 1-2.
16. J. O'Dowd, W. H. Guo, E. Flood, M. Lynch, A. L. Bradley, and J. F. Donegan, "Influence of acceptance angle on high-finesse microcavity two photon absorption photodetectors," in Photon08, 2008), MD-7881-7104.
17. J. O'Dowd, W. H. Guo, E. Flood, M. Lynch, A. L. Bradley, and J. F. donegan, "Generalized description of polarization dependence of two-photon absorption detectors," in Photon08, 2008), MD-7881-7115.
18. J. O'Dowd, W. H. Guo, E. Flood, M. Lynch, A. L. Bradley, and J. F. donegan, "Influence of acceptance angle of high-finesse microcavity two-photon absorption photodetectors," in ICPS, 2008), TH-PD3-146.
19. J. O'Dowd, W. H. Guo, E. Flood, M. Lynch, A. L. Bradley, and J. F. Donegan, "Polarization characterization of a two-photon absorption microcavity detector," in ICPS, 2008), Th-PD3-141.

Acknowledgements

I would like to thank Prof. J. F. Donegan for suggesting this work and for giving me the opportunity to join his group. His support over the course of my PhD has made all of this work possible.

Thanks to Dr. T. Krug for his help familiarising me with the labs during the first few months of my PhD as well as to Mr. E. Flood and Mr. T. Quinlan for their help during the final few months.

This work on a day to day basis has been carried out with the continuing support of Dr. W. H. Guo. His help in all areas of this work, both experimental and theoretical could not be more appreciated. His tolerance with my never ending barrage of questions has been astonishing.

Thanks to Dr. L. Bradley and M. Lynch for their suggestions and assistance during the course of this work.

I would like to thank Alcatel-Lucent for allowing me to spend time in Bell Labs in Crawford Hill. I am especially thankful to Dr. D. C. Kilper for inviting me to work in his labs. His suggestions have been very useful and without him large segments of this work would not have been possible. I am also appreciative of all the help I received while in Bell, especially from Dr. M. Dinu and Dr. R. Giles.

Many thanks to all the members of the "semiconductors photonics group" with special thanks to Dr. V. Weldon for his technical support. To all the group members who have made my time in the group more enjoyable.

Special thanks to the Dr. L. P. Barry, Dr. P. Maguire, K. Bondarczuk and F. Smyth and all the members of R.I.N.C.E. for all there assistance.

To my friends in Trinity over the years, some of which have stayed for the long haul, especially Niall, Chris, Yenny and Diarmuid. To the guys I have played soccer with over the years in college thanks for the much appreciated distraction and escape from the lab.

Thanks to my friends from outside college, especially Fiona, Oisin and Dermot. Thanks also to my friends in the U.S. who made my stay all the more enjoyable, especially Elizabeth and John.

Finally thanks to my parents and to my brothers and sister Alan, David and Aisling.

Contents

Abbreviations

APD	Avalanche photodiode
ASE	Amplified spontaneous emission
BL-ASE	Band-limited amplified spontaneous emission
BPF	Band pass filter
CW	Continuous wave
DPSK	Differential phase shift keying
DWDM	Dense wavelength division multiplexing
EDFA	Erbium doped fiber amplifier
FPE	Fabry-Perot etalon
FWHM	Full width at half maximum
NRZ	Non-return to zero
OOK	On-off keyed
OPM	Optical performance monitoring
OSA	Optical spectrum analyser
OSNR	Optical signal to noise ratio
PA	Polarisation controller
PD	Photodetector (average power meter)
PRBS	Pseudo random binary sequence
RZ	Return to zero
SHG	Second harmonic generation
SPA	Single-photon absorption
TLS	Tuneable laser source
TPA	Two-photon absorption
TPAM	Two-photon absorption microcavity
VOA	Variable optical attenuator
WDM	Wavelength division multiplexing

1. Introduction

1.1 Background and motivation

The motivation of the work demonstrated in this thesis is twofold. Firstly the usefulness of using TPA as a means of monitoring network performance is investigated. The demonstrated usefulness of TPA as a monitoring tool increases the need for a TPA detector which can work at the low optical powers present. A TPA microcavity is investigated as being such a detector.

The work discussed in this thesis can be divided into two key parts. First is the characterisation of a two-photon absorption microcavity (TPAM) and second is the investigation of various optical performance monitoring (OPM) applications which are based on two-photon absorption (TPA). The TPAM investigated in this thesis could be used as detectors for carrying out OPM of signals in optical networks. The networks in which an OPM would be expected to operate are very dynamic and variable due to both physical changes and network management changes. The primary physical changes which influence the operation of a network include processes such as dispersion and polarisation fluctuations experienced by signals transmitted through these networks [1-3]. Furthermore, with networks becoming increasingly transparent and flexible through the use of technologies such as reconfigurable optical add-drop multiplexers, an OPM application must be capable of operating at a range of both bit rates and modulation formats [4]. Another implication of this transparency is the removal of network health indicators associated with electrical signal regeneration and also with the propagation and build-up of impairments as a signal travels through a network (i.e. polarisation mode dispersion (PMD), amplified spontaneous emission (ASE) noise and chromatic dispersion (CD)). In order for a TPAM to be used in such an uncertain environment, its response (tuning, alignment sensitivity, and polarisation dependence) must be well understood, which is one of the objectives of this thesis, as well as an

investigation of some TPA based OPM techniques. These applications as well as a number of other TPA based applications are outlined in section 1.4. Also a number of TPAM OPM applications are demonstrated.

1.2 Thesis outline

Chapter 2: An introduction is given to etalon theory as well as a description of etalon reflection and transmission characteristics. The phase response of reflections from the etalon mirrors and the intracavity field are described. Distributed Bragg reflectors (DBRs) are introduced and their response investigated using the transverse matrix method (TMM).

Chapter 3: A microcavity structure is introduced and a description of the spectral dependence of both the reflection and the transmission response is given. The electric field in the microcavity and the lifetime of signals in the cavity are also discussed. Details of the TPAM devices which have been used in this thesis are given, including details of both device growth processing.

Chapter 4: The primary function of a TPAM structure is to enhance the level of TPA. The effect of this enhancement on the level of single photon absorption (SPA) in a TPAM is investigated. It is shown that the cavity acts to enhance the level of both SPA and TPA in the TPAM. When the overall effect of SPA and TPA enhancement is compared, the overall influence of the enhancement is to minimise the level of SPA relative to the level of TPA.

Chapter 5: The influence of the limited acceptance angle of a TPAM on its response is investigated. It is shown that the limited acceptance angle of the microcavity explains the observed asymmetry seen in the spectral dependence of

the TPAM. The theory derived can be used to calculate the optimum incident spot diameter for a TPAM in order to maximise the level of TPA.

Chapter 6: The polarisation response of a TPAM is investigated. The deviation in the dependence of the detector response from that of bulk GaAs is shown to be due to the birefringence of the cavity. A theoretical model based on the convolution of the cavity birefringence and the polarisation dependence of TPA in GaAs is described and shown to match the measured polarisation dependence of the TPAM detector very well.

Chapter 7: An investigation of the level of TPA generated by a signal which is comprised of polarised band-limited amplified spontaneous emission noise (BL-ASE) has been carried out. A theoretical investigation of the level of TPA generated by an ASE signal is shown to be in excellent agreement with the experimental data. An optical signal to noise ratio (OSNR) measurement is also carried out to further validate the theoretical model.

Chapter 8: A TPAM is shown to be capable of operating as a channel identification monitor. The detector is shown experimentally to be capable of discriminating between three different signal types which are BL-ASE, a 10 Gbs^{-1} 33 % return to zero on-off keyed (RZOOK) signal and a 40 Gbs^{-1} non return to zero differential phase shift keyed (NRZ-DPSK) signal. Also shown is the thermal tuning of the TPAM which can be used to tune the TPAM by approximately 5 nm with a 40 ^{0}C change in device temperature.

Chapter 9: A conclusion based on work contained in this thesis is given. Also possible future work is outlined.

1.3 Nonlinear optical processes: two-photon absorption

Nonlinear optics is an extremely broad field which is covered by a number of books and an extremely large number of scientific journal publications, see for example [5-7]. Nonlinear optics is used to refer to the range of processes which occur due to the incidence of intense incident light on a material. The intensity of light necessary in order to produce this modification of the material system is quite large. Due to this, it was only with the advent of the laser in 1960 and it became easier to access the nonlinear optical regime that research into nonlinear optics became an active field of research [8]. In 1961 second harmonic generation (SHG) at an optical frequency was demonstrated [9] and followed soon after by the observation of several other coherent optical frequency mixing effects (i.e. optical difference frequency generation and optical third-harmonic generation) [10]. With the observation of these nonlinear effects it was realised that the definition of the electrical polarisation vector (P) could be re-expressed in order to explain these nonlinear effects. In conventional (linear) optics

$$\hat{P} = \varepsilon_0 \chi^1 \hat{E} \tag{1.1}$$

where ε_0 is the permittivity of free space, χ is the susceptibility of the medium and $\hat{E}$ is the electric field, this equation can be re-expressed as a power series in order to take into account the effect of higher order material susceptibilities:

$$\hat{P} = \varepsilon_0 \left[\chi^1 \hat{E} + \chi^2 \hat{E}^2 + \chi^3 \hat{E}^3 + ... \right] \tag{1.2}$$

where χ^1, χ^2 and χ^3 are the first, second and third order susceptibilities, respectively. $\hat{P}^2(t) = \varepsilon_0 \chi^2 \hat{E}^2(t)$ and $\hat{P}^3(t) = \varepsilon_0 \chi^2 \hat{E}^3(t)$ can be referred to as the second and third order nonlinear polarisation, respectively. TPA is a third order process and as such $\hat{P}^3$ will be discussed in greater detail.

It is important to note that χ^3 is a 4th rank tensor with 3^4 (81) terms. For third order polarisation the Fourier component, $P_i^3(\omega_i, k_i)$, associated with a propagation direction k_i and a frequency ω_i can be expressed as [7, 11]:

$$\hat{P}_i^3(\omega_i,k_i)=\frac{\varepsilon_0}{4}\sum_{jkl}\chi^3_{ijkl}(\omega_i;\omega_j,\omega_k,\omega_l)\hat{E}_j(\omega_j,k_j)\hat{E}_k(\omega_k,k_k)\hat{E}_l(\omega_l,k_l) \qquad (1.3)$$

where E_j, E_k and E_l are the component field amplitudes, and *i*, *j*, *k* and *l* are the crystals principal crystallographic axes [100], [010] and [001], which are represented here by the unit vectors $\hat{x}$, $\hat{y}$ and $\hat{z}$. Photon energy and momentum conservation mean that $\omega_i=\omega_j+\omega_k+\omega_l$ and $k_i=k_j+k_k+k_l$, respectively.

It is more convenient for (1.3) to be written in a lab frame as this allows an arbitrary set of polarisation directions to be defined as the principle axes. This is done by expressing (1.3) in terms of frequencies ω_b, ω_c, and ω_d and by defining the polarisations using the unit vectors $\hat{b}$, $\hat{c}$ and $\hat{d}$, (1.3) can then be expressed in terms of a direction $\hat{a}$ and a frequency ω_a [11]

$$\begin{aligned}\hat{P}_a^{\,3}(\omega_a,k_a)=&\frac{\varepsilon_0}{4}\sum_{bcd}\sum_{ijkl}\chi^3_{ijkl}(\omega_a;\omega_b,\omega_c,\omega_d)\\&\cdot a_i^* b_j c_k d_l\,\hat{E}_b(\omega_b,k_b)\hat{E}_c(\omega_c,k_c)\hat{E}_d(\omega_d,k_d)\end{aligned} \qquad (1.4)$$

where $a_i^*=\hat{a}^*\cdot\hat{i}$, $b_j=\hat{b}\cdot\hat{j}$, $c_k=\hat{c}\cdot\hat{k}$ and $d_l=\hat{d}\cdot\hat{l}$ are the direction cosines for the projections $\hat{P}_a^*$, $\hat{E}_b$, $\hat{E}_c$ and $\hat{E}_d$ onto the directions $\hat{i}$, $\hat{j}$, $\hat{k}$ and $\hat{l}$, respectively. The summation over *i* and over the direction cosine a_i^* is to take into account the contributions of all $\hat{P}_i$ along the a_i^* direction. In order for $\hat{P}_a$ to be found for all ω_a, the summation over the three axis directions (*b*, *c* and *d*) must be carried out for all instances for which the combination of the three fields ($\hat{E}_b$, $\hat{E}_c$ and $\hat{E}_d$) for which $\omega_a=\omega_b+\omega_c+\omega_d$ and $k_a=k_b+k_c+k_d$.

(1.4) can be simplified by taking into account symmetry associated with isotropic materials (such as GaAs which is the material for which the TPA based detection in this thesis has been carried out). Due to the intrinsic symmetries in the structure of GaAs, χ^3 for GaAs has only 21 values which are non-zero, and of these only 4 are independent [11]. The four independent elements are of the form: χ_{gggg}, χ_{gghh}, χ_{ghgh} and χ_{ghhg}, where *g* and *h* are used to refer to the tensor indices *x*, *y* and *z*. For isotropic materials the relationship between these terms

can be described by σ which can be used as a measure of the anisotropy of the material. (This value is investigated for a TPAM in chapter 6.)

$$\sigma = \frac{\chi_{xxxx} - (\chi_{xxyy} + \chi_{xyxy} + \chi_{xyyx})}{\chi_{xxxx}} \tag{1.5}$$

By using (1.5) and expressing terms of the form $(\hat{a}\cdot\hat{c})(\hat{b}\cdot\hat{d})$ as

$$(\hat{a}\cdot\hat{c})(\hat{b}\cdot\hat{d}) = \sum_i \hat{a}_i^* \hat{b}_i \hat{c}_i \hat{d}_i + \sum_{i,j\neq i} a_i^* b_i c_i d_i \tag{1.6}$$

(1.4) can be expressed (without the explicit stating of the frequency and wavevector dependencies for simplicity) as [11]

$$\hat{P}_a^3 = \frac{\varepsilon_0}{4} \sum_{bcd} \chi_{eff}(a;b,c,d) \hat{E}_b \hat{E}_c \hat{E}_d \tag{1.7}$$

where χ_{eff} is defined as

$$\begin{aligned} \chi_{eff}(a;b,c,d) = {} & \chi_{xxyy}(\hat{a}^*\cdot\hat{b})(\hat{c}\cdot\hat{d}) + \chi_{xyyx}(\hat{a}^*\cdot\hat{d})(\hat{b}\cdot\hat{c}) \\ & + \chi_{xyxy}(\hat{a}^*\cdot\hat{c})(\hat{b}\cdot\hat{d}) + \sigma\chi_{xxxx}\sum_i a_i^* b_i c_i d_i \end{aligned} \tag{1.8}$$

For degenerate resonant TPA that is the subject described by this thesis, (1.8) can be further simplified. As all fields in degenerate TPA have the same frequency (ω), the only tensor elements needed are of the form $\chi_{ijkl}(\omega;-\omega,\omega,\omega)$. Also, intrinsic permutation symmetry allows for the interchange of i with j, k and l. As a result of these symmetries only three independent tensor elements remain, which are the elements χ_{xxxx}, χ_{xxyy}, and $\chi_{xyyx} = \chi_{xyxy}$. (1.7) and (1.8) can now be expressed as [11]

$$\sigma = \frac{\chi_{xxxx} - (\chi_{xxyy} + 2\chi_{xyxy})}{\chi_{xxxx}} \tag{1.9}$$

and

$$\begin{aligned} \chi_{eff}(a;b,c,d) = {} & \chi_{xxyy}(\hat{a}^*\cdot\hat{b})(\hat{c}\cdot\hat{d}) + \chi_{xyyx}[(\hat{a}^*\cdot\hat{d})(\hat{b}\cdot\hat{c}) + (\hat{a}^*\cdot\hat{c})(\hat{b}\cdot\hat{d})] \\ & + \sigma\chi_{xxxx}\sum_i a_i^* b_i c_i d_i \end{aligned} \tag{1.10}$$

In order to understand the response described by (1.7) a pump-probe measurement can be considered. (1.7) can be expressed in terms of the polarisation of the pump and the probe, with only terms which have the same

pump and probe polarisation being considered (p), as these are the only terms necessary in order to explain degenerate TPA.

$$\hat{P}_p^3(\omega,k_p)=\frac{\varepsilon_0}{4}\left[\chi_{eff}(p;p^*,p,p)\left|\hat{E}_p(\omega,k_p)\right|^2\hat{E}_p(\omega,k_p)\right] \tag{1.11}$$

where $\left|E_p(\omega,k_p)\right|$ is the absolute of $E_p(\omega,k_p)$. The terms neglected in formulating (1.11) refer to a cross polarised pump and probe which describe cross phase modulation. (1.11) is then substituted into the reduced wave equation

$$(\hat{k}.\nabla)\hat{E}_p=\left[\frac{i\omega}{2nc\varepsilon_0}\right]\hat{P}_p^3 \tag{1.12}$$

where the slowly varying envelope approximation and a transformation to time-retarded coordinates were made and where n and c are the refractive index and speed of light, respectively. The variation in the intensity of the combined pump and probe (I_p) as it propagates along direction z can then be described by [11]

$$\frac{\delta I_p}{\delta z}\approx-\beta_{pp}I_p^2 \tag{1.13}$$

where the TPA absorption coefficient for a co-polarised pump and probe (β_{pp}) is defined as

$$\begin{aligned}\beta_{pp}&=\left[\frac{\omega}{2n^2c^2\varepsilon_0}\right]Im\left[\left\{\chi_{eff}(p;p^*,p,p)\right\}\right]\\&=\frac{\omega}{2n^2c^2\varepsilon_0}Im\left\{\chi_{xxyy}\left|\hat{p}.\hat{p}\right|^2+2\chi_{xyyx}+\sigma\chi_{xxxx}\sum_i\left|p_i\right|^4\right\}\end{aligned} \tag{1.14}$$

1.4 Applications of two-photon absorption

1.4.1 Introduction

Traditionally optical pulse characterisation as well as processing of optical signals has not been carried out using nonlinear detectors such as the TPAM described in this thesis. Instead high speed linear photodetectors and electrical

switches have been used. For short pulses (< 10 ps) operating at high data rates (> 40 Gbs^{-1}) this becomes increasingly difficult although certain schemes have been found to allow linear detectors to be used to characterise short optical pulses [12]. This limit on pulse duration is imposed because of a fundamental limitation on the frequency response of the electronics involved in these measurements which result in problems with measurements at speeds in excess of 50 GHz [13].

While TPA is the primary focus of this thesis, a number of these applications as well as numerous other applications can be carried out using other non-linear processes. These processes include second harmonic generation, four-wave mixing and the optical Kerr effect [14-16]. What follows is an outline of some of the most promising and useful applications which have been suggested which utilise TPA based detection.

The reason for focusing on using the TPA process, as opposed to the range of other possible nonlinear processes, is that TPA allows the use of simple electrical detection [17]. Using TPA does not require expensive nonlinear crystals and the associated need for phase matching which inherently add cost and remove robustness from a detection scheme. Also it is shown that slow TPA detectors are well suited to carrying out monitoring and for detection of high speed optical signals due to the intrinsically high speed nature of the TPA process [18, 19].

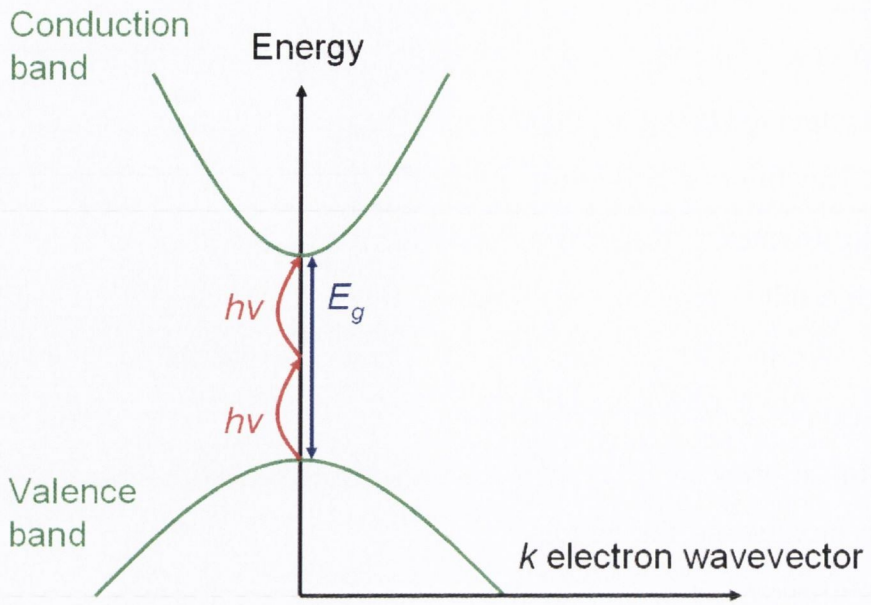

Fig. 1.1 Simplified schematic of band structure of a direct bandgap material, showing a degenerate TPA process.

TPA is a nonlinear process which was first observed in 1961, see section 1.3 [20]. TPA occurs when two photons with energy $h\upsilon$ are absorbed by a material for which the semiconductor energy gap (E_g) is greater than $h\upsilon$ but less than or equal to $2h\upsilon$, see Fig. 1.1. The TPA considered in this thesis is degenerate TPA which means that both photons absorbed have the same energy. The absorption of the two-photons is via an intermediate virtual state, the lifetime of which is governed by the uncertainty principle [21]. It is due to the short lived nature of this intermediate state that TPA is an intrinsically high speed process. The intermediate state can be any state in any band, although the probability of the absorption process happening is highest when the energy difference between the states involved is smallest (i.e. when the intermediate state is close to either the upper valence band or the lower conduction band) [21-23]. As stated in (1.13), the rate of TPA is proportional to the incident signal intensity squared.

1.4.2 Optical time division multiplexing

One method of increasing individual channel data rates is via the use of optical time division multiplexing (OTDM) [24, 25], see Fig. 1.2. OTDM makes it possible to achieve optical channel data rates that operate at much higher frequencies than that of the electrical equipment which generated the constituent optical signals. This increase in data rates is achieved using a pulse source which operates at a frequency for which the electrical components are easily available (which currently means working at around 10 GHz). This signal is then separated using a passive optical splitter, see Fig. 1.2. Each of the separated signal channels is individually encoded with data. The signals are then delayed so as to have each of the signal channels evenly distributed in the time domain in the bit slot when they are multiplexed together. Recently, transmission of an individual channel with a data rate of 170 Gbs^{-1} over a distance of 4320 km was achieved using OTDM [26]. Also individual signals with channel data rates of 2.56 Tbs^{-1} have been transmitted error free (bit error rate (BER) < 10^{-9}) [27].

OTDM systems are heavily reliant on a number of technologies, which can be broken up into three main parts: the transmitter, fibre transmission and receiver. An OTDM transmitter consists of a pulse source which is operating at a specific repetition frequency (i.e. 10 GHz). The pulse source ideally has much shorter pulses that are normally used at that repetition frequency. At 10 GHz the pulses for a non-OTDM system would be approximately 33 ps for a RZOOK modulated signal. For an OTDM system which is multiplexing 3 signals with a repetition frequency of 10 GHz the pulse duration would ideally be less than one third of the non-OTDM pulse duration (i.e. less than 11 ps).

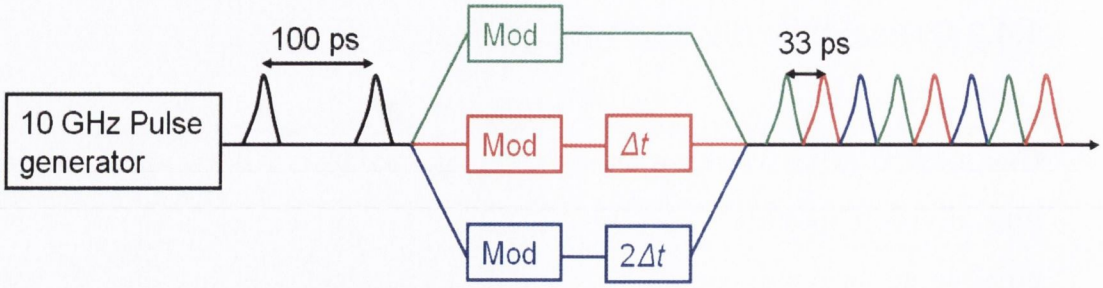

Fig. 1.2 Schematic of an OTDM transmitter. Mod is an optical modulator. Δt is a time delay designed to interleave the optical pulses (in this example Δt is 33 ps).

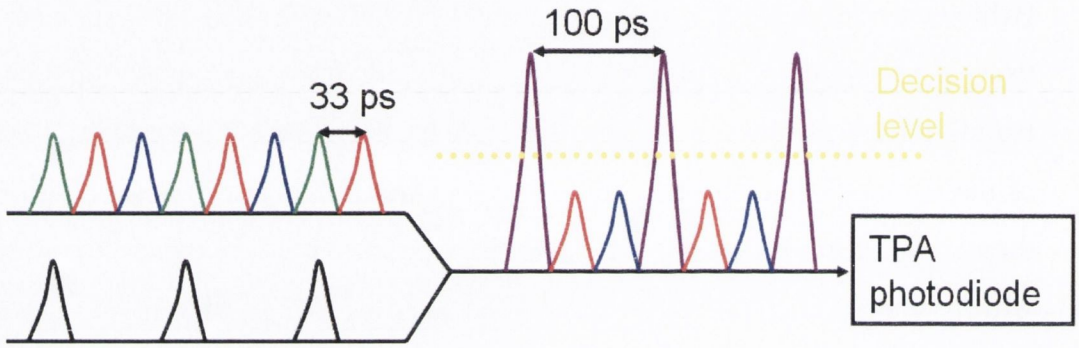

Fig. 1.3 Schematic of OTDM receiver. The TPA photodiode is operating as an optical thresholder. Signals below the decision threshold result in a 0 being detected while signal above the decision threshold results in a 1.

TPA has over the last number of years been suggested for use in de-multiplexing the signal at the receiver [28-32]. TPA based OTDM de-multiplexers work by coupling the received signal channel with a local oscillator, see Fig. 1.3. The TPA response is proportional to $\left|E_{sig}+E_{probe}\right|^4$, where E_{sig} and E_{probe} are the signal and probe field amplitudes. When the probe is overlapped with the signal which is to be de-multiplexed the resulting TPA signal is larger than the TPA signal generated when the probe is not overlapped, see Fig. 1.3. The result of this, for the example given in Fig. 1.3, is that the TPA detector only detects one of the three convoluted signals as the other signals result in current levels which are set to be below the decision threshold. The decision threshold is set to be a current level greater than the level of current generated by a pulse

which is not overlapped with the local oscillator. In this way, the TPA detector is working as a high speed optical threshold [33]. This means the TPA based photodiode which is operating at the same frequency as the pulse generator is capable of detecting the signal even though it is not capable of operating at the channel data rate (i.e. 30 Gbs^{-1}), see Fig. 1.3.

1.4.3 Auto and cross correlation

For pulses with pulse widths below 10 ps, electrical detection using a fast photodetector is in general no longer suitable. Both auto-correlation and cross-correlation of optical pulses can be used to retrieve temporal information about extremely short pulse (< 10 ps). Autocorrelation involves investigating a pulse in a pump-probe type measurement while using the pulse itself as the probe, see Fig 1.4 The signal under test is split using a beam splitter with one arm corresponding to the signal arm and the other being the probe arm [34, 35]. The variable time delay on the probe arm is varied and then the signals are recombined before being detected using a TPA photodiode [36].

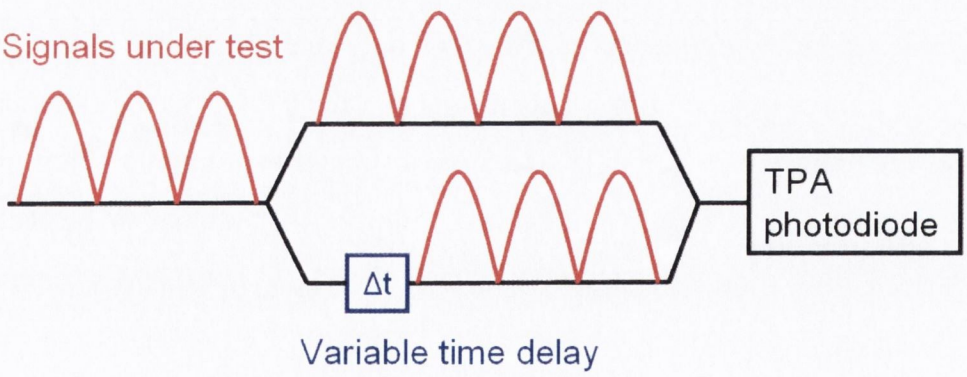

Fig. 1.4 Schematic of an optical auto-correlator utilising a TPA photodetector, there optical path containing the variable time delay is the probe arm while the alternate optical path is the signal arm.

It has been shown that TPA based autocorrelation can be used to retrieve temporal information about extremely short optical pulses [21, 37-39]. TPA based autocorrelation has been demonstrated as being possible even at very low optical powers [40]. A limitation of autocorrelation is that while it can give accurate information about pulse duration the result of an autocorrelation is always symmetric and so gives little to no information about pulse shape [5, 41].

Crosscorrelation is also a very powerful pulse characterisation technique. The main advantage of crosscorrelation over autocorrelation is that the pulse shape (level of pulse asymmetry) can be measured. The asymmetry of a pulse can be very important as it can be used to obtain information relating to a number of characteristics of a pulse such as pulse chirp. The primary way in which crosscorrelation is used in telecommunication systems is in carrying out optical sampling measurements.

Optical sampling involves taking a pulse stream and then investigating its amplitude in the time domain using a temporally short probe pulse (ideally much shorter than the pulses under test), see Fig. 1.5. The probe pulse is set to have a low repetition frequency (i.e. approximately 10 MHz) which is a frequency that is set to be slightly offset from being an integer multiple of the of the repetition frequency of the pulses under test [29]. The small frequency offset acts like a variable temporal delay of the probe signal relative to the pulses under test and so the probe scans across the pulses under test in the time domain. The low probe pulse repetition frequency ensures that only one probe pulse interacts with the pulse train at any one time. This means that the TPA detector electrical response is only required to operate at a frequency greater than the repetition frequency of the probe pulse. TPA based optical sampling has shown to be well suited to investigating short optical pulses such as those used in OTDM systems [42-44].

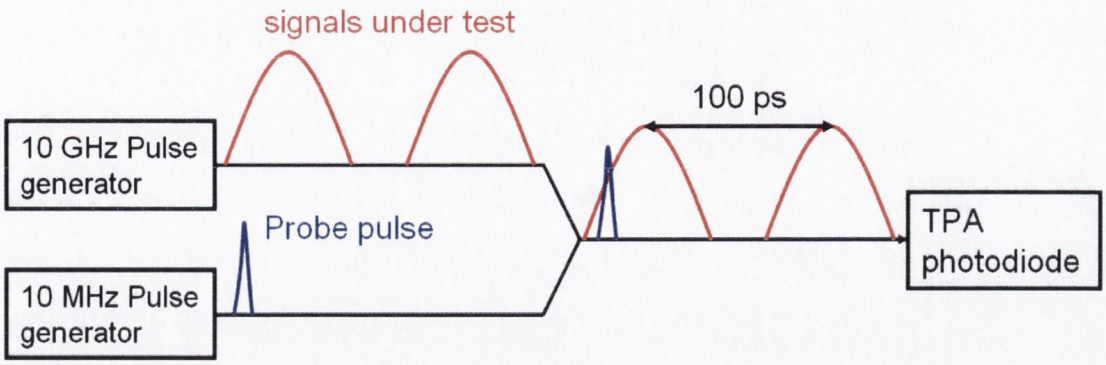

Fig. 1.5 Schematic of an optical sampling (cross correlation) system utilising a TPA photodetector.

Another application of cross correlation is to carry out clock recovery. Clock recovery refers to recovering the electrical timing signal which operates at the individual channel data rate [1]. Clock recovery involves synchronizing the phase of a local clock signal with that of the clock signal of the incident pulses which are to be detected, see Fig. 1.6 [45]. When the clock pulses are overlapped in the time domain with the data pulses the detected TPA photocurrent is maximised and so by varying the delay between the data and the clock signal the clock is deemed to be found when the TPA signal is maximised [46]. Successful clock recovery has been shown previously for signal data rates of 80 Gbs^{-1} using TPA based detection [47].

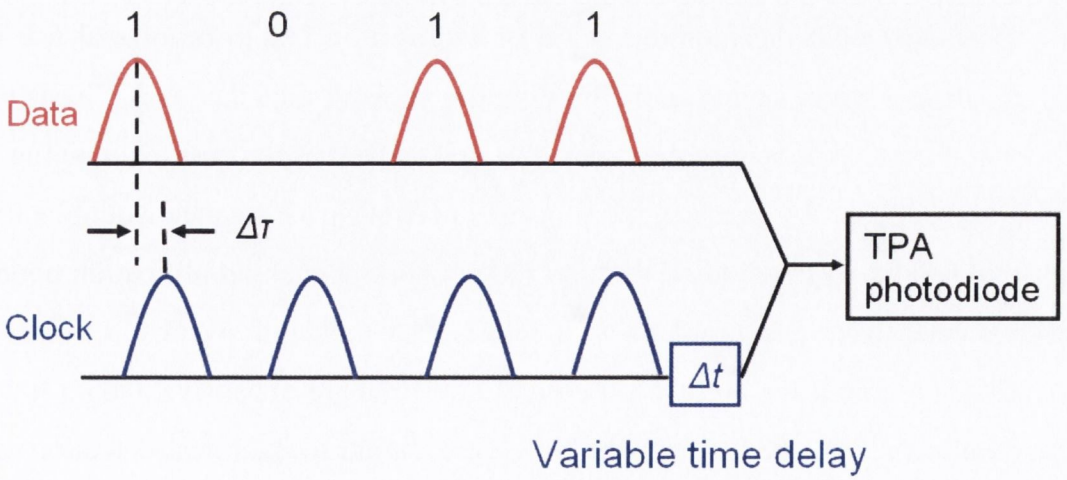

Fig. 1.6 Schematic of a clock recovery (cross correlation) system utilising a TPA photodetector, $\Delta\tau$ is the time difference between the peak of one of the data pulse and one of the clock pulses.

1.4.4 Optical performance monitoring

Optical performance monitoring (OPM) is a general term that refers to monitoring the fidelity of the transmission of an optical signal as it is transmitted through an optical network [48]. OPM is taken in general to be a means of measuring network health and channel degradation. A variety of different forms of OPM have received attention over the last number of years [48-50]. Through the use of OPM it is hoped that the network will have increased flexibility, reliability and functionality [51-53]. To date the most common forms of OPM have been carried out using linear detection. These schemes focus around the monitoring of average signal power, channel power, channel wavelength, degree of signal polarisation, bit error rate (BER) and spectral OSNR [48, 54-60]. Also a number of monitoring schemes based on placing low frequency modulated signals on the transmitted signal and then monitoring the transmission of these modulated signals at different points throughout the network have been demonstrated [61, 62]. These schemes suffer from a number of drawbacks related to the quality of the information that can be garnered from the measurement as well as the interpretation of multiple impairments resulting in problems interpreting the measured result as well as high implementation costs.

While a combination of OPM schemes could definitely give very high quality network performance data this may not be practical due to the high cost associated with the monitoring. In order for an OPM to be of real use it must result in a larger saving in the running the network on a day to day basis than the initial cost associated with implementing it as well as the cost maintaining it [48]. One very useful method of monitoring a network performance would be to detect the data being transmitted through the network at each amplification node in the network [57]. The problem with this is that the high speed electronics (> 40 Gbs^{-1}) required for high speed optical networks are expensive and so lower cost monitoring schemes are needed which are similar to the linear detection schemes mentioned above but which provide more detailed network performance data.

As well as the linear detection schemes mentioned above there are also a wide variety of OPM schemes based on non linear processes such as SHG, four wave mixing [63] and the optical Kerr effect. Each of these processes has been linked with a large number of monitoring applications. SHG is most widely used in carrying out SHG frequency resolved optical gate (SHG-FROG) applications, which is a measurement which can retrieve both the intensity and phase information of a pulse in real time (> 2Hz) [15, 64, 65].

In this thesis, TPA based OPM schemes are investigated [66, 67]. The schemes that have been looked at here are based on monitoring OSNR and on measuring channel presence. TPA based OSNR monitoring has been investigated by a number of groups in the past [19, 68-70].

2. Transfer matrix method

2.1 Fabry-Perot etalon

The Fabry-Perot etalon (FPE) is the basic structure on which the TPAM is based [71, 72]. When the resonance condition of the etalon is satisfied the overall reflectivity of the etalon tends towards a minimum while the intra-cavity field can be greatly enhanced. In order to characterise the response of a microcavity which consists of two distributed Bragg reflectors (DBR's) the response of a simple two mirror etalon must be understood. This is because the response of a microcavity as a whole can be quite complex. It is instead easier to study each DBR on its own and then to treat each DBR as a single etalon mirror. This then allows basic etalon theory to be used in order to describe the response of a microcavity. The primary things that must be investigated in order to characterise the response of a FPE are the fields generated (reflected, transmitted and in the spacer region of the etalon) and the phase shift in the mirrors associated with changing wavelength and incident angle.

2.1.1 Etalon transmission and reflection

A FPE's response is made up of reflection and transmission spectra associated with the make up of its mirrors. To study the FPE response the transmission and reflection coefficients associated with these layers must first be calculated. The theory described here only deals with transverse electric modes (TE) as under normal experimental conditions the influence of transverse magnetic modes (TM) is insignificant. The reason the TM mode is not investigated here is because its contribution is negligible when the signal input on the TPAM is close

to normal which is the conditions under which the TPAM has been used for the work discussed in this thesis.

The reflection coefficient associated with light incident from layer i (L_i) onto the layer boundary (z_{i+1}) between L_i and L_{i+1} is $r_{i,i+1}$, see Fig. 2.1. The transmission coefficient associated with light incident from L_i though the layer boundary z_{i+1} is $t_{i,i+1}$

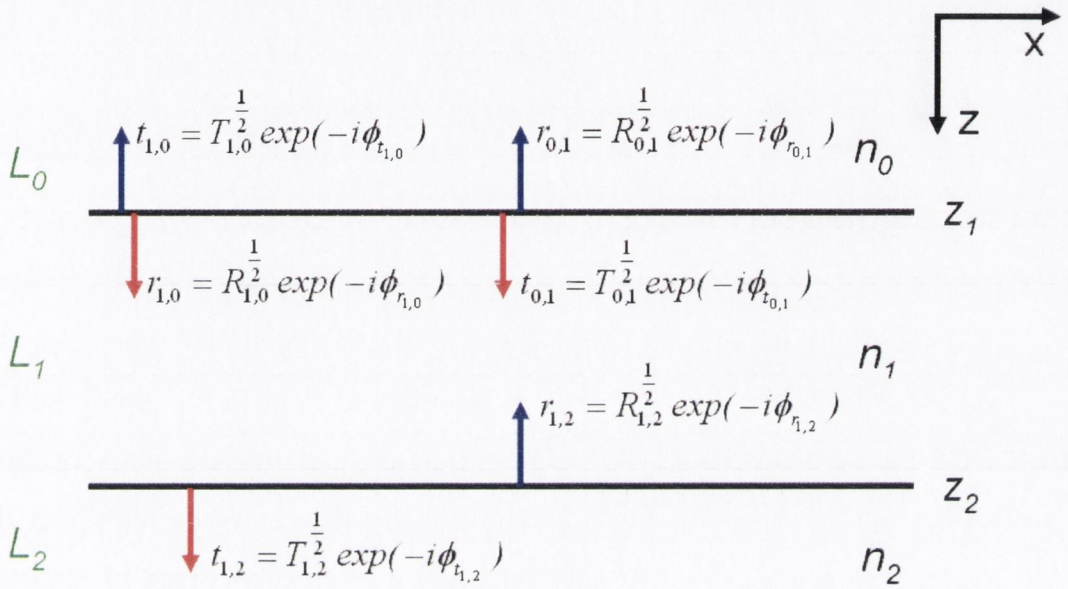

Fig 2.1 Explanation of nomenclature used in describing etalons. L_0 is layer 0, n_0 is the refractive index of layer L_0, z_1 is the interface between L_0 and L_1, $t_{0,1}$ is the transmission coefficient for light transmitted from L_0 into L_1 and $r_{0,1}$ is the reflection coefficient for light incident on z_i from L_0 that is reflected back into L_0, $\phi_{r_{0,1}}$ is the phase shift associated with $r_{0,1}$.

The individual reflection and transmission coefficients are calculated using the Fresnel equations [73]

$$r_{0,1} = \frac{n_0 \cos\theta_0 - n_1 \cos\theta_1}{n_0 \cos\theta_0 + n_1 \cos\theta_1}\ ,\ t_{0,1} = \frac{2n_0 \cos\theta_1}{n_0 \cos\theta_1 + n_1 \cos\theta_0} \qquad (2.1)$$

where θ_i is the incident angle of light input from L_i which is incident on z_{i+1}, n_i is the refractive index of L_i. As well as the phase shift due to the transmission through the etalon there is also a phase change associated with the reflection (ϕ_r) at the etalon interfaces. ϕ_r is associated with the change in sign of the reflection coefficient. If the reflection coefficient is negative then this results in a π phase shift for the reflected signal. So if $n_2 > n_1$ then there is a π phase shift associated

with r_0 where as there is no phase shift associated with the sign of the reflection coefficient when $n_1 > n_2$. The transmission coefficient has no phase shift associated with it. If the mirror has no loss then

$$R_{i,i+1} = \left| r_{i,i+1}{}^2 \right| \ , \ T_{i,i+1} = \left| t_{i,i+1}{}^2 \right| \tag{2.2}$$

$$R_{i,i+1} + T_{i,i+1} = 1 \tag{2.3}$$

$$R_{i,i+1} = R_{i+1,i} \tag{2.4}$$

2.1.2 Intra-cavity field

For simplicity the normal incidence case is considered here when calculating the intra-cavity field e_c/e_{in} (where e_c is the electric field in the cavity and e_{in} is the field incident on the cavity). The reflection and transmission coefficients are calculated as shown in Fig 2.2. The field in the cavity builds up as the signal incident through z_1 is internally reflected a number of times in the etalon. The signal builds up according to

$$F_1 = t_{0,1} e^{-ikz} \tag{2.5}$$

$$F_2 = t_{0,1} e^{-ikd} r_{1,2} e^{-ik(d-z)} \tag{2.6}$$

$$F_3 = t_{0,1} e^{-ikd} r_{1,2} e^{-ikd} r_{1,0} e^{-ikz} \tag{2.7}$$

$$F_4 = t_{0,1} e^{-ikd} r_{1,2} e^{-ikd} r_{1,0} e^{-ikd} r_{1,2} e^{-ik(d-z)} \tag{2.8}$$

(2.5-2.8) shows that the field builds up as a geometric power series

$$y = F_1 + F_2 \tag{2.9}$$

$$F_3 = F_1(x), \quad F_4 = F_2(x) \tag{2.10}$$

$$F_3 + F_4 = yx, \quad F_5 + F_6 = yx^2 \tag{2.11}$$

$$\frac{e_c}{e_{in}} = y + yx + yx^2 + \ldots = \frac{y}{1-x} \tag{2.12}$$

$$\frac{e_c}{e_{in}} = \sqrt{T_{0,1}}\, exp(-i\phi_{t_{0,1}}) \left[\frac{e^{(-ikz)} + \sqrt{R_{1,2}}\, e^{-i(2k_z d + \phi_{r_{1,2}})} e^{(ik_z z)}}{1 - \sqrt{R_{1,0}}\sqrt{R_{1,2}}\, e^{-i(\phi_{r_{1,0}} + \phi_{r_{1,2}} + 2k_z d)}} \right] \tag{2.13}$$

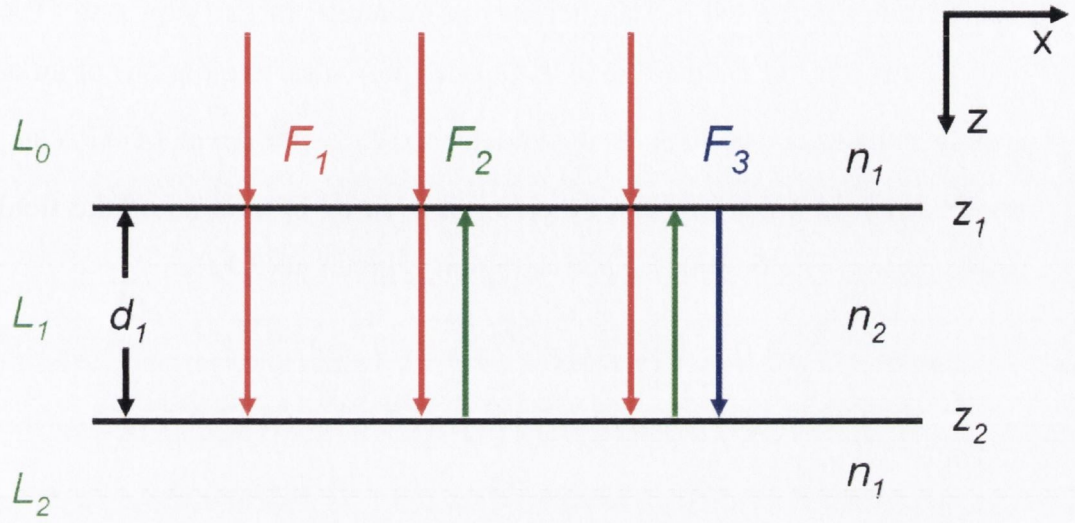

Fig 2.2 Explanation of transmission and reflection coefficients, d_i is the distance between interface z_i and z_i+1.

It is similarly possible to calculate the transmitted field (e_t/e_{in}) and the reflected field (e_r/e_{in})

$$\frac{e_t}{e_{in}} = \frac{(T_{0,1}T_{1,2})^{\frac{1}{2}} e^{-i(\phi_{t0,1}+\phi_{t1,2}+k_z d)}}{1-\sqrt{R_{1,0}R_{1,2}}\, e^{-i(\phi_{r1,0}+\phi_{r1,2}+2k_z d)}} \tag{2.14}$$

$$\frac{e_r}{e_{in}} = (R_{0,1})^{\frac{1}{2}} e^{(-i\phi_{r0,1})} + \frac{(T_{0,1}T_{1,0}R_{1,2})e^{-i(\phi_{t0,1}+\phi_{t1,0}+\phi_{r1,2}+2k_z d)}}{1-\sqrt{R_{1,0}R_{1,2}}\, e^{-i(\phi_{r1,0}+\phi_{r1,2}+2k_z d)}} \tag{2.15}$$

and the reflected power R_{fp} and transmitted power T_{fp} are

$$R_{FP} = \left|\frac{e_r}{e_{in}}\right|^2 \tag{2.16}$$

$$T_{FP} = \left|\frac{e_t}{e_{in}}\right|^2 \tag{2.17}$$

2.1.3 Field enhancement

The reason for the use of a microcavity structure in carrying out TPA based detection is that the field (E_{act}) in the spacer region (active region) of an etalon is greatly enhanced. As TPA is dependent on $|E_{act}|^4$ the level of TPA generated photocurrent in a detector can be greatly increased by enhancing the field in the active region. The field in the active region is given in (2.13).

$$|E|_{act}^2 = \left|\frac{e_c}{e_{in}}\right|^2 = T_{0,1}\frac{1+R_{1,2}+2\sqrt{R_{1,2}}\,cos(2k_z z)}{\left(1-\sqrt{R_{0,1}R_{1,2}}\right)^2} \tag{2.18}$$

which was derived using:

$$|(a+b)|^2 = |a|^2 + |b|^2 + 2\,Re(ab^*) \tag{2.19}$$

where z refers to distance travelled from z_1 in the z direction (see Fig. 2.2), $|E|_{act}^2$ is the intensity of the field in the active region, b^* is the conjugate of b, Re(ab^*) is the real part of ab^*.

$$\begin{aligned} |E|_{act}^4 &= \left|\frac{e_c}{e_{in}}\right|^4 \\ &= T_{0,1}^2\frac{1+2R_{1,2}+4\sqrt{R_{1,2}}\,cos(2k_z d)+4R_{1,2}^{3/2}\,cos(2k_z d)+4R_{1,2}\,cos^2(2k_z d)}{\left(1-\sqrt{R_{0,1}R_{1,2}}\right)^4} \end{aligned} \tag{2.20}$$

where d is the thickness of the spacer region. The ratio of TPA generated in a cavity relative to a non-cavity case is ζ_{TPA}. The non-cavity case refers to absorption in a layer identical to the active region but which is not sandwiched between two mirrors

$$\zeta_{TPA} = \int_0^d |E|_{act}^4\,dz = T_{0,1}^2\frac{1+R_{1,2}^2+4R_{1,2}}{\left(1-\sqrt{R_{0,1}R_{1,2}}\right)^4} \tag{2.21}$$

as all remaining sine terms disappear (as $2k_z d$ is 2π) for the resonance case.

2.1.4 Phase response

In order to investigate the phase response the first step is to find the transmitted electric amplitude E_{tr}. For simplicity a 2 layer structure as is shown in Fig. 2.2 is investigated

$$E_{tr} = \frac{T_{0,1}T_{1,2}}{1+R_{1,0}R_{1,2}-2\sqrt{R_{1,0}R_{1,2}}\,cos(\psi)} \tag{2.22}$$

where $\psi = \phi_{r_{1,0}} + \phi_{r_{1,2}} + 2k_z d$. If for some reason ψ changes by a small amount $\delta\psi$ away from resonance i.e. due to a change in wavelength (λ) of the signal incident on the cavity, then the transmitted power is found using (2.17, 2.22) to be approximately

$$T_{FP} \approx \frac{T_{0,1}T_{1,2}}{\left(1-\sqrt{R_{1,0}R_{1,2}}\right)^2 + \sqrt{R_{1,0}R_{1,2}}\,\delta\psi^2} \tag{2.23}$$

where the denominator is calculated using the expansion

$$cos(\psi) = \sum_{n=0}^{\infty}(-1)^n \frac{\psi^{2n}}{(2n)!} \approx 1-\frac{\psi^2}{2} \tag{2.24}$$

The spectral dependence of (2.23) is Lorentzian around the resonant wavelength of an etalon. The full width at half maximum (FWHM) of the Lorentzian response can be worked out using:

$$T_{FP}(at\ FWHM) \approx \frac{T_{0,1}T_{1,2}}{\left(1-\sqrt{R_{1,0}R_{1,2}}\right)^2 + \sqrt{R_{1,0}R_{1,2}}\,\delta\psi_{FWHM}^2} \approx \frac{T_{0,1}T_{1,2}}{2\left(1-\sqrt{R_{1,0}R_{1,2}}\right)^2} \tag{2.25}$$

From (2.25) $\delta\psi_{FWHM}$ can be calculated

$$\delta\psi_{FWHM} = \frac{2(1-R)}{\sqrt{R}} \tag{2.26}$$

where $R = \sqrt{R_{1,0}R_{1,2}}$, so R is the average reflectivity of the etalon. If $\delta\psi$ is assumed to be due entirely to the shift in incident wavelength (λ) away from the resonance wavelength (λ_0), then

$$\delta\psi \approx \delta\lambda \left.\frac{\partial\psi}{\partial\lambda}\right|_{\lambda_0} \approx \delta\lambda \left[\left.\frac{\partial}{\partial\lambda}\left(\frac{4\pi nd}{\lambda}\right)\right|_{\lambda_0} + \left.\frac{\partial\phi_{r_{1,0}}}{\partial\lambda}\right|_{\lambda_0} + \left.\frac{\partial\phi_{r_{1,2}}}{\partial\lambda}\right|_{\lambda_0} \right] \tag{2.27}$$

The first term on the right side of (2.27) is due to phase change in the spacer layer in the etalon and can be easily calculated. The two remaining terms on the right had side are phase shifts due to the top and bottom mirrors respectively. The mirror phase shifts become difficult to calculate for etalons with multiple layers in their top and bottom mirrors as is the case in the TPAM under study in this thesis. This means that in practice the transverse matrix method (TMM) is used to study the TPAM response.

Using (2.27) the Free Spectral Range (FSR) and the finesse of the etalon can be calculated. (2.27) can be expressed as

$$\delta\psi \approx -\delta\lambda \frac{4\pi}{\lambda_0^2}\left(n_g + d_{r_{1,2}} + d_{r_{1,0}}\right) \tag{2.28}$$

where d_{r_1} and d_{r_2} are penetration depths into the z_1 and z_2 interfaces respectively

$$d_{r_{1,2}} = -\frac{\lambda_0^2}{4\pi}\frac{\partial\phi_{r_{1,2}}}{\partial\lambda}\bigg|_{\lambda_0} \tag{2.29}$$

So the spectral FWHM of the transmission spectrum at normal incidence is

$$\delta\lambda_{FWHM} = \frac{(1-R)\lambda_0^2}{\sqrt{R}2\pi D} \tag{2.30}$$

where $D = n_g d_1 + d_{r_{1,0}} + d_{r_{1,2}}$, n_g is the group index of the spacer region. The phase shift associated with the FSR is $\delta\psi_{FSR} = 2\pi$. The wavelength shift to go to the next resonant peak of the etalon is

$$\delta\lambda_{FSR} = \frac{\lambda_0^2}{2D} = FSR \tag{2.31}$$

The finesse of an etalon is the FSR divided by $\delta\lambda$ so:

$$Finesse = \frac{\sqrt{R}\pi}{(1-R)} \tag{2.32}$$

Experimentally R for a cavity is calculated by simulating the cavity response using the transverse matrix method (see section 2.2) in order to find D. Then R is calculated using (2.31) and (2.32).

2.1.5 Distributed Bragg reflector

The mirror structure used in creating a TPAM is a DBR. A DBR is made up of mirror pairs which have high (n_h) and low (n_l) refractive indices respectively. The individual thickness of each of these layers is:

$$d_i = \frac{\lambda_B}{4n_i} \tag{2.33}$$

where λ_B is the design wavelength (Bragg wavelength) for the mirrors, d_i is the physical thickness of L_i.

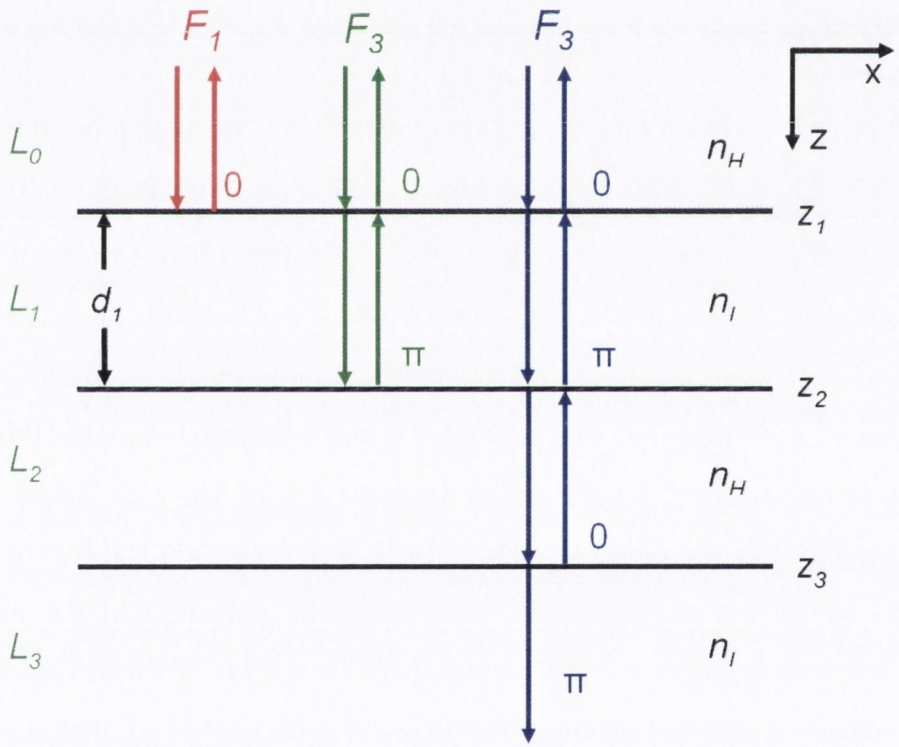

Fig. 2.3 Phase accumulation for signal normally incident on DBR at λ_B.

When an input signal with λ_B is normally incident on the DBR the phase shift due to propagation builds up as shown in Fig. 2.3. It is important to note that the phase shift referred to in this case is the phase of a signal relative to the phase of the initial signal incident from L_0 at z_1. Propagation through each of the layers in the z and $-z$ directions results in a $\pi/2$ and $-\pi/2$ phase accumulation respectively. The reflected phase at interface z_1 for each of the 3 signal cases

shown (F_1, F_2, and F_3) is 0. This means the reflected signals are in phase and so add constructively resulting in such a DBR structure having high reflectivity centred on λ_B. The phase of the transmitted signal increases by $\pi/2$ for each layer it passes through with an output phase of π resulting from the structure shown in Fig. 2.3. Once the input signal deviates from λ_B then the phase shift resulting from transiting a layer deviates from $\pi/2$ and $-\pi/2$ respectively. In practice the resulting phase, reflection and transmission of the DBR is investigated using the transverse matrix method (TMM).

Results of a TMM simulation for the reflection, transmission response of a DBR are shown in Fig. 2.4 (a, b). The DBR structure simulated is a GaAs/AlAs structure with 20 mirror pairs with λ_B = 1550 nm. The high refractive index contrast between air and the top mirror of the DBR means that the signal in the cavity is quite close to normal (0 degrees) even if the signal input onto the cavity with quite a large angle, see Fig. 2.4(a). From the inset of Fig. 2.4(a) the dependence of phase shift is plotted (for the same range of angles as the main graph, 0 to 90 degrees). The dependence of phase shift on k_x^2 is shown to be linear for a wide range of angles, which is important for assumptions later in this thesis, see section 5.2. The reflectivity and transmissivity of a DBR are shown not to be strongly dependent on incident angle, see Fig. 2.4(b). The spectral dependence of the phase shift associated with reflection and transmission for the DBR is shown in Fig. 2.5(a). In practice the only part of the phase response which is of interest is the response around λ_B. It is shown in Fig. 2.5(b) that the deviation in phase shift around λ_B is linear with respect to changing wavelength. This is an important approximation which is used in theory to describe the phase response of a microcavity around resonance, see section 5.2. It can be seen from the response shown in Fig. 2.5 (b) that a DBR consisting of multiple mirror pairs produces a high reflectivity spectral region (stop band) which is centred on λ_B. The width of the stop band is dependent on the difference in refractive indices of the two layers of the mirror pair. By increasing the contrast in the refractive indices of the constituent mirror pairs of a DBR the stop band width can be increased.

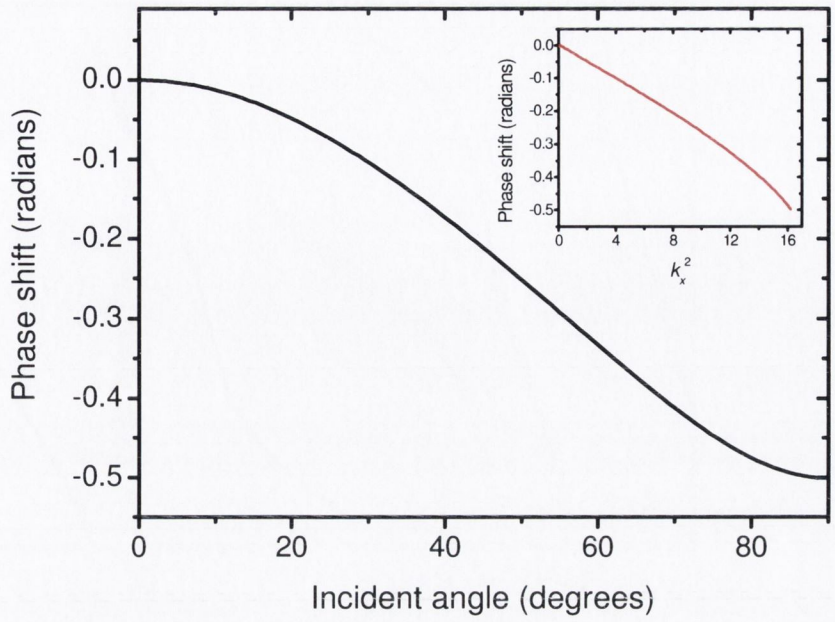

Fig. 2.4 (a) Dependence of phase shift on incident angle for a DBR with 20 GaAs/AlAs mirror pairs, λ_B= 1550 nm. Fig. 2.4 (a) (inset) Dependence of phase shift on k_x^2 a DBR with 20 GaAs/AlAs mirror, Phase shift is linearly dependent on k_x^2 for angles less than 50 degrees. 0 degrees for both graphs means the signal is normally incident on the DBR.

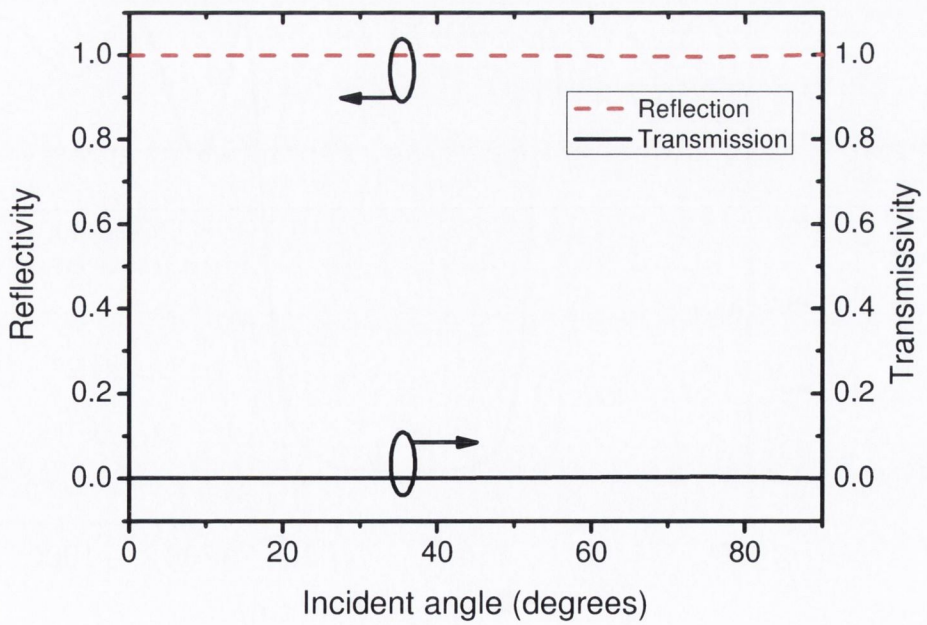

Fig. 2.4 (b) Angle dependence of reflectivity and transmissivity of a DBR with 20 GaAs/AlAs mirror pairs, λ_B = 1550 nm. 0 degrees means the signal is normally incident on the DBR.

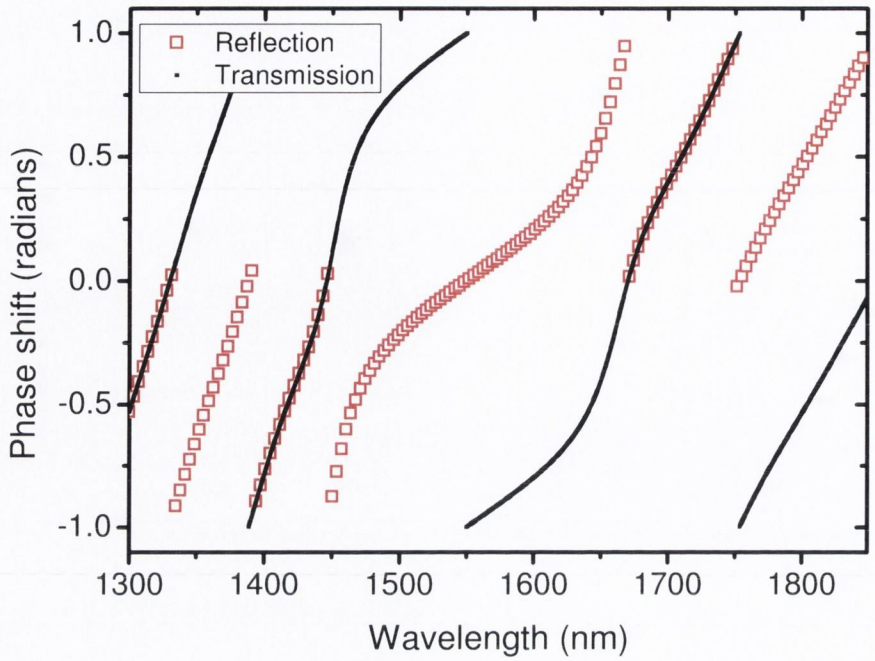

Fig. 2.5 (a) Spectral dependence of phase shift associated with reflection and transmission for a DBR with 20 GaAs/AlAs mirror pairs, λ_B = 1550 nm. The dependency on phase shift on wavelength around λ_B is shown to be linear.

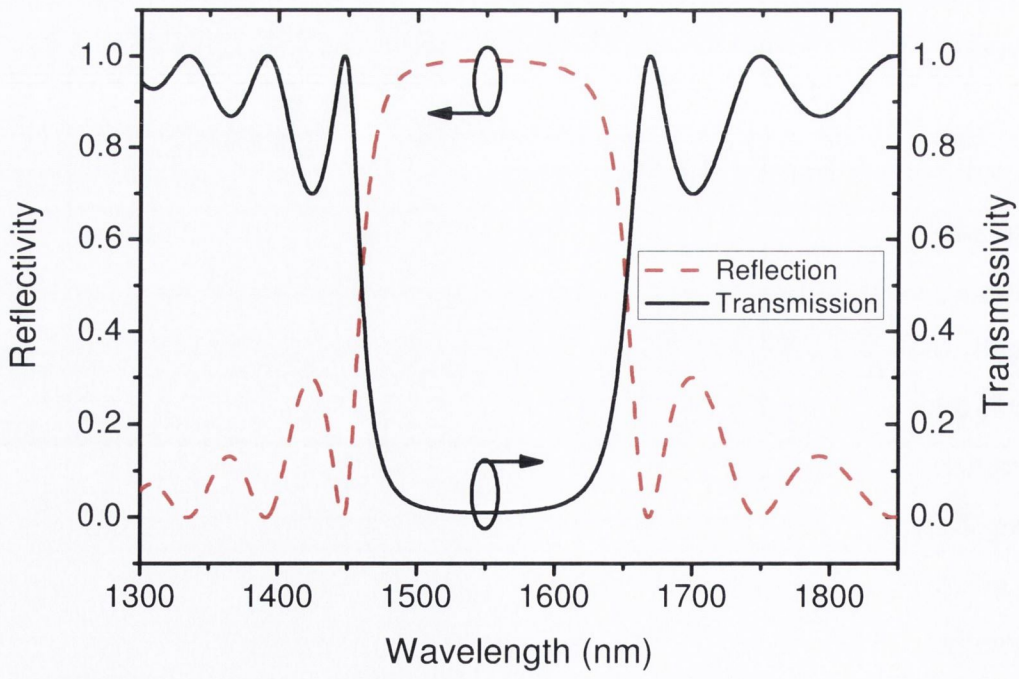

Fig. 2.5 (b) Spectral dependence of reflection and transmission for a DBR with 20 GaAs/AlAs mirror pairs, λ_B= 1550 nm. The high reflectivity region centred on λ_B is the cavity stop band.

2.1.6 Phase shift in a DBR

The mirror penetration depths $(d_{r_{1,2}})$ are extremely important as they must be taken into account when calculating the effective active region length. The phase shift associated with a DBR is quite complicated, and so for simplicity it is calculated in this thesis using the TMM. The phase response for a DBR with 20 GaAs/AlAs mirror pairs and λ_B = 1550 nm is shown in Fig 2.5. The phase shift dependence on wavelength is seen to be linear for a wide wavelength region (> 30 nm) around λ_B. Due to this linear phase response around λ_B the derivative of the phase response around λ_B can be used to describe the phase response for all wavelengths of practical interest in this work. The derivative of the phase response is related to $(d_{r_{1,2}})$ through (2.29).

2.2 Transverse matrix method

In order to explain the response of an etalon with a more complicated structures i.e. large numbers of mirrors it is convenient to use the TMM. A and B are defined as shown in Fig. 2.6. The definitions for the reflection and transmission coefficients are the same as those shown in Fig. 2.1.

A_i and B_i are the amplitudes of the waves travelling through L_i in the z and $-z$ directions respectively:

$$A_{i+1} = A_i t_{i,i+1} + B_{i+1} r_{i+1,i} \tag{2.34}$$

$$B_i = A_i r_{i,i+1} + B_{i+1} t_{i+1,i} \tag{2.35}$$

In order to rearrange (2.34) and (2.35) the Fresnel relations must be used

$$t_{i,i+1} t_{i+1,i} + r_{i,i+1} r_{i+1,i} = 1 \tag{2.36}$$

$$r_{i,i+1} = -r_{i+1,i} \tag{2.37}$$

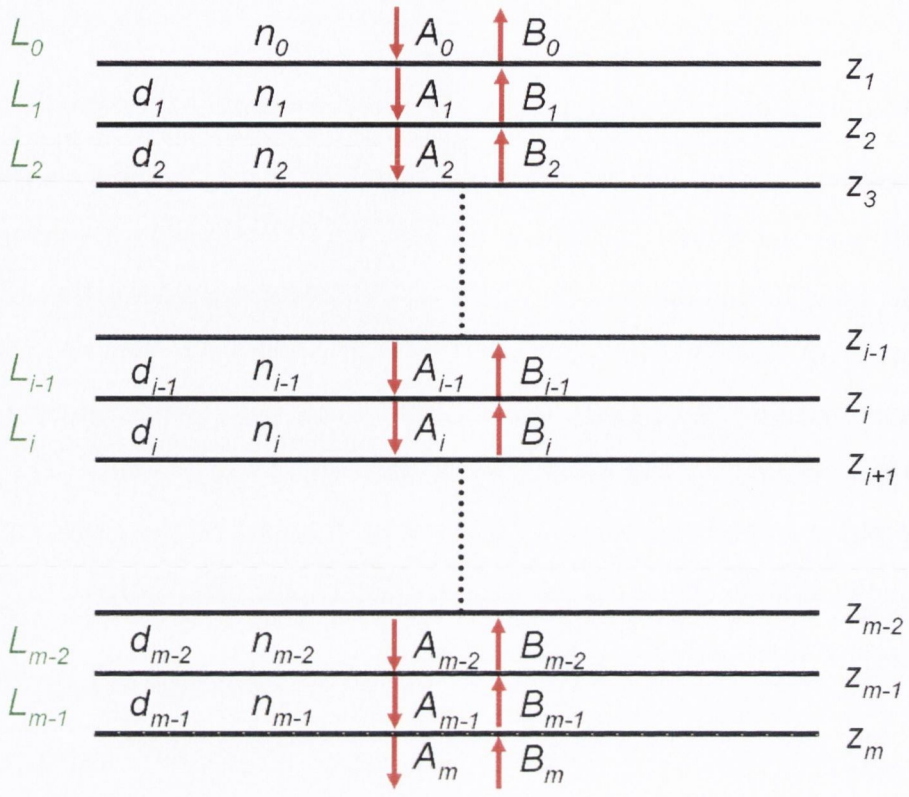

Fig. 2.6 Definition of variables used to define layer structure and transmission as used in definition of the TMM. A_i and B_i are the amplitudes of the waves travelling through L_i.

(2.34) and (2.35) can be expressed as

$$A_i = \frac{1}{t_{i,i+1}}\left(A_{i+1} - B_{i+1} r_{i+1,i}\right) \tag{2.38}$$

$$B_i = \frac{1}{t_{i,i+1}}\left(A_{i+1} r_{i,i+1} + B_{i+1}\right) \tag{2.39}$$

(2.38) and (2.39) can be expressed in matrix form as

$$\begin{bmatrix} A_i \\ B_i \end{bmatrix} = \frac{1}{t_{i,i+1}} \begin{bmatrix} 1 & r_{i,i+1} \\ r_{i,i+1} & 1 \end{bmatrix} \begin{bmatrix} A_{i+1} \\ B_{i+1} \end{bmatrix} = M_{i+1} \begin{bmatrix} A_{i+1} \\ B_{i+1} \end{bmatrix} \tag{2.40}$$

where M_{i+1} is the transfer matrix from L_i to L_{i+1}. When calculating the result of transitions through multiple layers the phase change due to propagation through the layers must be taken into account. The phase shift due to the signal transiting the space between boundary z_i and z_{i+1} is ϕ_i

$$\phi_i = k_{z_i} d_i = \beta n_i d_i = n_i d_i \cos\theta_i \frac{\omega}{c} \tag{2.41}$$

where θ_i is the incident angle for light incident on z_{i+1} from L_i, see Fig. 2.7, $\omega = 2\pi f$, f is the input signal frequency, k_i is the wave vector and is equal to $\beta_i n_i$, $\beta = \beta_0$, k_{z_i} is the z component of k

$$k_{z_i} = \sqrt{n_i^2 \beta^2 - (n_1 \beta \sin\theta_{inc})^2} \tag{2.42}$$

The effect of the phase shift on signals as they pass through the layers of a multi layer structure is taken into account by calculating a propagation matrix P_i for each of the layers (L_i)

$$P_{i+1} = \begin{bmatrix} e^{i\phi_{i+1}} & 0 \\ 0 & e^{-i\phi_{i+1}} \end{bmatrix} \tag{2.43}$$

The minus sign in $P_i(2, 2)$ is due to the signal travelling in the - z direction. The propagation through a series of layers can be represented in matrix form as

$$\begin{bmatrix} A_i \\ B_i \end{bmatrix} = M_{i+1} P_{i+1} M_{i+2} \begin{bmatrix} A_{i+2} \\ B_{i+2} \end{bmatrix} = \begin{bmatrix} F_{11} & F_{12} \\ F_{21} & F_{22} \end{bmatrix} \begin{bmatrix} A_m \\ B_m \end{bmatrix} \tag{2.44}$$

F is the matrix which describes the effect of the propagation through the entire multi layer structure.

In order to calculate M_{i+1} as defined in (2.44) r_i and t_{i-1} must be calculated using (2.1). In practice it is easier to implement the TMM by expressing the Fresnel equations (2.1) in terms of k_z:

$$r_{i,i+1} = \frac{n_i \cos\theta_i - n_{i+1} \cos\theta_{i+1}}{n_i \cos\theta_i + n_{i+1} \cos\theta_{i+1}} = \frac{k_{z_i} - k_{z_{i+1}}}{k_{z_i} + k_{z_{i+1}}} \tag{2.45}$$

$$t_{i,i+1} = \frac{2 n_i \cos\theta_i}{n_i \cos\theta_i + n_{i+1} \cos\theta_{i+1}} = \frac{2 k_{z_i}}{k_{z_i} + k_{z_{i+1}}} \tag{2.46}$$

(2.45) and (2.46) can be substituted back into (2.44)

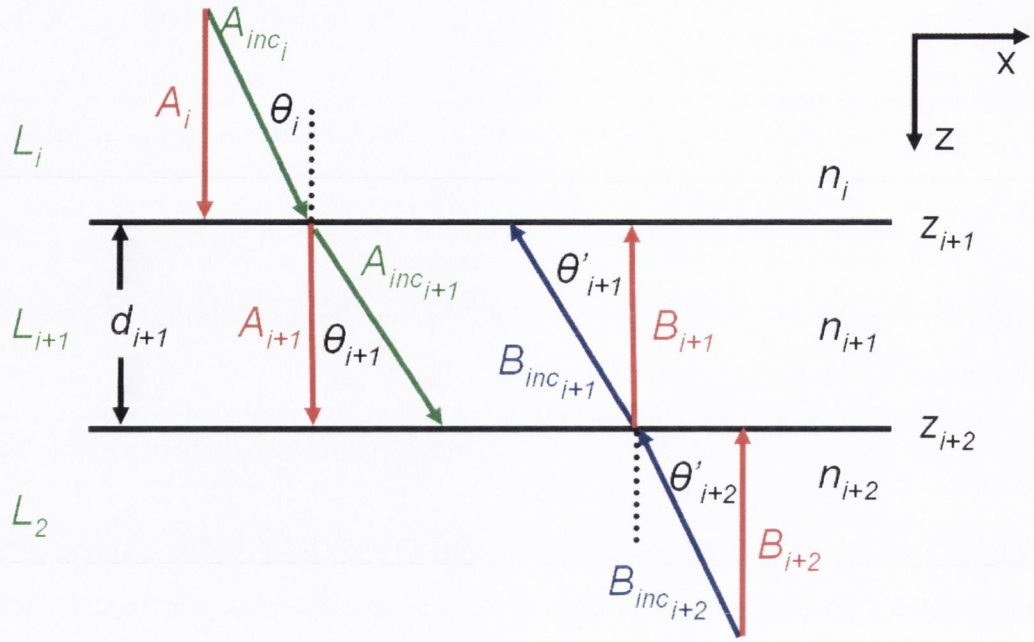

Fig. 2.7 Definition of variables used to define layer structure and transmission as used in definition of the TMM.

The reflectivity and the transmissivity of the multi layer structure is calculated by letting B_m equal to zero, which can be done because there are no more layers to reflect light back into the cavity after z_m

$$A_0 = F_{11} A_m \tag{2.47}$$

$$B_0 = F_{21} A_m \tag{2.48}$$

From (2.34) and (2.35) the reflection (r) and transmission (t) coefficients for the multi layer structure can be calculated

$$r = \frac{B_0}{A_0} = \frac{F_{21}}{F_{11}} \tag{2.49}$$

$$t = \frac{A_m}{A_0} = \frac{1}{F_{11}} \tag{2.50}$$

The reflectivity and transmissivity of the multi layer structure can be described as

$$R = |r|^2 \tag{2.51}$$

$$T = \frac{k_{z_m}}{k_{z_0}} |t|^2 \tag{2.52}$$

Both r and t are complex variables whose phase angle gives the phase change due to reflection and transmission respectively for the multi layer structure.

3. Two-photon absorption microcavity detector

3.1 Basic principle

The detector used to carry out TPA based monitoring in this work is a TPA microcavity (TPAM) [71, 72]. The TPAM's which have been used consist of two highly reflective DBR's between which is sandwiched a one λ thick active region, see Fig 3.1. The response of such a structure is explained by calculating the response of each DBR individually (reflection, transmission and phase shift) using the TMM, see section 2.2. Then each DBR is treated as a single mirror and so the cavity can be described using etalon theory, see section 2.1.

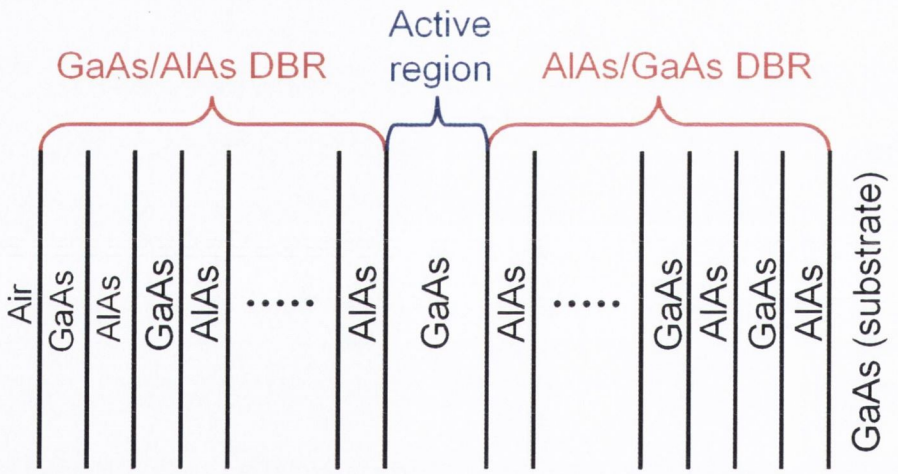

Fig. 3.1 Schematic of a microcavity structure consisting of top and bottom DBR's with 20 and 20 GaAs/AlAs mirror pairs. The active region is 1 λ_B thick.

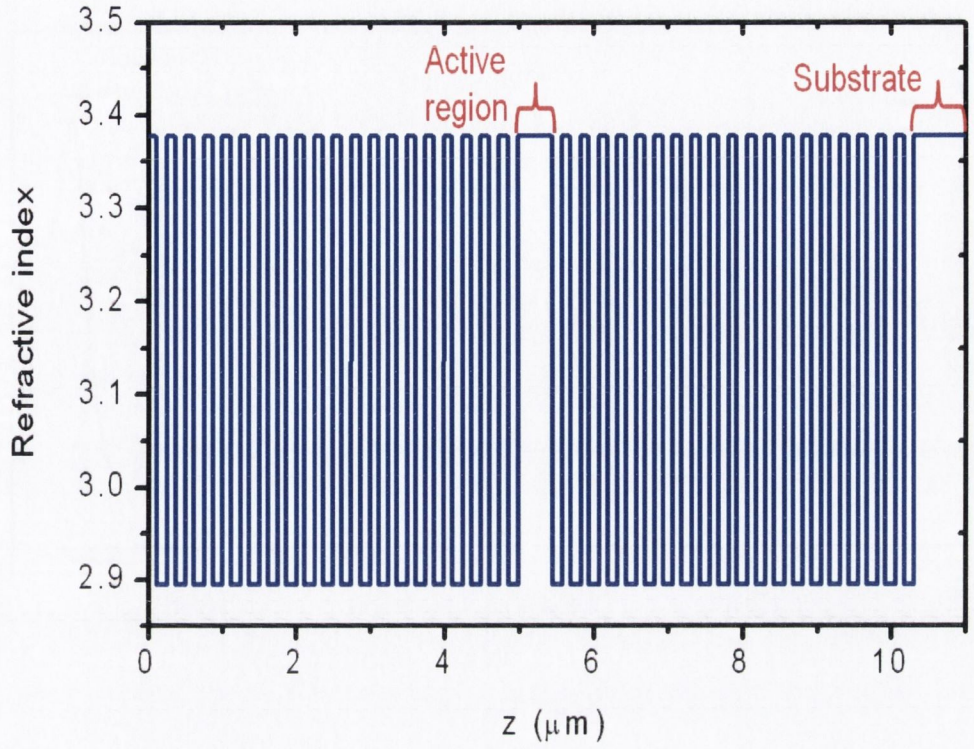

Fig. 3.2 Refractive index distribution for of a TPAM consisting of top and bottom DBR's with 20 top and 20 bottom GaAs/AlAs mirror pairs. The active region is a 1 λ_B thick GaAs layer. Position 0 μm corresponds to the air interface of the microcavity.

The refractive index distribution of such a structure is shown in Fig. 3.2. The effect of the 1 λ_B thick active region is to produce a narrow wavelength region in the stop band centred on λ_B which has low reflectivity (cavity resonance). The device structure shown in Fig. 3.2 has $R_{1,0}$ and $R_{1,2}$ values of 0.9976 and 0.9917 respectively, see Fig 3.3(a). The shape of the reflectivity and transmission response around λ_B has the same shape as a Lorentzian function; see Fig. 3.3(b).

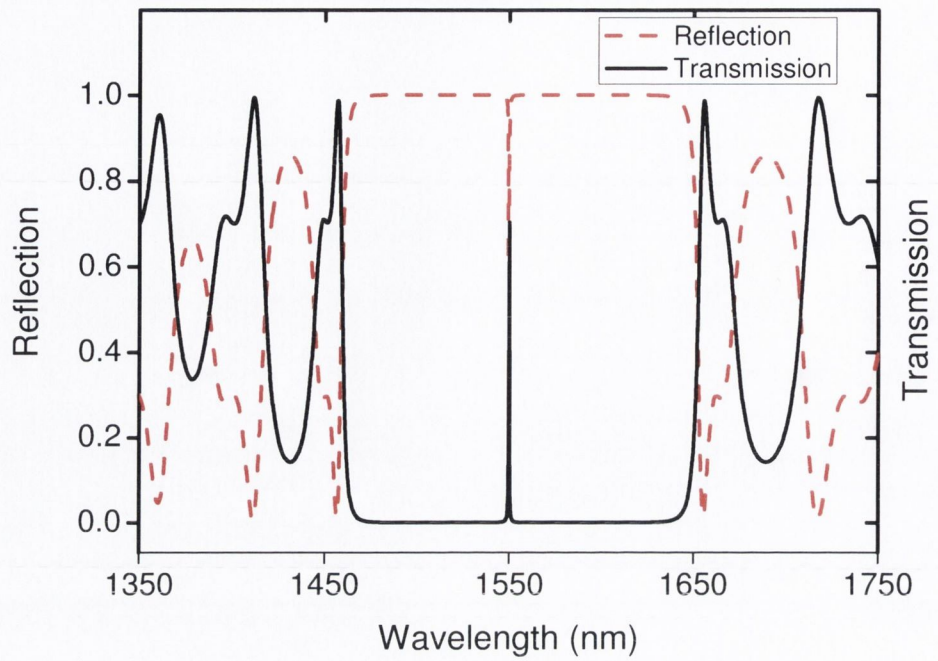

Fig. 3.3 (a) Reflectivity and transmissivity dependence of a TPAM consisting of 20 top and 20 bottom GaAs/AlAs DBR mirror pairs. The active region is 1 λ_B thick.

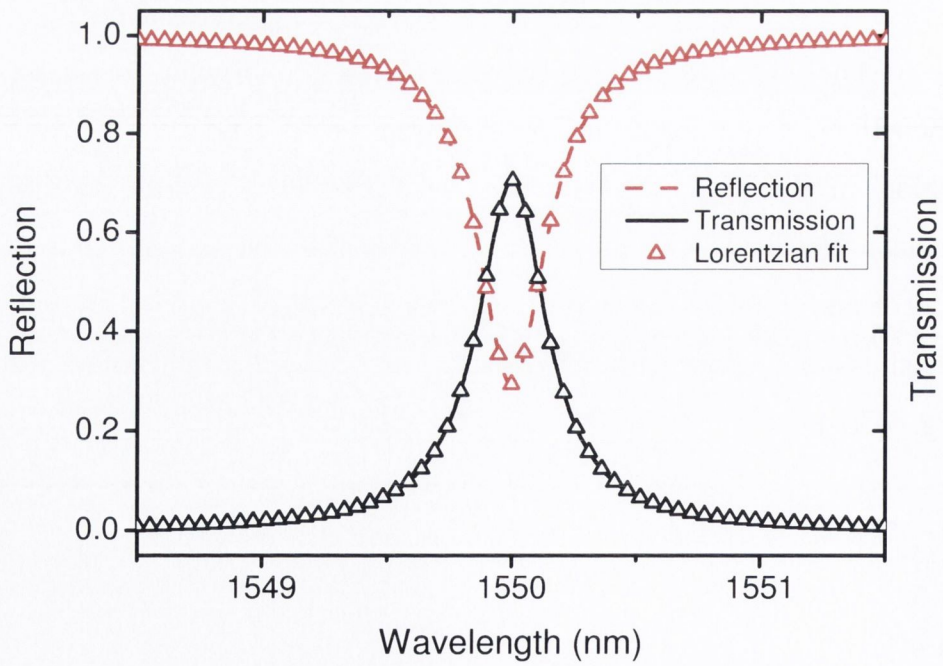

Fig. 3.3 (b) Reflectivity and transmissivity dependence of a microcavity for a narrow wavelength region centred on the λ_B. The TPAM consists of 20 top and 20 bottom GaAs/AlAs DBR mirror pairs. The active region is 1 λ_B thick.

The FWHM of the spectral response of the reflection and the transmission (cavity bandwidth) is given by (2.25). This equation shows that the FWHM of the spectral dependence of the cavity reflection and transmission spectra is dependent on the product of the reflection and transmission of the top and bottom DBR's. Increasing the reflectivity of the entire cavity (R) results in a decrease in the FWHM of the reflection/transmission response of the cavity. The reflection of the cavity at resonance is minimised by balancing the cavity, which means matching the front and back mirror reflectivities (set $R_{0,1}$ equal to $R_{1,2}$). It can be seen in Fig. 3.3(b) that even though the top and bottom DBR's of the simulated cavity are identical the cavity is not completely balanced (reflectivity does not reach 0 at λ_B). The cause of this imbalance is that the top DBR has an air interface while the bottom mirror has an interface with a GaAs substrate. If the substrate were removed (leaving the bottom DBR with an air interface) then the reflectivity at resonance for this structure would be 0. In practice the minimum reflectivity of the microcavity is not important in relation to TPA based detection as we are only interested in the enhancement of the electric field and the cavity bandwidth. It is also important to note that due to growth considerations that the response of grown TPAM structures will not exactly match the theoretical response as described above. The main difference is in the reflectivity of the DBR's which in practice is slightly lower reflectivity that suggested by the theory. Due to this the reflectivity of the devices must be calculated experimentally.

3.2 Electric field

The benefit of using a TPAM is that it results in a large enhancement of the optical field in the active region of the cavity. The electric field in a TPAM can be calculated for the entire structure using the TMM, see section 2.2. The electric can be described as a standing wave:

$$E_i = exp(-ik_{z_i} d_{z_i}) + exp(ik_{z_i} d_{z_i}) \tag{3.1}$$

where k_{z_i} is the value of k_z in the layer i, d_{z_i} is the distance from z_i in the z direction. The field builds up in the cavity relative to the input field and is greatest in the active region, see Fig. 3.4. It can be seen in Fig. 3.4 that the enhancement of the electric field in the active region relative to the input optical field is approximately 10. In Fig. 3.4 positions below 0 μm correspond to the air interface of the cavity and positions greater than approximately 5.75 μm correspond to the substrate under the bottom mirror of the cavity. As the generated TPA photocurrent is proportional to E^4 this means that the level of TPA in this microcavity structure is enhanced by approximately 10,000 times relative to the non-cavity case.

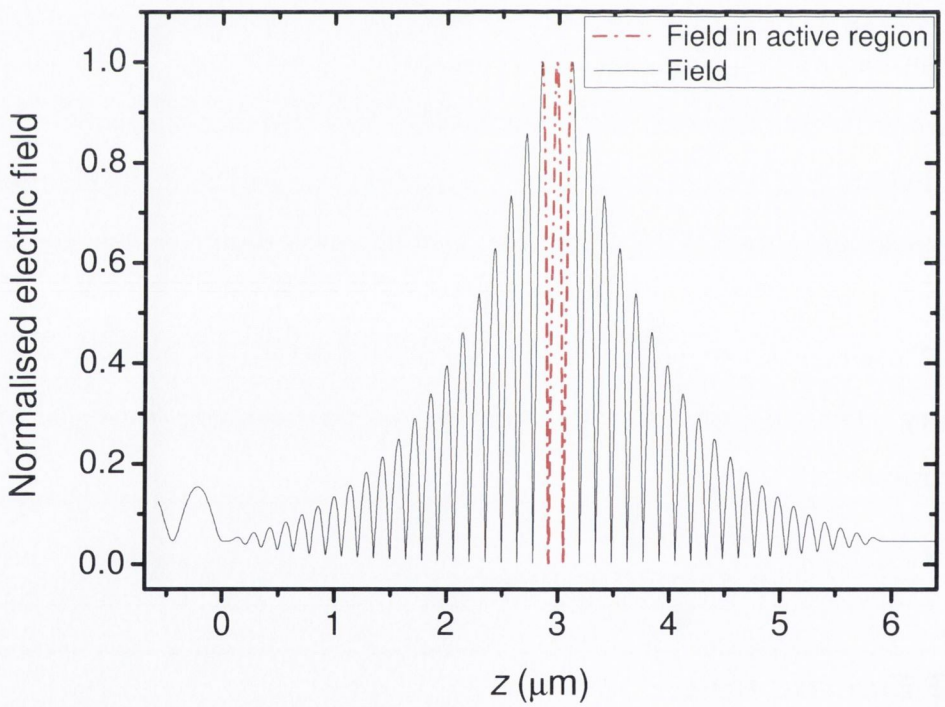

Fig. 3.4 Distribution of absolute of E in structure consisting of top and bottom DBR's with 20 and 20 GaAs/AlAs mirror pairs. The active region is a 1 λ_B thick GaAs layer. The dashed line shows E for the active region. 0 μm corresponds to the Air/TPAM interface.

The level of enhancement of the optical field in the active region of the cavity can be worked out using etalon theory, see section 2.1.3. In order to maximise

the level of enhancement in the cavity there are two requirements. Firstly the value of R for the cavity must be as close to one as possible. Secondly the value of $R_{1,2}$ must be as high as possible as the enhancement of the cavity has a stronger dependence on $R_{1,2}$ than on $R_{0,1}$ due to the presence of $R_{1,2}$ in the numerator of (2.18).

As the level of SPA is proportional $|E^2|$ and TPA is proportional to $|E^4|$ this means that the level of enhancement for both SPA and TPA in the TPAM can differ by orders of magnitude, see chapter 4. The ratio of the level of SPA to TPA generated in a microcavity is found by integrating $|E^2|$ and $|E^4|$ across the cavity length $d_{z_{act}}$, where $d_{z_{act}}$ is the thickness of the active region in the z direction which for a 1 λ_B GaAs region at 1550 nm which corresponds to a physical thickness of 459 nm.

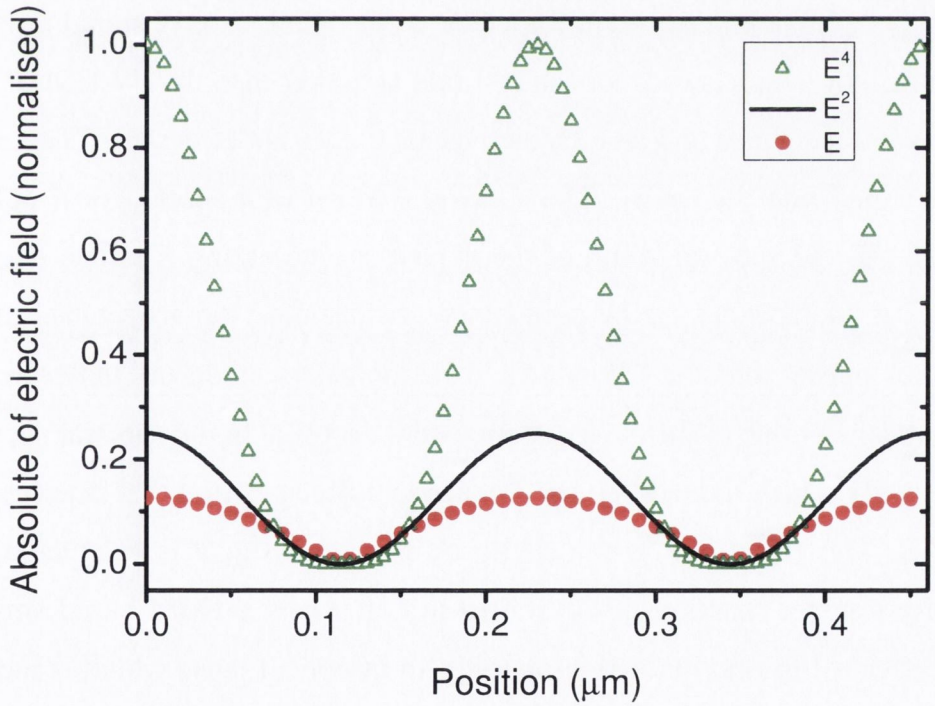

Fig. 3.5 Distribution of absolute value of E, E^2 and E^4 in a TPAM structure consisting of top and bottom DBR's with 20 and 20 GaAs/AlAs mirror pairs. The active region is a 1 λ_B thick GaAs layer. The position at the interface between the top DBR and the active region is set as 0 μm. All curves are normalised by the peak of E^4.

3.3 Cavity lifetime

The case for cavity enhancement as explained in section 2.1.3 is only completely valid for CW incident signals. For CW incident signals higher values of R generate larger field enhancement in the cavity. This is not necessarily the case for incident optical pulses [74].

The incident field inside needs several round trips inside the cavity in order for the intensity to build up inside the cavity. For cavities, the rise time for the build up of the intensity increases as R increases. After a period of intensity build-up in the cavity the intensity will reach a saturation point which is dependent on R. Higher values of R correspondingly leads to the cavity saturating at increasingly high intensities. For short optical pulses the pulse duration can be shorter the cavity saturation time. This results in the cavity not reaching the saturation intensity and as such the level of enhancement for these pulses is less that the level of enhancement for a CW input signal. A CW signal in general has a linewidth which is orders of magnitude narrower than the FWHM of the cavity spectral acceptance and as such increasing R does not affect the acceptance of the CW signal into the cavity. The spectral FWHM of a short optical pulse can be similar to the spectral width of the cavity. So increasing R which decreases the spectral width of the cavity acceptance can decrease the acceptance of the short optical pulses into the cavity. As such there is a trade off between increased enhancement due to the cavity lifetime and decrease in the spectral acceptance of the cavity which reduces the portion of the pulse spectrum that is accepted by the cavity. The effect due to the cavity on the input signal is calculated using the cavity transfer function [74]. Shown in Fig. 3.6 is a TMM based simulation of the effect of the cavity on a temporally short optical pulse which is incident on a microcavity with R = 0.95 (both pulses have been normalised to their peak intensity in the cavity. The effect of the cavity in broadening an incident pulse can be clearly seen. For larger overall cavity reflectivities this broadening will increase.

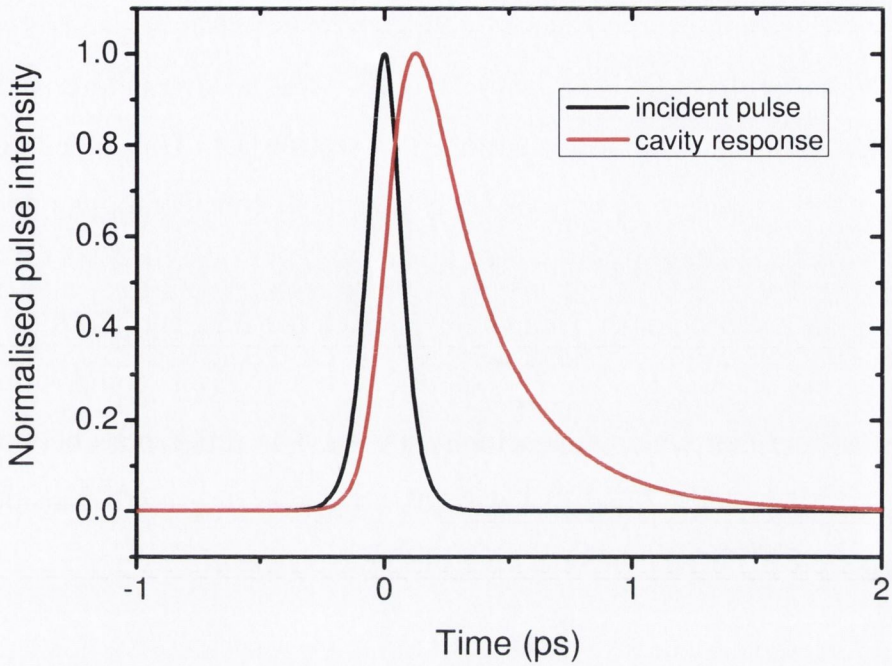

Fig. 3.6 Pulse shape in time domain with and without the influence of a cavity. Simulated cavity has R= 0.95. Both pulses have been normalised to their peak intensity in the cavity.

3.4 Our devices

3.4.1 Layer structure

The TPAM's with which the majority of work in this thesis was carried out were both commercially grown and commercially processed. The growth was carried out by IQE (Europe) Ltd a commercial grower based in Cardiff. The processing was carried out by Compound Semiconductor Technologies Global Ltd (CST) which is based in Cardiff.

For the work in this thesis two different TPAM's have been used. Both devices are identical except that one set of devices had an extra six mirror pairs in its top DBR. Both sets of TPAM's were grown using metalorganic chemical vapour deposition (MOCVD). The extra six mirror pairs increase the cavity

lifetime of the second set of devices. The reflectivities of both sets of microcavity devices were optimised for use with 2 ps and 8 ps pulses respectively, see section 3.3. The layer structure is shown in Fig. 3.7. The layer structure is slightly more complex than the structures mentioned in section 3.1. This added complexity is present for a number of reasons such as growth considerations and an effort to reduce the level of SPA in these devices.

Other than layers number 10 and eleven both the 2 ps and the 8 ps microcavity devices are identical. Fig. 3.7 shows both the layer composition that was specified and that which was actually grown. The differences between the layer composition specified and that was grown is due to growth considerations and does not greatly affect the operation of these devices.

Layer No	Material	Group	Repeat	Start X	Finish X	PL(nm) T (um)	Doping (cm-3) Specified	Doping (cm-3) Actual	Dopant
13	GaAs					0.1156	**>1E+19**	2.5E+19	Carbon
12	AlAs					0.1348	**3E+18**		Carbon
11	Al(x)GaAs	3	**6**	**0.12**		0.1178	**1E+18**		Carbon
10	AlAs	3	**6**			0.1348	**1E+18**	7E+17	Carbon
9	GaAs	2	**6**			0.1156	**3E+17**		Carbon
8	AlAs	2	**6**			0.1348	5E+17		Carbon
7	Al(x)GaAs			**0.6**		0.1268	3E+17		Carbon
6	AlAs					0.1348			None
5	GaAs					0.4625			None
4	AlAs					0.1348	**1>0.5e18**		Silicon
3	Al(x)GaAs			**0.6**		0.1268	**1E+18**		Silicon
2	AlAs	1	**23**			0.1348	**1E+18**	1.2E+18	Silicon
1	GaAs	1	**23**			0.1156	**1E+18**		Silicon

Fig. 3.7 Layer composition for microcavities optimised for 2 ps and 8 ps. Layer numbers 10 and 11 are only present in the 8 ps devices.

The devices were grown on a Silicon doped 625 μm thick GaAs substrate. The λ_B for these devices is specified as being 1560 nm. Layer 1 and 2 is a GaAs/AlAs mirror pair which is repeated 23 times in order to give the bottom DBR of the TPAM's high reflectivity. The relatively high doping level in these layers ($1E^{18}$ cm^{-3}) is to aid carrier transport. In layer 3 there is a high level of Al present in

order to increase the size of the bandgap and so decrease the level of any possible SPA. The doping present in layer 4 is in order to overcome residual p-doping in the material. Layer 5 is the un-intentionally doped active region. The active region is 1 λ_B thick. Layer 6 is un-doped in order to prevent dopant going into the active region. The aim of this is to try and limit the level of SPA in these devices. In layer 7 there is a high level of Al present in order to increase the size of the bandgap and so decrease the level of any possible SPA. Layers 8 and 9 have slightly lower doping in order to decrease the level of residual SPA. Layers 10 and 11 are only present in the 8 ps cavity, they are used to increase the top mirror reflectivity and so increase the cavity lifetime. The higher doping is present to improve the carrier transport through these layers. The doping can be higher in these layers than in layers 8 and 9 as they are well away from the active region and as such any residual SPA is unlikely to result in detected photocurrent. Al is present in these layers in order to allow for the increase in doping (this is a growth issue). Layers 12 and 13 are highly doped in order to allow for ohmic bonding.

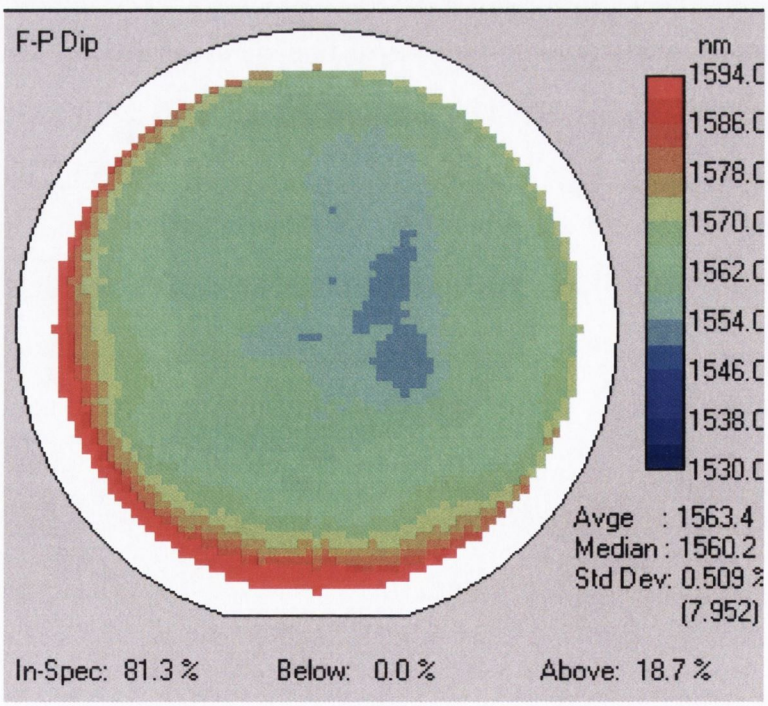

Fig. 3.8 Reflectivity map of an 8 ps microcavity wafer. The legend indicates the resonance position of the TPAM for different positions on the wafer (minimum reflectivity in the stop band of the TPAM). Reflectivity map provided by IQE.

The principal means of checking whether the devices matched the design specifications is by looking at the measured reflectivity of the devices. In Fig. 3.8 the value of λ_B of the grown cavity for different positions around the 3 inch wafer are shown. It can be seen that the actual value of λ_B varies by as much as 50 nm around the wafer. This means that a single growth provides a set of TPAM's with a range of different resonant wavelengths.

3.4.2 Processing

One of the benefits of using a TPAM as a TPA detector is that the processing required is not difficult. The processing was carried out commercially by CST. The processing requires deposition of SiO_2 on the top of the TPAM which acts as an electrical insulator. The SiO_2 layer is etched-off the top layer for the aperture opening, see Fig. 3.9. A gold layer is then deposited around the aperture which is used as an electrical contact (p-contact), while the bottom of the TPAM which is attached to a metal can (TO can) that operates as an n-contact. Devices are processed to have 3 different aperture sizes (20 μm, 50 μm and 100 μm).

The 4 μm etch pit is designed to be deep enough to pass through the spacer region of the cavity and so mean only light passing through the device aperture is capable of contributing to the generated photocurrent from the detector.

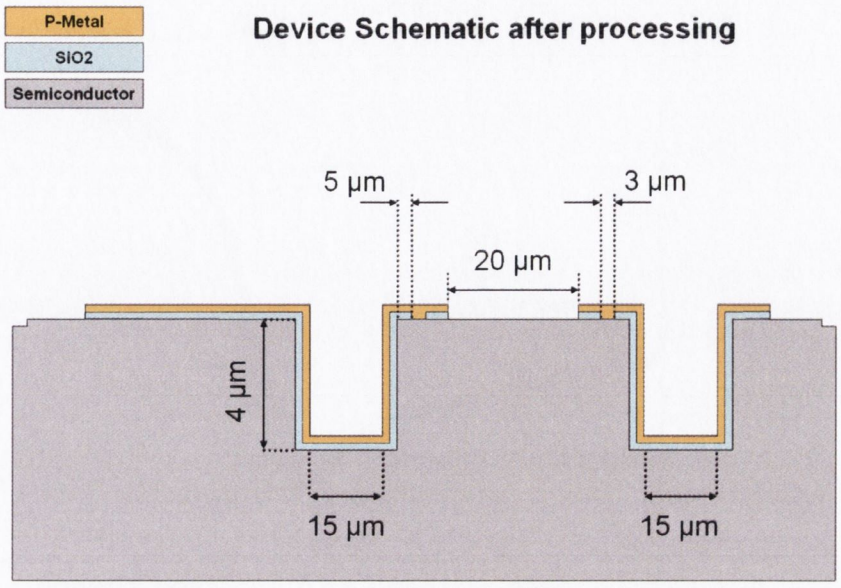

Fig. 3.9 Schematic of processing carried out by CST in order to create apertures and electrical contacts for TPAM. Schematic was provided by CST. The 4 µm etch pit passes through the cavity spacer region.

3.4.3 Diode characteristics

The TPAM is a p-i-n diode. Photodetectors based on p-n junctions have been investigated as high speed photodetectors for many years [75]. The top and bottom DBR's are the p- and n- junctions respectively. The diode behaviour of a TPAM has been characterised by testing the current vs. bias dependence with no light incident on the TPAM, see Fig. 3.10. The circuit used to investigate the bias dependence of the TPAM is shown in Fig. 3.11. The Ammeter used is a Keithley picoammeter. The main information that can be garnered from the bias dependence of the TPAM is its series resistance.

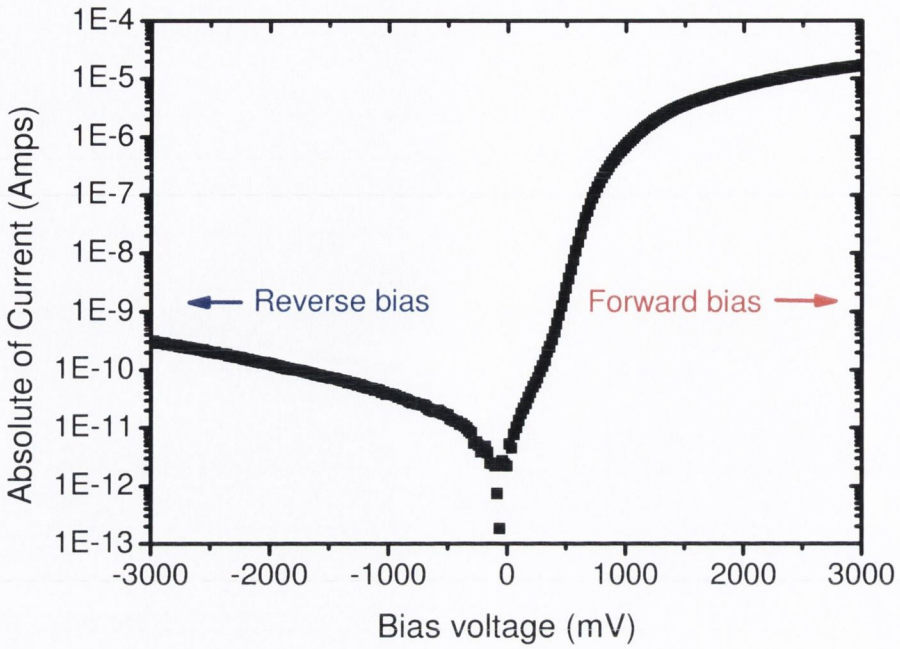

Fig. 3.10 Voltage vs. current curve for 8 ps microcavity, positive voltage refers to forward bias. No light is incident on detector during scan.

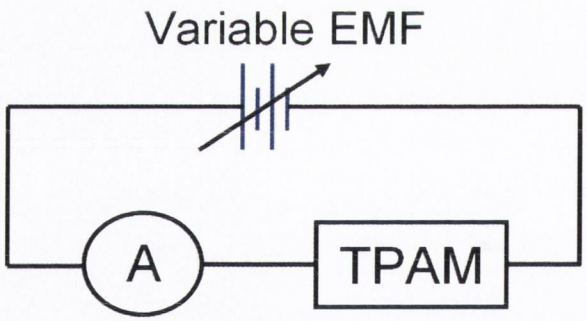

Fig. 3.11 Schematic of circuit used in order to investigate current vs. voltage response of a TPAM. A is a picoammeter.

The series resistance is calculated from the linear dependence of generated current on voltage after the diode is turned on, see Fig. 3.12. The slope of Fig. 3.12 which is a plot of voltage vs. generated current gives the series resistance of the TPAM which for the TPAM under test here is 110 kΩ. Similar VCSEL structures have reported with series resistances of the order of 100 Ω [76, 77]. With their low resistance having been achieved by grading the material interfaces

in their mirror pairs which reduces the series resistance associated with band edge discontinuities at the material interfaces as well using higher doping [78]. Similarly we have achieved a large decrease in series resistance by grading our interfaces although these devices are not used in the work presented here as the device speed is not a limitation in any of this work

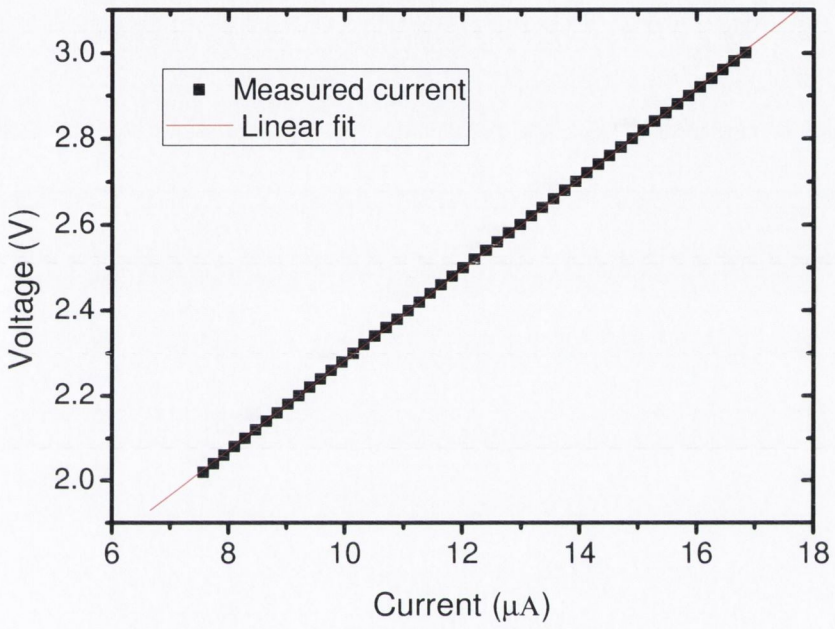

Fig. 3.12 Linear fit of diode response after diode is "turned on".

3.4.4 Difference between designed cavity response and actual response

The two sets of TPAM's used in this cavity were designed cavity lifetimes of 2 ps and 8 ps. The way the cavity lifetime of the grown TPAM's is calculated is by finding the cavity bandwidth and comparing it to the cavity of the designed structure. The devices we have grown it turns out have cavity bandwidths that are broader than anticipated from TMM modelling of these structures. The deviation from the theoretical cavity response is due to loss in the structures. In practice

this is not of importance for this work as all calculations are based on the measured cavity bandwidth.

4. SPA suppression

4.1 SPA and TPA enhancement

In order for a TPA detector to be used in carrying out OPM it must be capable of operating at as low an input optical power as possible. This is because, in general, the signal being tested will be less than 10 % of the signal power in the system under test. The power available (for test) depends on where in the network the monitor is to be placed, with it being possible for powers to range from 10 dBm to less than – 30 dBm. In practice these types of input optical powers are not a problem for linear detectors but pose a serious problem for TPA based detectors (including TPAM's). At these low input powers the influence of SPA on the detected signal becomes a serious issue, with the actual power at which problems occur also being related to the incident spot size, see chapter 5.

The primary reason for using a TPAM is in order to enhance the level of TPA, a calculation of the level of TPA enhancement is essential as a means of testing the usefulness of such a structure, see section 3.2 [71, 72]. As the level of TPA is dependent on $|E|_{act}^4$ while SPA is dependent on $|E|_{act}^2$ this results in a relative suppression of SPA relative to TPA in a TPAM [79], where $|E|_{act}$ is the absolute of the amplitude of the field in a active region of the TPAM. The field enhancement in a microcavity is derived in section 2.1.3. Using this description of field enhancement it is possible to investigate the level of enhancement of both SPA and TPA in a microcavity. The TPA (ζ_{TPA}) and SPA (ζ_{SPA}) enhancements are described as

$$\zeta_{TPA} = \frac{(1-R_{0,1})^2(1+R_{1,2}^2+4R_{1,2})}{(1-\sqrt{R_{0,1}R_{1,2}})^4} \tag{4.1}$$

$$\zeta_{SPA} = \frac{(1-R_{0,1})(1+R_{1,2})}{(1-\sqrt{R_{0,1}R_{1,2}})^2} \tag{4.2}$$

where the definitions of R are consistent with those in chapter 2.

4.2 SPA and TPA generated photocurrent

The generated SPA and TPA generated photocurrent can be described as

$$i_{TPA} = \frac{e}{2h\nu}\frac{Cl\beta P_{ave}^2}{Sd_{gen}} \tag{4.3}$$

$$i_{SPA} = \frac{e}{h\nu} C\alpha l P_{ave} \tag{4.4}$$

where e is the electron charge, S is the spot area, $h\nu$ is the photon energy, α and β are the SPA and TPA absorption coefficients respectively. C is the collection efficiency of the detector with a value of C = 1 corresponding to 100 % collection efficiency. P_{ave} is the average incident optical power, d_{gen} is the duty cycle of the incident optical signal [19] $d_{gen} = P_{ave}^2 / \overline{P(t)^2}$ where $P(t)$ is the optical power at time t.

Based on the definition of the level of enhancement by the TPAM it is possible to calculate the amount of optical power required in order for TPA to be the dominant absorption process (for TPA to exceed SPA)

$$P_{ave} > \frac{2\alpha S d_{gen}}{\beta}\frac{\zeta_{SPA}}{\zeta_{TPA}} \equiv \frac{2\alpha S d_{gen}}{\beta}\frac{1}{\xi} \tag{4.5}$$

where $\zeta = \zeta_{TPA} / \zeta_{SPA}$ and so ζ describes the relative suppression of SPA in a TPAM.

4.3 Experimental investigation of enhancement

The detector used for the investigation of the TPA and SPA enhancement are the cavities which are designed to have 8 ps cavities described in section 3.4, in practice what is considered is not the cavity lifetime but instead the reflectivity of the detector. The detectors designed to have 8 ps and 2 ps cavity lifetimes have overall reflectivities (R) of approximately 0.965 and 0.87. The difference in

enhancement between the $R = 0.965$ and 0.87 devices is investigated theoretically in section 3.5.3. The detector aperture is 20 μm in diameter. The measurement is carried out using a continuous wave (CW) widely tuneable laser (TLS), see Fig. 4.1. The signal is passed through an erbium doped fibre amplifier (EDFA) which allows for average optical powers greater than 50 mW to be incident onto the TPAM allowing the TPA dominated regime to be accessed for incident spot sizes which are larger than the 20 μm diameter of the TPAM under test. The signal is then passed through a variable optical attenuator (VOA) and a polarisation controller. 1 % of the output of the VOA is tapped off to an average power monitor (PD). The polarisation controller (PA) consists of an input polarizer and a half- and quarter-wave plate. The polarisation controller is needed due to the polarisation dependence of the TPA process which is investigated for these TPAM's in chapter 6 [80]. The polarisation for these measurements is controlled using the PA so as to maximize the level of TPA and is then kept constant throughout the measurement. The generated TPA photocurrent is measured using a Keithley 6485 picoammeter.

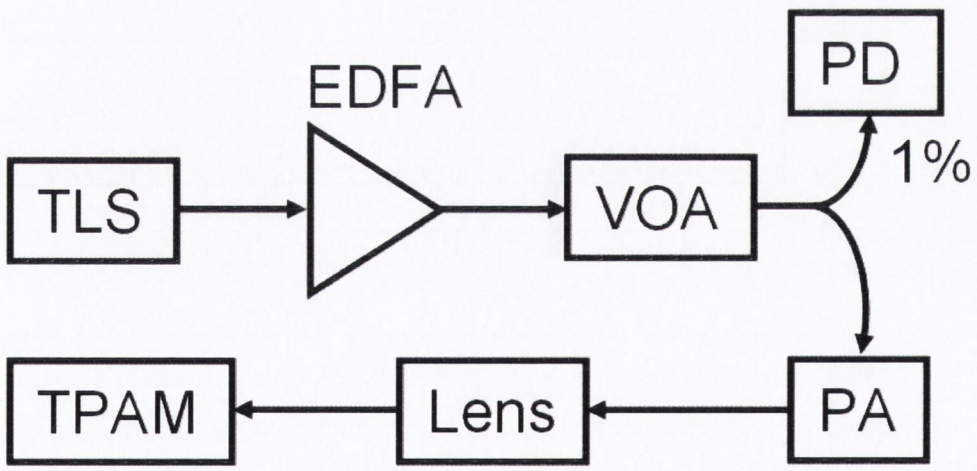

Fig. 4.1 Experimental setup for investigation of microcavity enhancement. TLS is a tuneable CW laser, VOA is a variable optical attenuator, PD is a InGaAs photodiode used as an average power meter, PA is a polarisation controller, EDFA is an erbium doped fiber amplifier an the Lens produces a ~ 3.5 μm focused spot on TPAM.

The cavity spectrum is first measured using a defocused spot which is much larger than the detector aperture, see section 3.4.2. With such a large incident spot size the input Gaussian beam can be treated as a collimated beam. The spectral dependence is measured by scanning the TLS wavelength while keeping the incident optical power constant, see Fig. 4.2. The incident power is selected to ensure that the TPA and SPA dominant regimes can be accessed, which for this defocused case corresponds to average powers of 5.84 mW and 0.2 mW respectively.

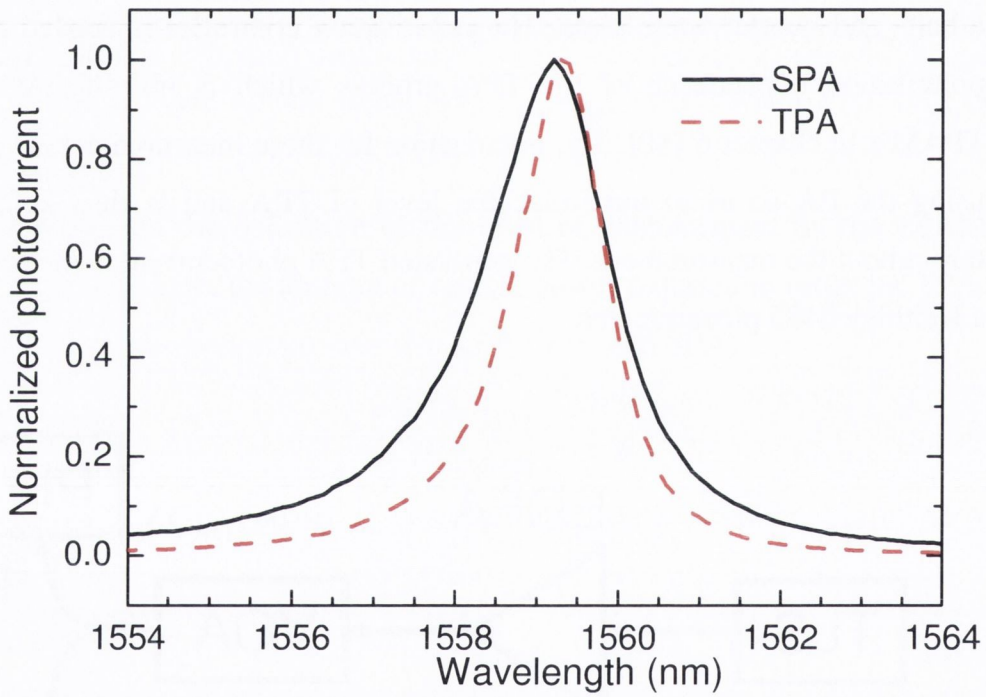

Fig. 4.2 Cavity spectral dependence for TPA and SPA dominant regimes respectively with a nearly collimated input signal The TPA and SPA dominated absorption regimes correspond to input optical powers of 5.84 mW and 0.2 mW respectively.

The full-width at half-maximum (FWHM) of the SPA spectral dependence is 1.88 nm, compared with 1.32 nm for the TPA spectral dependence. The TPA spectral width is exactly $\sqrt{2}$ times less than the SPA spectral width. This ratio in spectral widths is due to the TPA depending on $|E|^4_{act}$ while the SPA signal

depends on $|E|^2_{act}$. The practical effective cavity length is assumed to be the same as the design value, which is 2.04 μm. From the SPA spectral width R is found to be 0.965. As shown in section 3.2, even with R kept constant, the distribution of $R_{0,1}$ and $R_{1,2}$ will still influence the level of enhancement in a microcavity. For the TPAM under test $R_{1,2}$ is designed to be very close to 1 and so has a larger number of mirror pairs than the top mirror. In practice, because the loss due to absorption in the p-doped top mirror is assumed to be much higher than in the n-doped bottom mirror, the bottom mirror reflectivity is taken as being closer to the design value than the top mirror. So it is estimated that $R_{1,2}$ is between 0.98 and 0.99. A value of 0.985 for $R_{1,2}$ is taken here which means $R_{0,1}$ is approximately 0.945. Based on these estimations, the TPA and SPA enhancement can be calculated from (4.1, 4.2) as being 11,600 and 90 respectively. ξ based on these estimated values of enhancement is approximately 130 times.

The above estimate is slightly simplified, in order to fully characterise the level of SPA suppression in a microcavity the effect of the limited acceptance angle must be taken into account, see chapter 5. The acceptance angle of the planar microcavity is defined as being the angle away from normal incidence which causes the intensity inside the cavity to drop by a factor of two relative to the normal incidence case. The acceptance angle which is directly related to the cavity spectral width is estimated to be 12.7 degrees. The lensed fibre used to focus the input optical signal onto the microcavity generates a Gaussian beam with a minimum beam waist of approximately 3.5 μm which corresponds to a divergence angle of 16.1 degrees. The beam waist is the distance from the central axis of the beam at which the field amplitude drops off by a factor of $1/e$ relative to its amplitude on the central axis.

The incident signal onto the microcavity is then tightly focused with the in-focus position being taken as the one which maximises the TPA generated photocurrent. The spectrum is again recorded for TPA and SPA dominant regimes corresponding to P_{avg} of 1.3 mW and 4.6 μW, respectively, see Fig. 4.3. It can be seen from Fig. 4.3 that the spectral dependence is asymmetric. The

observed asymmetry is due to the limited acceptance of the microcavity, see chapter 5. Due to the limited acceptance angle of the planar microcavity, input angular components, which are increasingly far away from normal incidence, undergo decreased enhancement in the microcavity. This is because different components of the beam will not simultaneously be resonant with the cavity and so the combined effect of this is that the average enhancement of the entire incident beam is decreased. Using the theory as explained in chapter 5, the decrease in the enhancement for TPA and SPA is calculated as being 71 % and 32 % respectively.

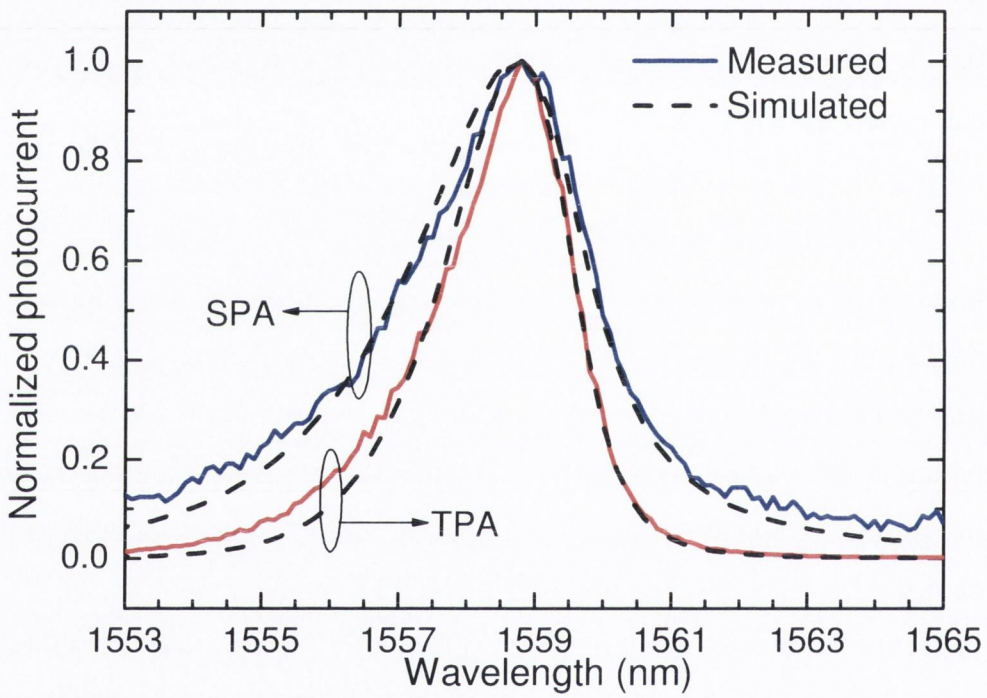

Fig. 4.3 Measured and simulated spectral dependence for TPA and SPA dominated regimes respectively with a tightly focused input signal. The TPA and SPA dominated absorption regimes correspond to input optical powers of 1.3 mW and 4.6 μW respectively.

With the incident wavelength corresponding to the peak wavelength from the spectrum in Fig. 4.3, the photocurrent dependence on CW incident power was measured, see Fig. 4.4. Fig. 4.4 is fit using a second order polynomial which

allows for the calculation of the current generated in a TPAM for a particular input optical power

$$i(nA) = 3.70P^2(mW) + 0.33P(mW) \tag{4.6}$$

which means that for an input of 0.09 mW the generated TPA and SPA photocurrent are equal. Using (4.1) with the decrease in enhancement taken into account, the TPA coefficient is 14.6 cm/GW (with the collection efficiency assumed to be 100 %).

In order to test the accuracy of the above reported value of β it is possible to compare it to previously reported values of β. In [11] the measured TPA coefficient of (001)-GaAs at 950 nm is between 20 cm/GW and 27 cm/GW, where 20 cm/GW is for linear polarisation along the (100) direction which describes the strength of the TPA in the isotropic limit [23], and 27 cm/GW is for linear polarisation along the (110) direction which represents an anisotropic factor of -0.76, see chapter 6. The wavelength dependence of the TPA coefficient is described by [81]

$$F\left(\frac{2h\nu}{E_g}\right) = \left(\frac{2h\nu}{E_g} - 1\right)^{\frac{3}{2}} \left(\frac{2h\nu}{E_g}\right)^{-5} \tag{4.7}$$

where E_g is the direct band gap energy of GaAs. (4.7) is based on a curve fitting of the β response for an isotropic band structure. Using (4.7) β is estimated with in the isotropic limit in (001)-GaAs at 1560 nm as 12.5 cm/GW. The anisotropic factor at 1560 nm of - 0.38 is used, see chapter 5 [23]. β for light polarized along the (110) direction at 1560 nm is then 14.8 cm/GW which agrees well with the experimentally found value of β reported above. In [82] a value of approximately 19 cm/GW was measured at 1560 nm which taking into account the uncertainty in their data around 1550 nm is in good agreement with the value of β reported in this thesis.

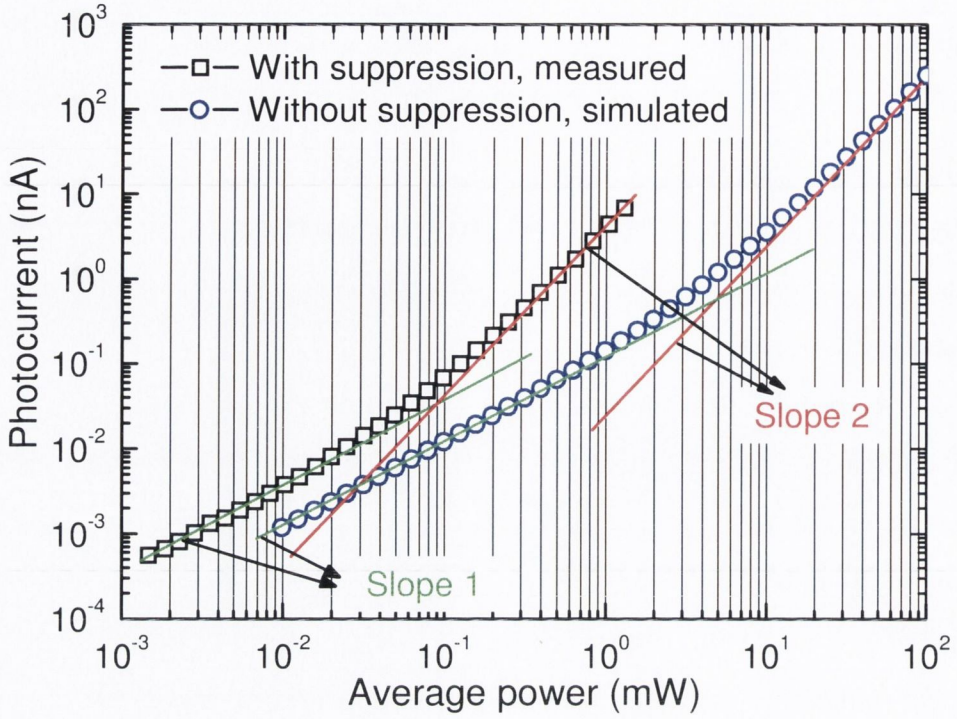

Fig. 4.4 Measured and simulated dependence of generated photocurrent on incident CW power for a TPAM (with suppression case) and a GaAs layer (without suppression case). The curve without SPA suppression was simulated for an absorbing region identical to the active region in the cavity but without the surrounding DBR's. The slopes of 1 and 2 correspond (on a log-log graph) to SPA and TPA dominated absorption regimes.

From the measured SPA current, α for this TPAM is estimated to be 0.93×10^{-4} cm^{-1}, which is a very low value. Even with this low value for α without relative suppression of the SPA, the SPA photocurrent would exceed the TPA photocurrent for the incident CW optical powers below 5 mW, see Fig. 4.4. In Fig 4.4 the simulated data is based on a non-cavity detector which has the same absorption length as the microcavity under test. If the influence of the acceptance angle on the microcavity could somehow be mitigated and so allowing the enhancement of the focused beam to be equal to the enhancement for the non-focused beam, then the TPA signal would exceed the SPA signal for CW incident optical powers greater than 38 μW.

4.4 Spot size measurement

The output signal from the lens, used throughout this thesis, has been profiled and found to have a Gaussian beam profile. The profiling was carried out by using a beam blocker which has a circular aperture, the diameter of which can be varied. Using this variable aperture it was also possible to find the diameter of the focused beam waist produced by the lens.

A focused Gaussian beam can be described as [73]

$$E(x,y,z) = E_0 \frac{\omega_0}{\omega(z)} exp\left(\frac{-r^2}{\omega(z)^2}\right) \tag{4.8}$$

where z is the axis orientated along the propagation direction of the beam. ω_0 is the beam radius at the focus position ($z = 0$) where the beam radius is taken to be the distance from the centre of the beam at which the amplitude drops to 1/e of its value on the axis at position z, see Fig. 4.5. $\omega(z)$ is beam radius at z (which is normally referred to as the beam spot size). Both x and y are two axes orthogonal to z, $r = \sqrt{x^2 + y^2}$. E_0 is the amplitude of the field of the Gaussian beam at the position where x, y and z are equal to 0. The radii ω_0 and $\omega(z)$ can be expressed in terms of each other according to

$$\omega^2(z) = \omega_0^2 \sqrt{1 + \frac{z^2}{z_0^2}} = \omega_0^2 \left[1 + \left(\frac{\lambda z}{\pi \omega_0^2}\right)\right] \tag{4.9}$$

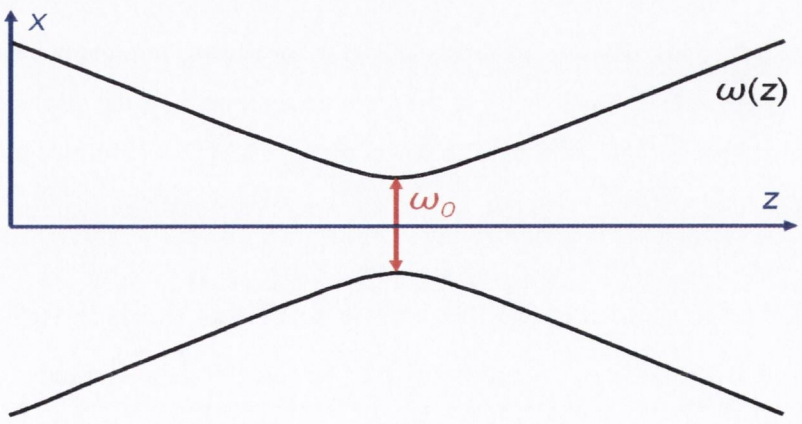

Fig. 4.5: Schematic of Gaussian pulse, ω_0 is the minimum beam waist, $z = 0$ corresponds to the position of ω_0 on the z-axis.

Using (4.8) the total power contained in a Gaussian beam (P_t) can be calculated

$$P_t = E(x,y,z)^2 = E_0^2 \frac{\omega_0^2}{\omega(z)^2} \int_0^\infty exp\left[-\frac{2r^2}{\omega(z)^2}\right] 2\pi r dr \tag{4.10}$$

Similarly the power transmitted through a circular aperture (P_a) can be calculated

$$P_a = \int_0^{\frac{D}{2}} E(x,y,z)^2 2\pi r dr = P_t\left(1 - \frac{D^2}{2\omega(z)^2}\right) \tag{4.11}$$

where the signal through the aperture has been centred on the aperture which has a diameter D. The relationship between P_t and P_a can be expressed as

$$y \equiv \sqrt{log\left(\frac{P_t}{P_t - P_a}\right)} = \frac{1}{\sqrt{2}\omega(z)} D \tag{4.12}$$

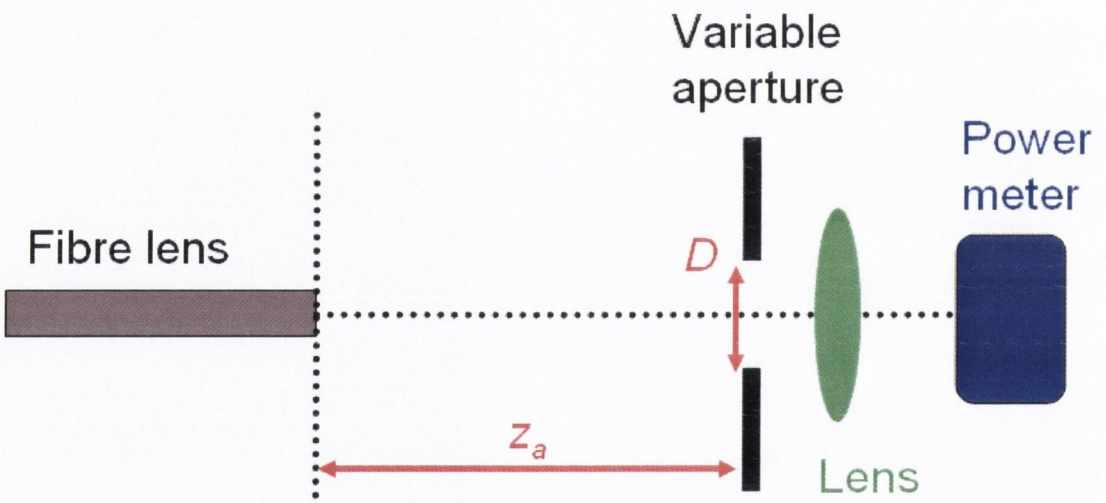

Fig. 4.6 Schematic diagram of setup used for measuring minimum beam waist of focused Gaussian signal, D is the diameter of the variable aperture, z_a is the distance between the output of the fiber lens and the aperture. The power meter is a Melles Griot integrating sphere (average power meter).

In order to measure ω_0 for the lens used in this thesis a variable aperture was placed in front of the fibre lens normal to the z axis a distance z_a from the output of the fibre lens, see Fig. 4.6. The signal used was a CW signal from a CW tunable laser (TLS) operating at 1550 nm. The variable aperture used had a

circular aperture which can be varied from approximately 2 mm to 40 mm while retaining its circular shape. The lens used after the aperture was used to focus the transmission onto the free space power meter (Melles Griot integration sphere, average power meter) which was used to measure the power transmitted through the aperture. Without the use of the lens it would have been possible for the beam to have diverged considerably by the time it had reached the power meter and for some of the beam to miss the power meter completely. The beam was aligned so as to pass through the centre of the aperture. The beam was centred in the aperture by making the aperture as small as possible and then moving the aperture along a plane orthogonal to the z axis until the power transmitted through the aperture was maximised.

The dependence of y on D is shown in Fig. 4.7 to be linear. From the slope of the linear fit in Fig 4.7 $\omega(z)$ can be found. It is now possible to find ω_0 using

$$\omega_0 = \frac{z\lambda}{\pi\omega(z)} \tag{4.12}$$

The ω_0 found for the lens used throughout this thesis 3.51 μm.

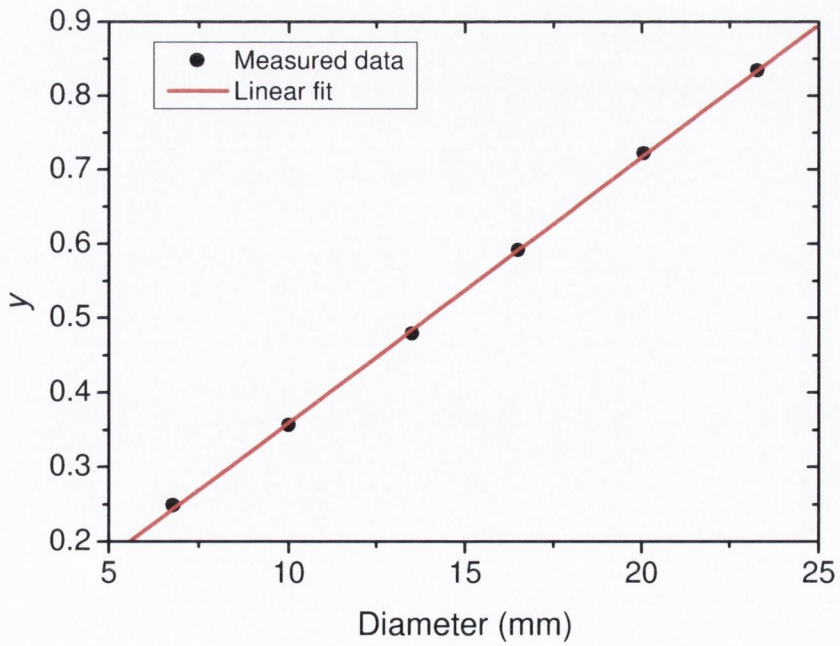

Fig. 4.7: Dependence of y on aperture diameter (D).

4.5 Conclusion

The most important feature of a TPAM is that of its enhancement of the optical field in order to enhance the level of TPA generated photocurrent for a particular input optical power incident on the detector. The TPAM is shown to not only enhance the level of TPA but also to relatively suppress the level of residual SPA [79]. This allows a TPA dominated signal to be accessed at much lower incident optical powers than would be possible with a similar GaAs absorbing region that is not sandwiched between two highly reflective DBR mirrors. The TPA coefficient is estimated to be approximately 15 cm/GW at 1560 nm in (001) GaAs. The residual SPA coefficient in the unintentionally doped GaAs active layer of the TPAM which is grown by metal-organic chemical vapour deposition is approximately 1.0×10^{-4} cm^{-1} (which is an extremely low value).

5. Influence of limited cavity acceptance angle

5.1 Influence of acceptance angle

In order for TPA based detection schemes to be considered for use it must be cost effective. In practice this means that the device will be required to work with as low an input optical power as is possible. Preferentially the detector will be able to operate at optical powers below -10 dBm. This is to allow the input to the detector to come from an optical tap of less than 10 % of network signal and then not need to be subsequently optically amplified before being incident on the detector. The first step towards this is the use of a microcavity, which due to the enhancement of the input optical field results in a lower threshold power being necessary to result in TPA dominated absorption. To further reduce the level of input optical power required the input beam must be focused onto the detector. This is because the level of TPA is inversely proportional to the incident spot area

$$I_{TPA} \propto \frac{P^2}{S} \tag{5.1}$$

where I_{TPA} = TPA generated photocurrent, P is the average incident power, S is the area of the incident signal. As the incident signal is focused so as to reduce the incident spot area this causes parts of the incident beam to have components with incident angles increasingly far away from that of the plane wave case (which is normal incidence). Some of the incident components will start to be off-resonance with the cavity due to its limited acceptance angle, see section 4.3. This results in both an asymmetric cavity spectral response and asymmetry in the peak response for the cavity for different focus positions [83]. The influence of the acceptance angle means there is a trade off between increasing TPA due to focusing the incident signal to smaller spot sizes vs. the decrease in TPA due the reduced acceptance of signals with smaller spots sizes by the cavity.

5.2 Theoretical analysis

We consider a continuous wave (CW) Gaussian beam normally incident on a microcavity detector. The enhancement of a short optical pulse in a microcavity has previously been analyzed in [74], see section 3.3. Shown in Fig. 5.1(a) is a Gaussian beam incident from air onto the microcavity detector surface, with the surface of the detector shown in Fig. 5.1(b). The electric field of the Gaussian beam can be expressed in air as

$$e_{in}(x,y,z)=\frac{e_0}{\sqrt{1+z^2\rho_0^{-2}}}exp(-\frac{x^2+y^2}{\omega^2(z)})exp(-i\beta\frac{x^2+y^2}{2H(z)}) \tag{5.2}$$

where $\rho_0 = \pi w_0^2 \lambda^{-1}$, $H(z) = z+\rho_0^2 z^{-1}$, and $\omega(z) = \omega_0(1+z^2\rho_0^{-2})^{1/2}$, e_0 is the input amplitude, $\beta = 2\pi/\lambda$ is the wavenumber in vacuum, λ is the incident wavelength, $z = 0$ is the position of the minimum beam waist (ω_0) where ω_0 is the $1/e$ beam radius at $z = 0$, $\omega(z)$ is the $1/e$ beam radius at z. The active layer is sandwiched between two highly reflective DBR's. The field in the active layer was calculated by decomposing the field at the detector surface ($z = z_s$ as shown in Fig. 5.1(a)) into plane waves with different lateral wavenumbers by calculating the Fourier transform

$$\tilde{e}_{in}(k_x,k_y,z_s)=\frac{1}{4\pi^2}\iint e_{in}(x,y,z_s)\exp(i(k_x x+k_y y))dxdy \tag{5.3}$$

where k_x and k_y are the wavenumbers in the x and y directions. Each plane wave component which is incident on the cavity produces a corresponding plane wave in the active layer. The resultant change in the plane wave is determined by the cavity transfer function

$$\Gamma(k_x,k_y,z)\equiv\frac{\tilde{e}_c(k_x,k_y,z)}{\tilde{e}_{in}(k_x,k_y,z_s)}$$
$$=\frac{\sqrt{T_0}\,exp(-i\phi_{t_0})(exp(-ik_z(z-z_a))+\sqrt{R_2}\,exp(-i(2k_z d+\phi_{r_2}))exp(ik_z(z-z_a)))}{1-\sqrt{R_1R_2}\,exp(-i(\phi_{r_1}+\phi_{r_2}+2k_z d))} \tag{5.4}$$

where $k_z = (n^2\beta^2-k_p^2)^{1/2}$, $k_p^2 = k_x^2+k_y^2$, n is refractive index of the active material, d is the active layer thickness, T_0 is the transmission of the front mirror for light incident from air, R_1 and R_2 are front and back mirror reflectivities for light

incident from inside the active region, ϕ_v (v represents r_1, r_2 and t_0) are the phase shifts associated with R_1, R_2 and T_0 respectively. The reflection and transmission phase shifts are assumed to be zero for normally incident plane waves at the mode wavelength, see section 2.1.5.

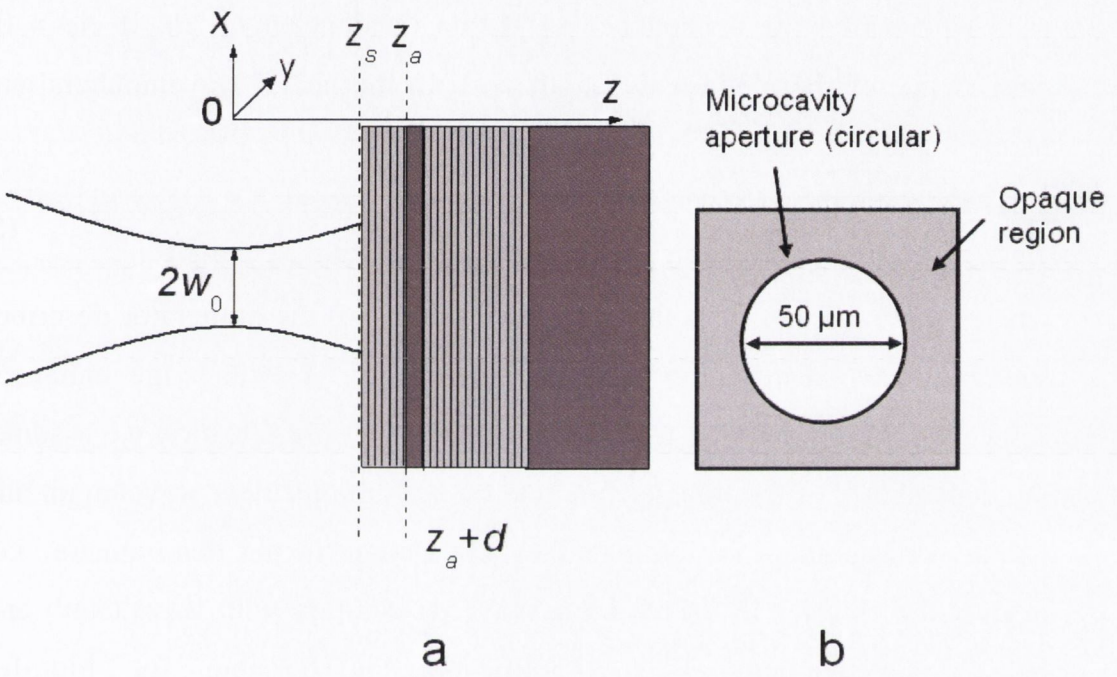

Fig. 5.1 (a) Schematic diagram of a Gaussian beam normally incident onto a microcavity detector. Fig. 5.1 (b) Schematic of input surface of the detector.

The start position (z_a) of the active layer is shown in Fig. 5.1(a). The round-trip phase shift $\phi = \phi_{r_1} + \phi_{r_2} + 2k_z d = 2m\pi$ determines the mode wavelength. If the lateral wavenumbers are equal to zero, i.e. for a normally incident plane wave, the mode wavelength is taken to be λ_0. Around this mode wavelength the change in the round-trip phase shift ϕ can be approximated using a first order Taylor expansion as

$$\Delta\phi \equiv \phi(\lambda_0 + \Delta\lambda, k_x, k_y) - \phi(\lambda_0, 0, 0) = -\frac{4\pi n_g l_\lambda \Delta\lambda}{\lambda_0^2} - \frac{l_\theta k_p^2}{n_0 \beta_0} \qquad (5.5)$$

where

$$l_\lambda = d - \frac{\lambda_0^2}{4\pi n_g}\frac{d\phi_{r_1}}{d\lambda} - \frac{\lambda_0^2}{4\pi n_g}\frac{d\phi_{r_2}}{d\lambda} \tag{5.6}$$

$$l_\theta = d + n\beta_0 \frac{d\phi_{r_1}}{d(k_p^2)} + n\beta_0 \frac{d\phi_{r_2}}{d(k_p^2)} \tag{5.7}$$

where n_0 is the refractive index at λ_0, $\beta_0 = 2\pi/\lambda_0$, l_λ is the effective length of the cavity used in describing the dependence of $\Delta\phi$ on λ, l_θ is the effective length used to describe the dependence of $\Delta\phi$ on incident angle (θ). If $\Delta\phi = 0$, the dependence of the mode wavelength on both the lateral wavenumbers and the incident angle is

$$\Delta\lambda = -\frac{l_\theta \lambda_0}{2n_0 n_g l_\lambda}\sin^2(\theta) \tag{5.8}$$

where $\sin(\theta) = k_p/\beta_0$, n_g is the group index. In (5.4) the numerator describes the standing wave distribution and the denominator describes the enhancement achieved by the reflection from the mirrors. As a simplification we assume that the dependence of the transfer function on both the incident wavelength and the lateral wavenumbers is dominated by the change in the denominator, i.e. we neglect the changes in the standing wave distribution with wavelength and the lateral wavenumbers. This simplification is possible for high-finesse microcavities as the deviation of incident wavelength is kept within a few nanometres of λ_0 and the incident angle is less than approximately 50 degrees off normal incidence. Angles of incidence within this range have a phase dependence on k_x^2 which is linear, see the inset of Fig. 2.4(a). The approximated transfer function is

$$\Gamma(k_x, k_y) \approx \frac{f(z)\exp(-i\Delta\phi_{\lambda,t_0})}{1 + \frac{R}{1-R}(1 - \exp(i\frac{4\pi n_g l_\lambda \Delta\lambda}{\lambda_0^2} + i\frac{l_\theta k_p^2}{n_0\beta_0}))}\exp(i\frac{l_{\theta,t_0}k_p^2}{n_0\beta_0}) \tag{5.9}$$

where

$$f(z) = \frac{\sqrt{T_0}(\exp(-in_0\beta_0(z - z_a)) + \sqrt{R_2}\exp(in_0\beta_0(z - z_a)))}{1 - R} \tag{5.10}$$

is the field inside the cavity for a normally incident plane wave at resonance; $\Delta\phi_{\lambda,t_0}$ is the dependence of the phase change in the top mirror on λ for light on its

initial transmission through the top mirror (t_0), $R = \sqrt{R_1 R_2}$, l_{θ,t_0} is the dependence of the effective length of the top mirror on θ for t_0. Both $\Delta\phi_{\lambda,t_0}$ and l_{θ,t_0} are calculated from ϕ_{t_0} as in (5.6) and (5.7). We then modify (5.9) using the spectral width and acceptance angle of the cavity as they are both easily measured experimentally. The spectral width ($\Delta\lambda_{FWHM}$, full-width at half maximum, FWHM) for normally incident plane waves can be expressed as

$$\Delta\lambda_{\text{FWHM}} = \frac{(1-R)}{\sqrt{R}} \frac{\lambda_0^2}{2\pi n_g l_\lambda} \tag{5.11}$$

The cavity acceptance angle with λ_0 incident can be expressed as

$$\Delta\theta_{\text{FWHM}} = 2\sin^{-1}\left(\sqrt{\frac{(1-R)}{\sqrt{R}} \frac{n_0\lambda_0}{2\pi l_\theta}}\right) = 2\sin^{-1}\left(\sqrt{\frac{\Delta\lambda_{\text{FWHM}}}{\lambda_0} \frac{n_0 n_g l_\lambda}{l_\theta}}\right) \tag{5.12}$$

If λ_0 is incident at an angle half that of the acceptance angle then the intensity inside the cavity will be half the normal incidence value. The cavity spectral width and the acceptance angle are related to each other through (5.8). We then re-write (5.9) as:

$$\Gamma(k_x,k_y) \approx \frac{f(z)\exp(-i\Delta\phi_{\lambda,t_0})}{1+\frac{R}{1-R}\left(1-\exp\left(i\frac{1-R}{\sqrt{R}}\frac{2\Delta\lambda}{\Delta\lambda_{FWHM}}+i\frac{1-R}{\sqrt{R}}\frac{4k_p^2}{\Delta\beta_{FWHM}^2}\right)\right)} \exp\left(i\frac{l_{\theta,t_0}k_p^2}{n_0\beta_0}\right) \tag{5.13}$$

where $\Delta\beta_{\text{FWHM}} = 2\beta_0\sin(\Delta\theta_{\text{FWHM}}/2)$. With the approximated transfer function we can calculate the field inside the cavity from the inverse Fourier transform. It can also be seen that $\exp(i\,l_{\theta,t_0}k_p^2/n_0\beta_0)\tilde{e}_{in}(kx,ky,z)$ is the Fourier transform of $e_{in}(x,y,z_s' \equiv z_s + 2l_{\theta,t_0}/n_0)$. So we can calculate the field inside the active layer as

$$e_c(x,y) \approx \iint \frac{e_{in}(x,y,z_s')\exp(-ik_x x - ik_y y)}{1+\frac{R}{1-R}\left(1-\exp\left(i\frac{1-R}{\sqrt{R}}\frac{2\Delta\lambda}{\Delta\lambda_{FWHM}}+i\frac{1-R}{\sqrt{R}}\frac{4k_p^2}{\Delta\beta_{FWHM}^2}\right)\right)} dk_x dk_y \tag{5.14}$$

where some unimportant phase factors have been omitted. The field dependence on z is $f(z)$ in (5.13) and is omitted in (5.14) for compactness. With (5.14) we can calculate the electric field in the active layer and the level of TPA. We use a relative value called the correction factor (C) to describe the cavity effect which

is defined as the ratio between the TPA generated in the active layer with and without the influence of the limited acceptance angle of the cavity

$$\zeta = \zeta_0 \frac{\iint |e_c(x,y)|^4 dxdy}{\iint |e_{in}(x,y,z_s')|^4 dxdy} \equiv \zeta_0 C \tag{5.15}$$

where

$$\zeta_0 = \frac{\int_{z_a}^{z_a+d} |f(z)|^4 dz}{d} = \frac{T_0^2(1+4R_2+R_2^2)}{(1-R)^4} \tag{5.16}$$

is the TPA enhancement for a normally incident plane wave at resonance. The factor C is a convolution of the dependence of cavity enhancement on both the incident wavelength and incident angle due to changes in $\Delta\phi$ as shown in (5.14).

5.3 Investigation of practical microcavity

The TPAM used for all simulations and experimental work in this chapter is a TPAM which is resonant at 1558.9 nm and has a 1-λ GaAs active region. The cavity has 14 p-doped $Ga_{0.88}Al_{0.12}As/Ga_{0.1}Al_{0.9}As$ top mirror pairs and 24 n-doped $Ga_{0.1}Al_{0.9}As$ /$Ga_{0.88}Al_{0.12}As$ bottom mirror pairs. The microcavity response is characterised using a signal provided by a continuous wave external cavity tunable laser. The signal is amplified by an Erbium-doped-fiber-amplifier (EDFA) which provides sufficient optical power to access the TPA dominant absorption regime. Due to TPA being an intrinsically polarisation sensitive process (see chapter 6), the signal is passed though a polarisation controller so that the signal onto the detector can be controlled. The polarisation is rotated so as to maximize the photocurrent at resonance and is then kept constant for these measurements. The polarisation controller consists of an input polarizer and a half- and quarter- wave plate. The lens arrangement has been profiled to ensure that the beam it produces has a Gaussian profile with a beam waist (ω_0) of 3.5 μm.

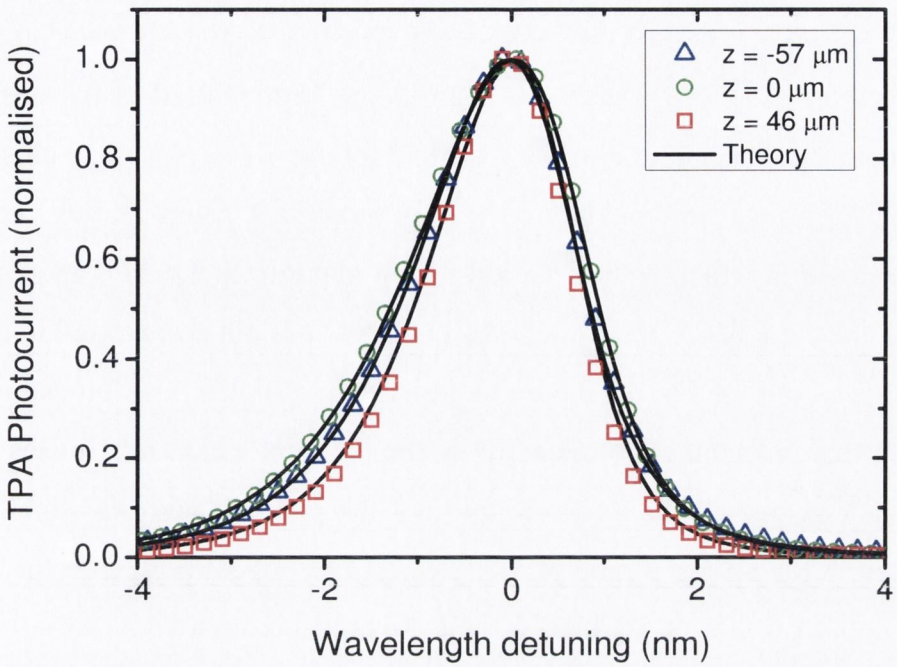

Fig. 5.2. Wavelength dependence of the microcavity for different focus positions with the microcavity operating in the TPA dominant regime with associated theoretical fits. The wavelength axis of each spectrum is centred on the maximum TPA response

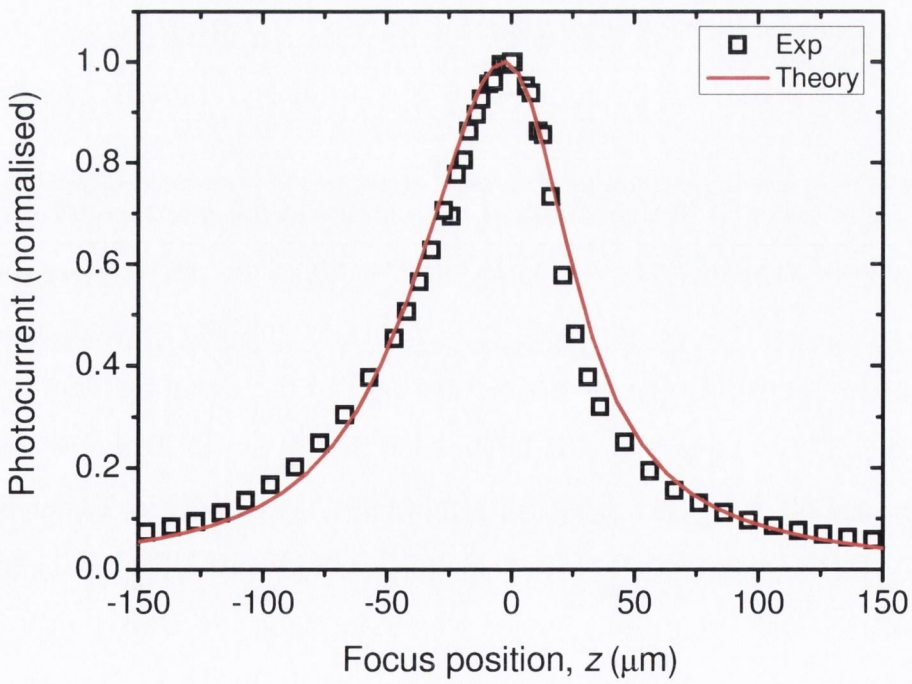

Fig. 5.3. Dependence of microcavity response on focus position. The focus position axis is centred on the maximum TPA response

The z-scan measurement was carried out by moving the microcavity along the propagation direction of the input beam. The microcavity is translated from z = -150 μm to z = 150 μm with the beam being kept centred in the aperture of the microcavity. The input signal for all measurements is placed as close to normal incidence on the microcavity as the measurement setup allows. The optimum focus position which is the position which maximizes the TPA response is set as being z = 0 μm. This optimum focus position does not correspond to the z = 0 μm position as outlined in the theory as experimentally this position can not be found (as all that is found experimentally is the position which maximises the level of the TPA generated photocurrent and not the position with the smallest spotsize centred in the spacer region of the cavity). The optical power on the microcavity was kept constant at 10 mW for the z-scan measurements. As z increases the microcavity is being moved away from the lens. At each z position the spectral dependence of the microcavity with TPA dominant is measured. This spectral response is asymmetric with the TPA response showing stronger wavelength dependence for wavelengths which are greater than resonance, see Fig. 5.2. The maximum photocurrent for each focus position is recorded, see Fig. 5.3. It is seen that the dependence of the peak TPA response on focus position is asymmetric about z = 0 μm. For positions with z > 0 μm less TPA is generated than for equivalent distances of z < 0 μm.

In order to fit the observed asymmetry in the microcavity response using the theory explained above, the spectral width of the microcavity response must be measured. To do this the microcavity is initially placed away from the optimum focus position so that the diameter of the signal incident in the detector is 65 μm. The input signal is larger than the 50 μm in diameter aperture of the microcavity; see Fig. 5.1(b). With this large spot size it is easier to access the SPA dominant regime. The wavelength is tuned across the cavity resonance for SPA and TPA dominant regimes which are achieved with 1 mW and 30 mW incident on the detector respectively as shown in Fig. 5.4. The spectral response of the SPA spectrum is fitted using a Lorentzian function. From this fitting the spectral width (SW) and the resonant wavelength (λ_0) are calculated as being

1.97 nm and 1558.9 nm respectively. The average reflectivity of the microcavity (R) is then calculated using $SW / FSR = R^{-1/2}(1-R)/\pi$. The spectra in Fig. 5.4 are normalised to the peak photocurrent and their wavelength-axis shifted to centre them at the origin. The remaining two unknowns necessary to fit the microcavity response are l_θ and l_λ. Both l_θ and l_λ are calculated theoretically for the device structure under test using the transverse matrix method, with values of 2.04 μm and 2.41 μm being calculated respectively.

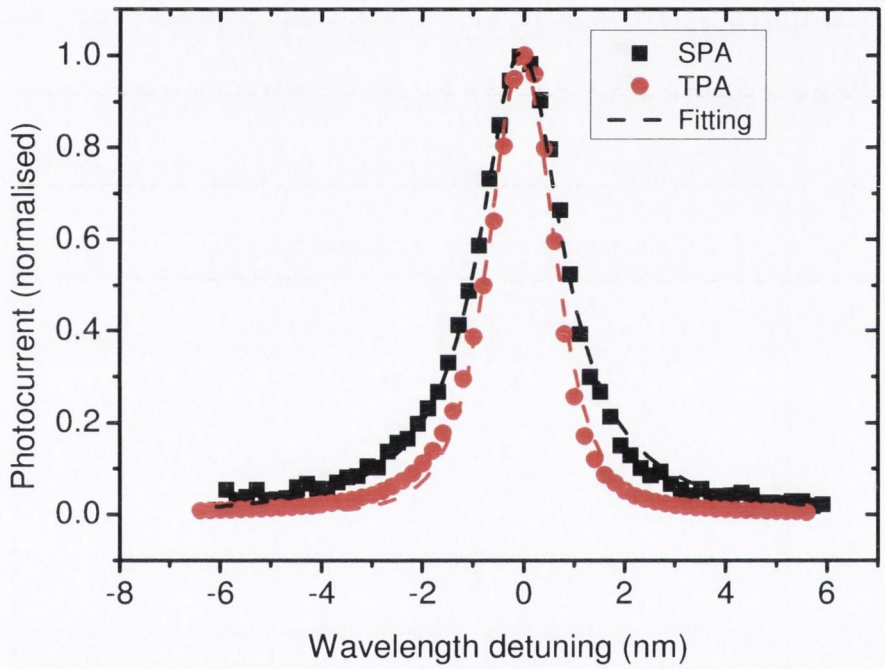

Fig. 5.4. Wavelength dependence of Microcavity for TPA and SPA dominant regimes with a 65 μm incident spot diameter. The dashed lines are the fittings of the SPA and TPA data with a Lorentzian and a Lorentzian squared function respectively.

When fitting the experimental data with the theory the device is found to be best fit by taking the incident signal on the microcavity as being 4.5 degrees off normal which is within the alignment accuracy of the experimental setup. The angle is included in the theory by adding the momentum resulting from the angle to k_x. The fitting of both the spectral response and the peak TPA response is shown in Fig. 5.2 and Fig. 5.3 respectively to fit the experimental data well. The

asymmetry in the spectral response in Fig. 5.2 is due the angular dependence of the cavity resonance wavelength (5.11). So as the input signal is focused some of the input signal is resonant at wavelengths less than λ_0. The asymmetry in the peak TPA response shown in Fig. 5.3 is due to the resultant effective spot size of the focused signal in the absorbing region of the microcavity. For $z < 0$ (converging beam) the effective spot size decreases after multiple roundtrips in the cavity where as for a diverging beam the effective spot size is larger than the incident spot size. From the theory it is found that the TPA response is not maximized when ω_0 is positioned so as to be in the centre of cavity. The signal is instead maximized approximately 17 μm from this position when the signal is converging.

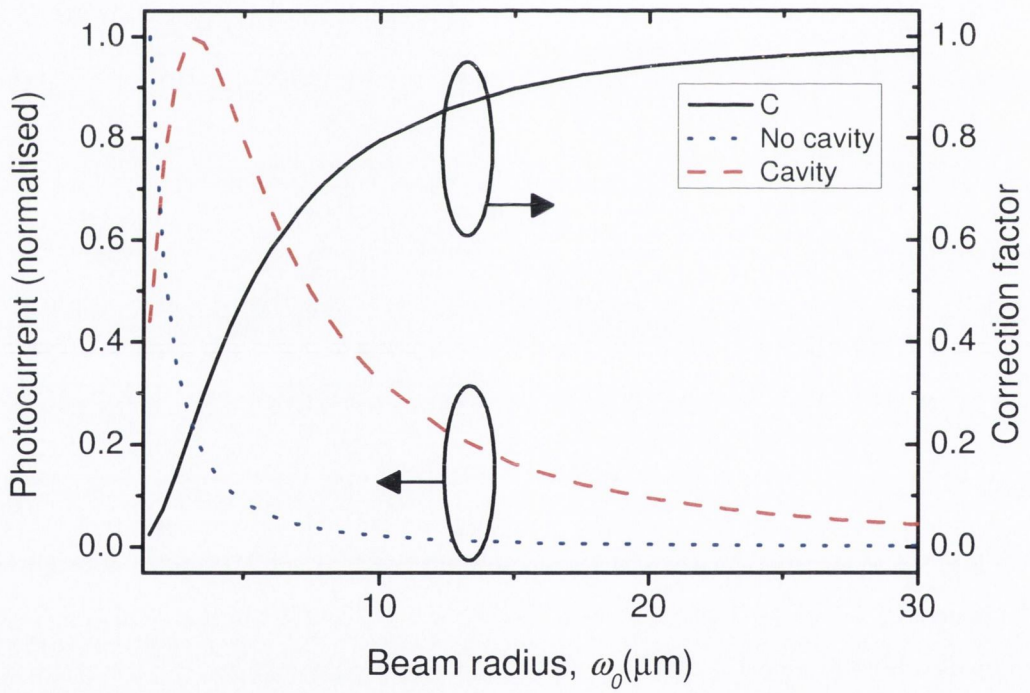

Fig. 5.5. Theoretical TPA response vs. ω_0 of incident beam for non cavity case (dotted line) with the photocurrent normalized to the signal generated by Gaussian signal with ω_0 = 1.5 μm, cavity case (solid line) is normalized to peak TPA response. Also shown (dashed line) is the response of the correction factor (C) vs. ω_0.

Using the theory a value of ω_0 for the input signal can be calculated which optimizes the TPA response in the microcavity. This is done by simulating the

dependence of (5.15) on ω_0. In the absence of a cavity, the TPA response ($\iint |e_{in}(x, y, z_s')|^4 dxdy$) is inversely proportional to the spot area, see Fig. 5.5. The TPA response in the cavity ($\iint |e_c(x, y)|^4 dxdy$) is more complicated. As the value of ω_0 is changed so too does the resonant wavelength of the cavity. So in the theoretical analysis for each value of ω_0 the wavelength is changed so as to optimise the TPA response. The peak TPA response for each value of ω_0 is recorded, see Fig. 5.5. We find that the spot size which maximizes the TPA response in the cavity is not the smallest possible spot size. The value of C is also shown vs. ω_0. Fig. 5.5 shows that the TPA response of the cavity increases with increasing spot size, as the input signal is more efficiently coupled to the resonant cavity mode until the optimum spot size is reached. The optimum ω_0 for this microcavity structure was calculated as being 3.5 μm. Once the incident spot size exceeds the optimum value the level of TPA generated in the structure decreases. This is due to the increasing spot size dominating the cavity TPA response. The value of C is shown to approach 1 as the incident spot size becomes larger and the incident beam becomes more like a plane wave.

5.4 Conclusion

Even with the enhancement provided by the TPAM it is still necessary to focus the input beam onto the TPAM in order to operate in the TPA dominated absorption regime at low optical input powers. A TPAM has a limited acceptance angle and so different angular components have different levels of enhancement in the cavity. For a TPAM detector, this results in an asymmetrical cavity spectral response and also an asymmetrical response to the focus position. The influence of the acceptance angle on the TPA response of the TPAM means that to optimize the level of TPA generated by a TPAM, the optimal spot size for the TPAM must be calculated. An optimized incident focused spot diameter of 7 μm has been calculated as being optimal so as to maximize the generated TPA photocurrent for the R = 0.965 TPAM under test. While measurements were only

carried out for a TPAM with $R = 0.965$, it is shown that the theory described can also be used to calculate the optimal incident focused spot size for cavities with different values of R. With increasing TPAM cavity lifetime the dependence on incident angle becomes increasingly important and as such the optimal incident spot size will increase.

6. Polarisation dependence

6.1 Introduction

In order to use these structures for TPA applications in which the polarisation of the input signal is subject to change, we must first fully understand the TPA polarisation dependence in these microcavities. The polarisation dependence of the TPA coefficient is dependant on the crystalline orientation of the material [23]. The polarisation dependence of TPA in (001) GaAs at 950 nm has been previously reported in [11]. As linear polarisation is rotated through 360 degrees, the TPA dependence is periodic, with a period of 90 degrees, and a variation of approximately 27 % in the TPA coefficient (β).

For the TPAM the polarisation dependence of the TPA process and the microcavity itself are convoluted. It is therefore necessary to characterise the additional contribution of the cavity effect to the intrinsic polarisation dependence of bulk GaAs.

6.2 Polarisation dependence of TPA in semiconductor microcavity

TPA measurements were carried out using a $Ga_{0.1}Al_{0.9}As/Ga_{0.88}Al_{0.12}As$ TPAM which is resonant at λ = 1561 nm with a 1 λ thick GaAs absorption region [80]. The cavity has 7 p-doped top mirror pairs and 24 n-doped bottom mirror pairs. The input optical signal is provided by an external cavity tunable diode laser which is modulated at 300 kHz with a duty cycle of 50 %, see Fig 6.1. The signal is amplified by an erbium-doped-fiber-amplifier (EDFA) so as to allow the TPA-dominated regime to be accessed. The signal is also passed through a variable optical attenuator (VOA) and a polarisation controller (PA). The polarisation

controller consists of an input polarizer and a half- and quarter-wave plate. Using the polarisation controller, the specific polarisation of the input signal onto the detector can be set. The detector is placed away from the in-focus position so as to reduce the effect of angular components of the input beam, which can result in asymmetry of the measured TPA spectrum due to the angular dependence of the TPAM response.

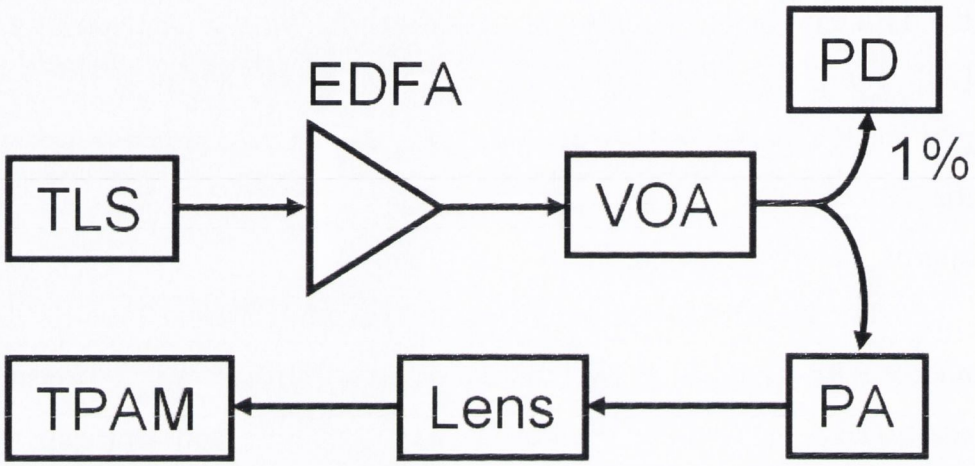

Fig. 6.1 Schematic of device setup. PD is photodiode used to monitor average power, VOA is a variable optical attenuator, and PA is a polarisation controller. After lens signal is in free space.

The TPAM also has some residual single-photon absorption (SPA) which is also enhanced by the TPAM [79], see chapter 4. The SPA polarisation dependence of the TPAM was investigated first. The polarisation state of the input signal was rotated through various states of linear polarisation around the Poincaré sphere; see Fig. 6.2. These scans were carried out with the average power held constant at 0.15 mW, which is low enough for the detected photocurrent to be dominated by SPA, as shown in Fig. 6.7(inset), which shows the TPAM photocurrent as a function of incident power near the cavity resonance. The graph is plotted with a log-log scale on which a slope of two and slope of one correspond to the TPA and SPA dominant regimes, respectively. For bulk GaAs, SPA is independent of the linear polarisation state but as can be seen in Fig. 6.2 there is a clear polarisation dependence of the detected photocurrent in

a TPAM. The deviation from the bulk material response can be explained by the birefringence of the cavity with the minimum and maximum of the SPA polarisation dependence corresponding to the two eigenmodes of the cavity.

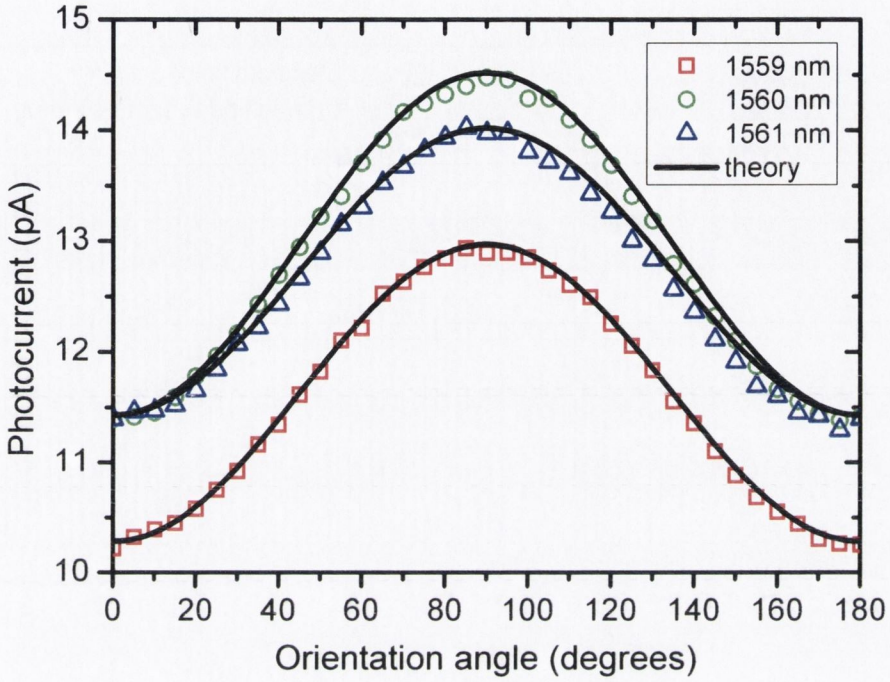

Fig. 6.2. SPA generated photocurrent vs. orientation of linear state of polarisation (θ) of the incident optical signal. The polarisation scan is carried out at a low average power (0.15 mW) in the SPA dominant regime at three different wavelengths around the cavity resonance.

Similar birefringence has previously been seen in vertical-cavity-surface-emitting-lasers (VCSEL's) which are similar in structure to these microcavities [84]. The birefringence is due to the electro-optic effect, which, as a third-order tensor, is not necessarily isotropic in cubic materials and so can lead to birefringence. The linear electro-optic effect (the quadratic effect does not affect this birefringence) arises mainly from the stark shift of atomic core states [84]. For the TPAM investigated here the change in refractive index associated with the electro-optic effect can be described by [84]:

$$\Delta\left(\frac{1}{n^2}\right) \approx \pm r_{41} E_{dc}(z) \tag{6.1}$$

where n is the refractive index, r_{41} is the linear electro-optic coefficient and $E_{dc}(z)$ is the internal field as a function of the position in the cavity (z), with z = 0 μm

corresponding to the air interface of the cavity. In order to calculate the influence of the electro-optic effect in a TPAM the field at each of the material interfaces ($E_{dc}(z)$) must be calculated. The calculated field which has been simulated using Simwindows [85] is shown in Fig. 6.3.

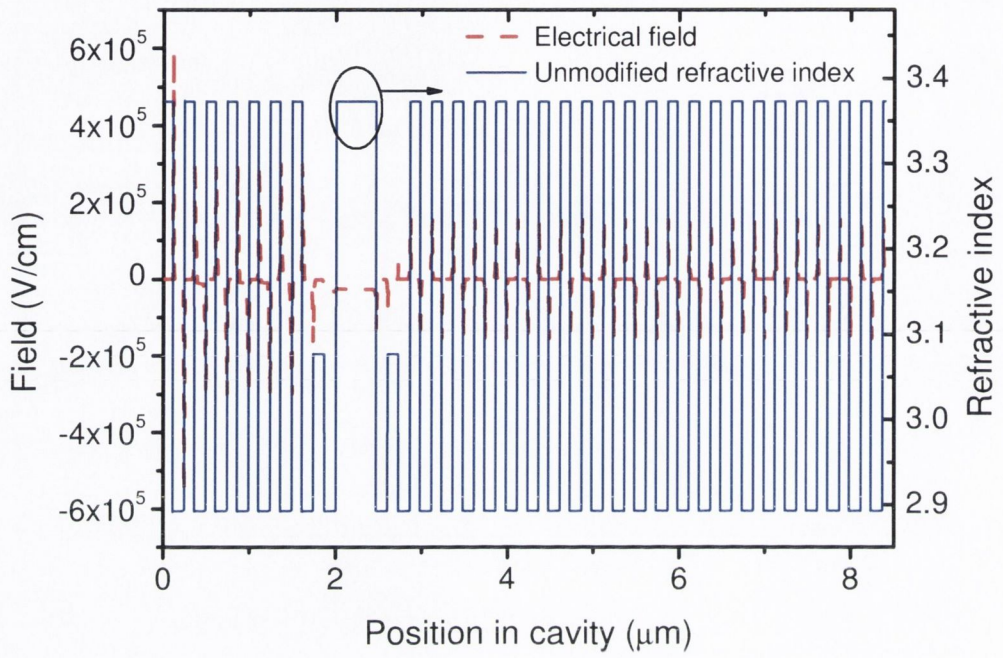

Fig. 6.3 (a) Refractive index distribution of a TPAM. Also shown is the field associated with each of the mirror interfaces, with the field having been calculated using Simwindows. 0 μm corresponds to the air/TPAM interface.

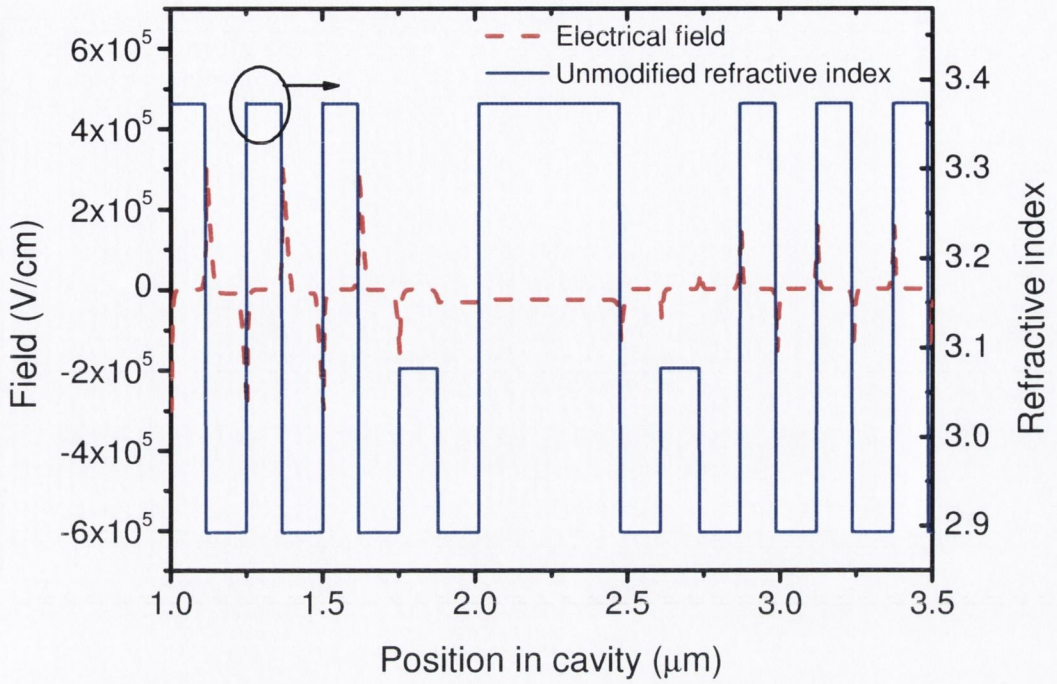

Fig. 6.3 (b) Refractive index distribution of the top 2 μm of a TPAM. Also shown is the field associated with each of the mirror interfaces, with the field having been calculated using Simwindows. 0 μm corresponds to the air/TPAM interface.

The calculated field allows for the calculation of the change in refractive index throughout the TPAM using (6.1), see Fig. 6.4. The cavity optical field associated with each of the TE modes of the cavity is convoluted with the modified refractive index, see Fig. 6.5. The resultant splitting between the resonant modes of the two TE modes can then be calculated using the transverse matrix method as in chapter 3, see Fig. 6.6. From Fig. 6.6 which compares both the experimental and theoretical spectral dependence of the cavity (for the SPA dominated absorption regime) it can be seen that the theoretical splitting between the resonant wavelengths of the two TE modes is in good agreement with the experimental observed response (approximately 0.15 nm).

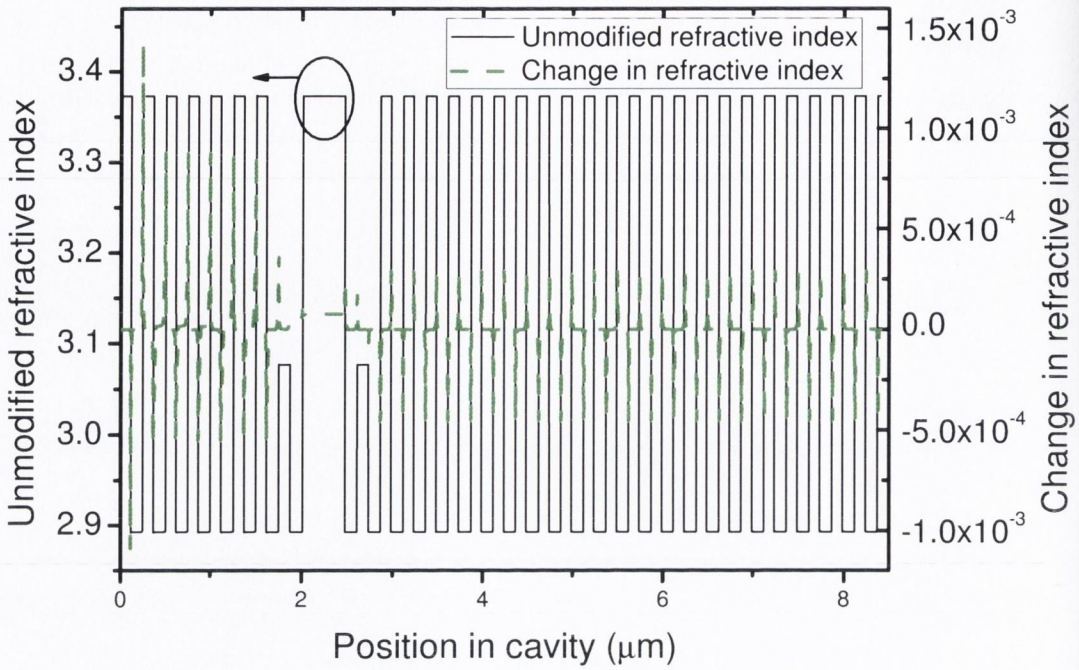

Fig. 6.4 (a) Refractive index distribution of a TPAM. Also shown is the change in refractive index caused by the electro-optic effect which is associated with electrical field at each of the mirror interfaces. 0 μm corresponds to the air/TPAM interface.

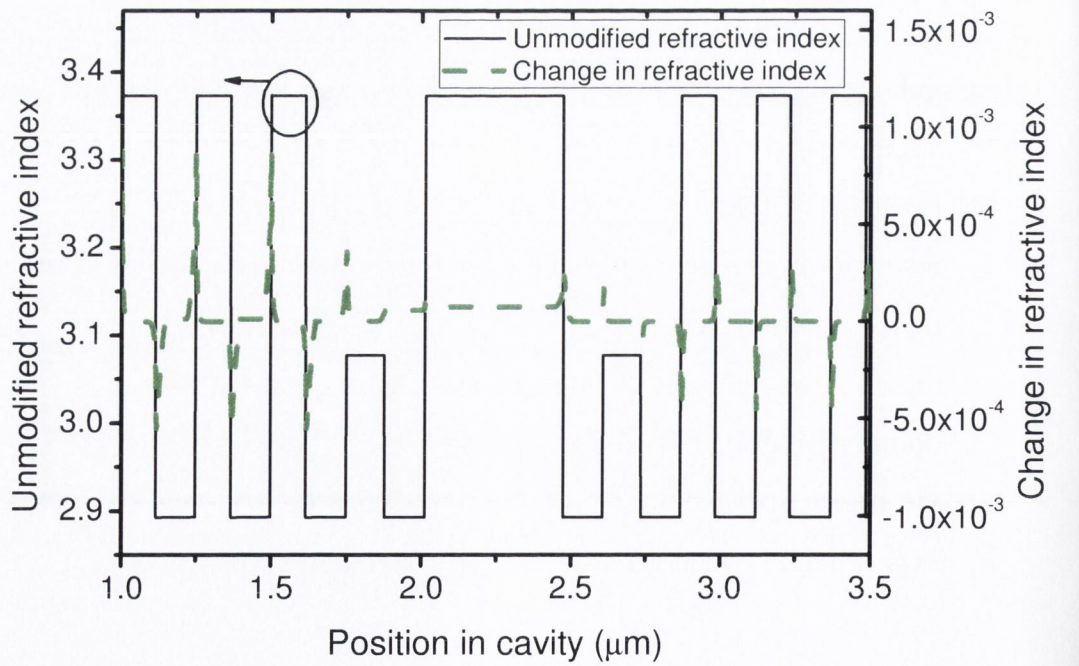

Fig. 6.4 (b) Refractive index distribution of a section of a TPAM. Also shown is the change in refractive index caused by the electro-optic effect which is associated with electrical field at each of the mirror interfaces. 0 μm corresponds to the air/TPAM interface.

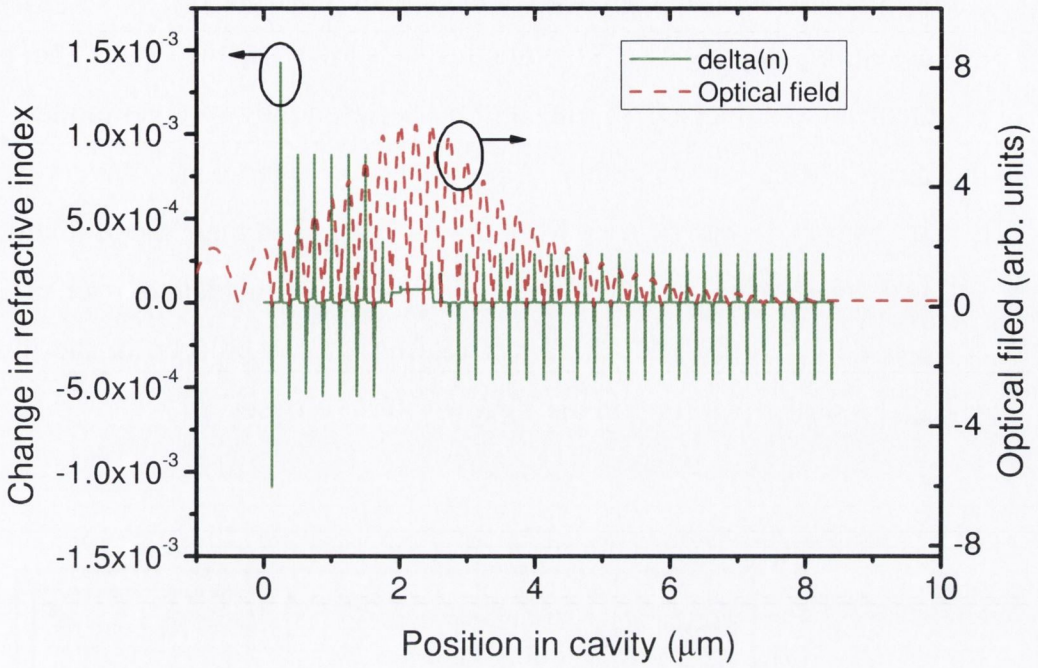

Fig. 6.5 Shown is the refractive index change (delta(n)) and the optical field in a TPAM. 0 μm corresponds to the air/TPAM interface.

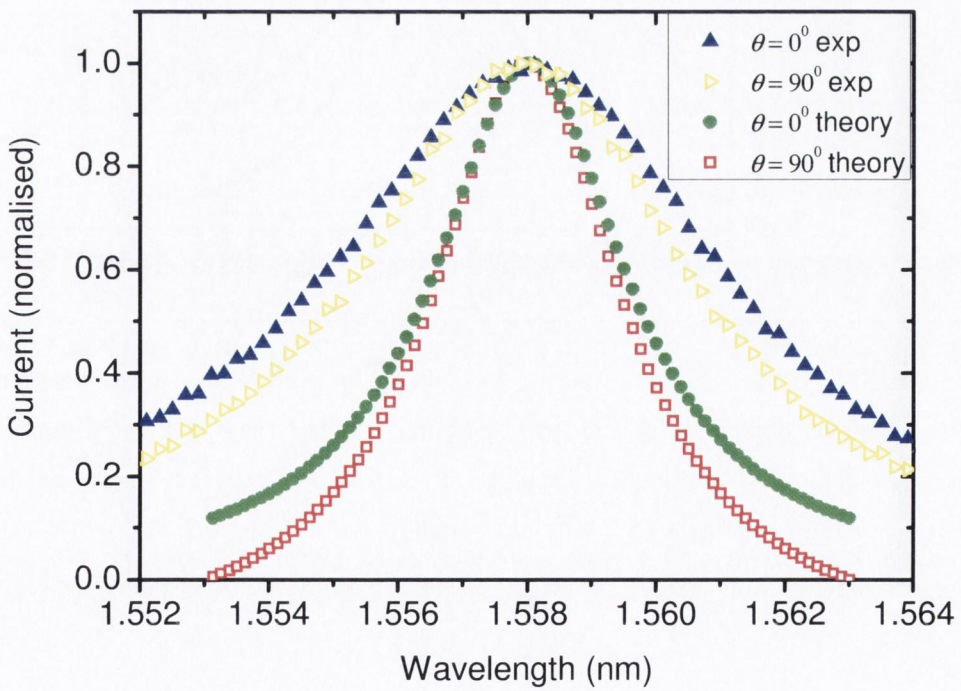

Fig. 6.6 Theoretical and experimental spectral dependence of a TPAM (SPA dominated regime). The theoretical spectral dependence includes the influence of the electro-optic effect.

The wavelength dependence of the photocurrent for states of polarisation corresponding to the two eigenmodes is shown in Fig. 6.7. The peak SPA photocurrent exhibits a 0.15 nm splitting between the two eigenmodes, indicating the birefringence of the cavity. Also these two eigenmodes have very different quality factors, as can be seen from the differences in their spectral widths. These spectral scans were repeated with a high average incident power of 37.8 mW, corresponding to the TPA-dominant regime, as can be seen in the inset of Fig. 6.7, and a similar splitting in the TPA response is observed.

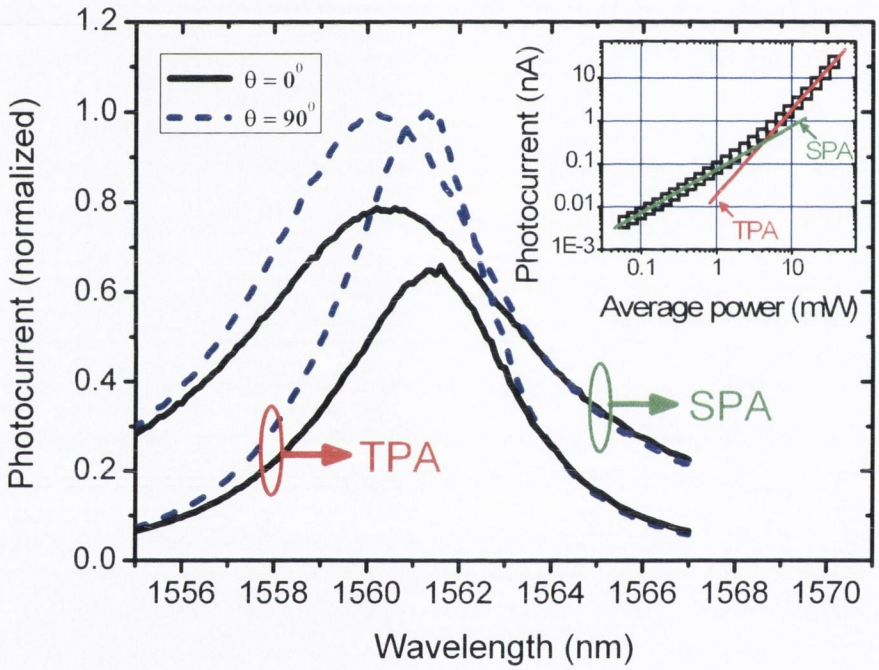

Fig. 6.7 Normalized photocurrent vs. wavelength for both high average power incidence and low average power incidence, corresponding to the TPA and SPA dominant regimes, respectively. The wavelength scans were carried out for the linear polarisation states corresponding to the peak ($\theta = 90^0$) and trough ($\theta = 0^0$) of Fig. 6.2. Fig. 6.7(inset) Photocurrent vs. incident optical power curve carried out near the resonant wavelength.

Further investigation of the polarisation dependence of the TPAM photocurrent was performed by scanning the state of polarisation from circular through linear and back to circular in the SPA dominant regime, as shown in Fig. 6.8. SPA in bulk GaAs has no phase dependence, so the change in SPA

photocurrent in Fig. 6.8 can again be explained by the birefringence of the cavity. As the ellipticity of the signal changes, so too does the ratio of the power coupled into each eigenmode. The cavity enhances the two eigenmodes differently, resulting in the polarisation dependence seen in Fig. 6.8.

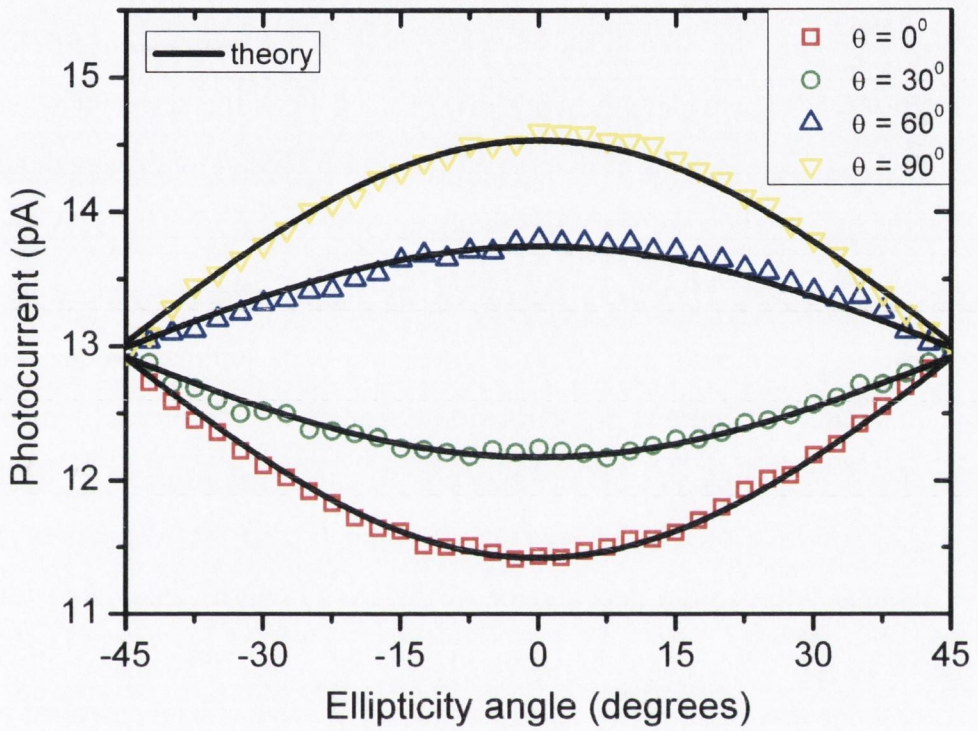

Fig. 6.8 Dependence of the SPA photocurrent on the state of polarisation as it is rotated from circular to linear to circular along a 4 different longitudinal lines of the Poincaré sphere, where θ is the orientation angle.

The SPA polarisation dependence of the TPAM can be found by calculating the enhancement by the microcavity for the two cavity eigenmodes. Once the enhancement of each of the modes is known, the SPA response of the microcavity for all input polarisation states can be calculated. In order to characterise the enhancement of the cavity, the overall reflectivity of the cavity (R) for each of the eigenmodes must be determined. This can be calculated from the SPA photocurrent spectra in Fig. 6.7. By fitting the spectral response of each of the two eigenmodes with a Lorentzian function, the bandwidth (BW) and the resonant wavelength (λ_0) can be extracted. The free spectral range (FSR) is given

by $FSR=\lambda_0/2D$ where D is the effective optical cavity length and is calculated to be 1.97 μm [79]. R can now be calculated using $BW / FSR = R^{-1/2}(1-R)/\pi$ and the cavity field enhancement factor is given by

$$e_{x,y} = \frac{C_{x,y}}{1 - R\,exp\left[-i\frac{2\pi\Delta\lambda_{x,y}}{FSR}\right]} \tag{6.2}$$

which describes the field in the cavity relative to the input electric field. $\Delta\lambda$ is the deviation of the wavelength being investigated from the resonant wavelength of the cavity which is used to determine the phase change with wavelength, which changes by 2π when the wavelength changes by one FSR. The SPA photocurrent generated in the TPAM is described by $I_{SPA} = \alpha A|e|^2$, where α is the SPA absorption coefficient and A is a constant; both parameters are polarisation independent. The unknown polarisation dependent parameter $C_{x,y}$ in (6.2) can be calculated by fitting the SPA photocurrent calculated from (6.2) to the data in Fig. 6.2 for each of the two eigenmodes (θ = 0° and 90° respectively). The full SPA linear polarisation dependence of the cavity can be calculated for all states of linear polarisation by calculating the amount of power coupled to each of the eigenmodes and then taking into account the relative enhancement of each mode using (6.2), as can be seen in Fig. 6.2. Similarly, it is possible to fit the polarisation dependence of the cavity for all elliptical polarisations, as there is no phase dependence for SPA in bulk GaAs. Once the power coupled into each eigenmode has been calculated, using (6.2) the SPA generated photocurrent for that polarisation state can be calculated, the results of which are shown in Fig. 6.8. As seen from both Fig. 6.2 and Fig. 6.8, the theoretical results based on the above analysis agree very well with the experimental data, which suggests that the previous assumption that both eigenmodes are linearly polarised, and their orientations are related to the peak and trough of Fig. 6.2, is valid.

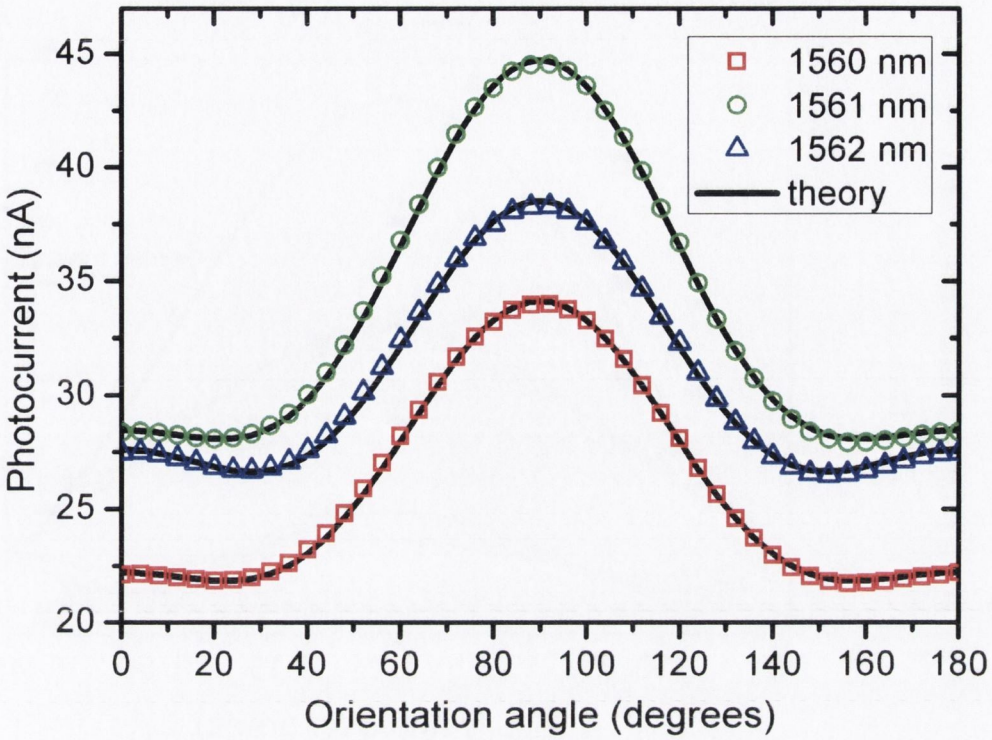

Fig. 6.9 TPA photocurrent vs. orientation of the linear state of polarisation of the incident optical signal, recorded for three wavelengths around the cavity resonance.

The case for TPA is slightly more complicated, as the TPA process in GaAs is polarisation dependant. From Fig. 6.7 it can be seen that the resonance wavelength of the cavity is not the same for the TPA dominated regime as it is in the SPA dominated regime. This can be explained by the thermal tuning of the cavity because of the large difference in incident power levels used for the TPA and SPA dominant regimes. The dependence of TPA photocurrent on the orientation of the linear polarisation state was recorded at three wavelengths around the cavity resonance, with constant average power incident, as shown in Fig. 6.9. The local maxima ($\theta = 0^{\circ}$ and 90°) correspond to the eigenmodes of the cavity. The difference between the amplitudes of the peaks is due to the birefringence of the cavity. In the absence of birefringence, the amplitude of both peaks would be the same for all wavelengths. The TPA photocurrent was also recorded as the input polarisation state was scanned from circular to linear to circular along four different longitudinal axes of the Poincaré sphere, see Fig. 6.10.

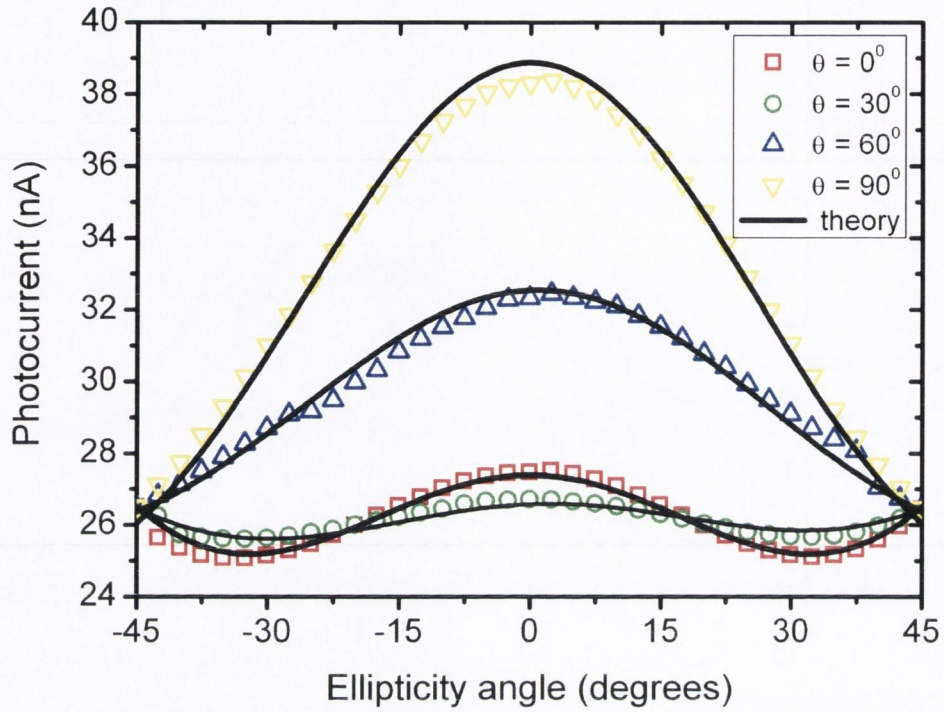

Fig. 6.10. Dependence of the TPA photocurrent on the state of polarisation as it is rotated from circular to linear to circular along 4 different longitudinal lines of the Poincaré sphere, where θ is the orientation angle.

In order to model the polarisation dependence of the TPA photocurrent, we must first calculate the intrinsic polarisation dependence of TPA in GaAs and then couple it with the polarisation dependence of the cavity as described for the SPA case. The TPA-generated photocurrent in the TPAM can be described by $I_{TPA} = \beta B|e|^4$, where β is the TPA absorption coefficient in the TPAM and B is a polarisation independent constant. The polarisation dependence of TPA in GaAs has previously been described in [23] as being dependant on three parameters. These are χ''_{xxxx}, σ the anisotropy parameter, where

$$\sigma = \frac{\left[\chi''_{xxxx} - \chi''_{xxyy} - 2\chi''_{xyxy}\right]}{\chi''_{xxxx}} \tag{6.3}$$

and δ, which is the incremental TPA dichroism parameter, where

$$\delta = \frac{\left[\chi''_{xxxx} + \chi''_{xxyy} - 2\chi''_{xyxy}\right]}{2\chi''_{xxxx}} \tag{6.4}$$

χ is a 4th rank tensor that describes the 3rd order susceptibility of GaAs, where χ''_{xxxx} is used as a shorthand representation of $Im\chi''_{xxxx}(-\omega,\omega,\omega)$, etc. The value for σ in GaAs has been previously reported as –0.76 at 950 nm [11]. The value at 1550 nm has not previously been measured experimentally, but the theoretical value is approximately half the value reported at 950 nm value [23]. Similarly, a value for δ has not previously been measured at 1550 nm. Both σ and δ at 1550 nm are determined later in this thesis. β has been expressed in [11] as

$$\beta = \frac{\omega}{2n^2c^2\varepsilon_0} Im\left\{\chi''_{xxyy}\left|\hat{p}.\hat{p}\right|^2 + 2\chi''_{xyyx} + \sigma\chi''_{xxxx}\right\} \tag{6.5}$$

Using the following relations which come from (6.4) and (6.5) β can be expressed in terms of σ and δ

$$\chi''_{xxyy} = \chi''_{xxxx}\left(\delta - \frac{\sigma}{2}\right) \tag{6.6}$$

$$2\chi''_{xyxy} = \chi''_{xxxx}\left(1 - \frac{\sigma}{2} - \delta\right) \tag{6.7}$$

which allows (6.5) to be expressed as

$$\beta = \frac{\omega}{2n^2c^2\varepsilon_0}\chi''_{xxxx}\left(\left(\frac{2-\sigma-2\delta}{2}\right) + \left(\frac{2\delta-\sigma}{2}\right)\left|\tilde{\zeta}.\tilde{\zeta}\right|^2 + \sigma\sum_i\left|\zeta_i^4\right|\right) \tag{6.8}$$

where $\tilde{\zeta}$ is the Jones matrix describing the polarisation state with reference to the principal crystallographic axes of GaAs. In order to calculate the TPA photocurrent, the electric field inside the cavity has to be found first using (6.2), by decomposing the incident polarisation into two orthogonal directions based on the two eigenmodes of the cavity. This is similar to the process used for the SPA photocurrent calculation. The Jones matrix describing the polarisation state inside the cavity was then determined. To facilitate the use of (6.3) in calculating the TPA photocurrent, the Jones matrix is rotated by 45 degrees, as the eigenmodes are oriented along [110] and $[1\bar{1}0]$ directions.

As in the SPA case, the polarisation dependent parameter $C_{x,y}$ was found experimentally by fitting the calculated photocurrent to the linear polarisation states corresponding to the two eigenmodes; see Fig. 6.9. The calculated $C_{x,y}$ values are then used in calculations for all the other states of polarisation. The

mode splitting of the two eigenmodes is very small when compared with the spectral width, as shown in Fig. 6.7. This shows that once the incident polarisation is linear, the polarisation inside the cavity does not significantly gain ellipticity, but its orientation will be changed slightly due to the enhancement difference of each of the eigenmodes. As the polarisation remains linear, the change in the TPA coefficient will be dependent only on σ which can be determined by fitting the measured linear polarisation dependence in Fig. 6.9. We find that an excellent fit can be achieved for a value of σ equal to –0.33, as seen in Fig. 6.9.

As the incident polarisation gains ellipticity, the electric field inside the cavity can still be found through processes similar to those introduced above; however the polarisation inside the cavity will be elliptical as well. For elliptical polarisations, the TPA coefficient will also depend on δ. With the value for σ obtained above and using δ as a fitting parameter, we can repeat the above fitting process on the measured curves in Fig. 6.10. As can be seen in Fig. 6.10, an excellent fit can be achieved for a value of δ equal to 0.068. The values calculated here of σ = -0.33 and δ = 0.068 are similar to the theoretical values predicted by [23], which are σ = -0.487 and δ = 0.076 and were obtained using low temperature parameters of GaAs. Although the values reported in this thesis were obtained at room temperature, they are still in good agreement with the values reported in [23].

6.3 Conclusion

A full characterisation of the polarisation dependence of TPA and SPA in a GaAs-based TPAM photodetector has been carried out. The two eigenmodes of the cavity have been identified and shown to be separated by 0.15 nm, due to birefringence in the cavity. The effect of this birefringence on the field enhancement associated with the two cavity eigenmodes has been shown to

explain the deviation of the polarisation dependence of the TPAM structure from that of bulk GaAs. In order to characterise the polarisation dependence of the TPA photocurrent in the TPAM detector, experimental values for σ and δ of -0.33 and 0.068, respectively, at a wavelength of 1550 nm in GaAs have been estimated at room temperature and shown to fit the experimental data very well.

7. Two-photon absorption generated by amplified spontaneous emission

7.1 Amplified spontaneous emission

Due to the dependence of TPA on signal variance it has attracted attention for use in carrying out optical performance monitoring (OPM) of optical networks [19, 66, 68, 86, 87]. A network impairment that is suitable for monitoring using TPA is optical signal to noise ratio (OSNR) [19, 68]. OSNR is generally defined as the ratio of the total average signal power to the amplified spontaneous emission (ASE) power in a specified optical bandwidth around the signal channel with 0.1 nm generally used as the defined bandwidth (this is the definition used in this work) [19]. OSNR is a useful indication of network health as OSNR is strongly related to the bit error rate (BER) of a signal transmitted through an optical network [54]. A number of previous OSNR monitoring schemes have focused on measuring the level of ASE present between adjacent signal channels which are outside the signal band [88, 89]. The problems with such out of band OSNR measurements are two fold. Firstly as channel spacing is reduced (i.e. to 50 GHz in a DWDM 10 Gbs^{-1} system) the spacing between channels may not be large enough to make an accurate measurement [90]. The second and more important reason is that the ASE outside the signal band may not be (and very likely is not going to be) an accurate indication of the level of ASE that is combined with the signal in the signal band. This difference is due to the effect of the series of filters present in a network through which the signal has been transmitted [90]. It is possible using TPA based detection to carry out an in-band OSNR measurement without the need for clock recovery or any other costly high speed electronics. In order to carry out TPA based OSNR monitoring the level of TPA generated by ASE must be understood. In this work we look at ASE generated by an optical amplifier. It has previously been reported that ASE generates the same amount of TPA as that produced by a CW signal [19]. This

statement is investigated here and found to be incorrect. It is shown here that the level of TPA produced by a polarised band-limited ASE (BL-ASE) signal is the same as that produced by a CW signal which is modulated so as to have an generalised duty cycle (d_{gen}) of 0.5 [67]. d_{gen} is defined as

$$d_{gen} = \frac{\overline{p(t)}^2}{\overline{p(t)^2}} \tag{7.1}$$

where $\overline{p(t)}^2$ is the average signal power squared and $\overline{p(t)^2}$ is the square of the signal power at time t averaged over t.

7.2 TPA generated by a modulated signal

The level of TPA generated by a modulated signal is well understood [19]. For simplicity in this analysis only one polarisation is considered so that the polarisation response of the detector as discussed in chapter 6 need not be taken into account. The field of an optical modulated signal after being passed through an amplifier with gain G can be described as

$$s(t) = \sqrt{(2G\,p(t))}\cos(\omega_0 t) \tag{7.2}$$

where ω_0 is the carrier angular frequency. The TPA photocurrent generated by $s(t)$ can be expressed as

$$i_{signal} = C\,Im(\chi^{(3)})\overline{|s(t)|^4} = \frac{C\,Im(\chi^{(3)})G^2\overline{p(t)}^2}{d_{gen}} \tag{7.3}$$

where $C = el/(4n^2c^2\varepsilon_0\hbar S)$, l is the absorption length, S is the spot area, n is the refractive index, ε_0 is the permittivity of free space, $\hbar$ is the reduced Planck's constant, e is the change of an electron.

7.3 SPA based detection of amplified spontaneous emission

Previously the level of SPA generated by an ASE signal has been investigated in [91]. In [91] the ASE optical field is described as

$$n(t) = \sum_{k=-M}^{M} \sqrt{2N_0\delta_v}\cos((\omega_0 + 2\pi k\delta\nu)t + \Phi_k) \tag{7.4}$$

where Φ_k is a random phase for each ASE component. P_{sp} is the spontaneous emission power in a given optical bandwidth (B_0) $P_{sp} = N_{sp}(G-1)h\nu B_0$, N_{sp} is the spontaneous emission factor of the amplifier, G is taken to be a constant in the bandwidth B_0, M is the number of frequency steps over which the summation is carried out $M = B_0/2\delta\nu$, $N_0 = N_{sp}(G-1)h\nu$. The ASE field can be combined with the signal field in order to calculate the field that is output from the an amplifier $E(t)$

$$E(t) = \sqrt{2Gp(t)}\cos(\omega_0 t) + \sum_{k=-M}^{M} \sqrt{2N_0\delta\nu}\cos((\omega_0 + 2\pi k\delta\nu)t + \Phi_k) \tag{7.5}$$

with the SPA generated photocurrent $i_{SPA}(t)$ resulting from the amplifier output being

$$i(t) \propto \overline{E^2(t)}\frac{e}{h\nu} \tag{7.6}$$

with the bar referring to a time average over the optical frequencies B_0. $\overline{E^2(t)}$ can be expressed as

$$\overline{E^2(t)} = \overline{s^2(t)} + \overline{2s(t)n(t)} + \overline{n^2(t)} \tag{7.7}$$

where the 3 terms on the right hand side are the SPA signal, signal noise beat and noise terms respectively. It is important to note the influence of the averaging on the result. When calculating the product of two variables $A(t)$ and $B(t)$ that the product of $\overline{A \cdot B}$ does not necessarily equal $\overline{A} \cdot \overline{B}$. The analysis of the noise term is the most complicated due to the effect of averaging over the random phase term, to simplify this $\overline{n^2(t)}$ can be re-expressed as

$$\overline{n^2(t)} = 2N_0\delta\nu \sum_{k=-M}^{M} cos(\beta_k) \sum_{j=-M}^{M} cos(\beta_j) \tag{7.8}$$

where $\beta_{j,k} = (\omega_0 + 2\pi k\delta\nu)t + \Phi_{j,k}$, therefore (7.8) can be expanded as

$$\overline{n^2(t)} = 2N_0\delta\nu \sum_{k=-M}^{M} \sum_{j=-M}^{M} \left(\frac{1}{2} cos(\beta_k - \beta_j) + \frac{1}{2} cos(\beta_k + \beta_j) \right) \tag{7.9}$$

The $cos(\beta_k + \beta_j)$ term in (7.9) can be expressed as

$$\sum_{k=-M}^{M} \sum_{j=-M}^{M} (cos(\beta_k + \beta_j)) = \sum_{k=-M}^{M} \sum_{j=-M}^{M} cos((k+j)2\pi\delta\nu t + \Phi_k + \Phi_j) \tag{7.10}$$

In order for (7.10) to have a non-zero dc term then the terms inside the brackets of the cosine term must be 0. If the terms inside the brackets of the cosine term ends up being non-zero (i.e. of the form $cos(2\omega_0)$ or $cos(\Phi_p)$ where Φ_p represents a random phase term) then their summation does not have a dc component and as such make no contribution to $\overline{E^2(t)}$. (7.10) has a time average of 0 as the summations over the random phase terms $(\Phi_k + \Phi_j)$ do not cancel each other out. This leaves the terms of the form $cos(\beta_k - \beta_j)$ that have a non-zero dc component. This allows $\overline{n^2(t)}$ to be expressed as

$$\overline{n^2(t)} = N_0\delta\nu \sum_{k=-M}^{M} \sum_{j=-M}^{M} cos((k-j)2\pi\delta\nu t + \Phi_k - \Phi_j) \tag{7.11}$$

with the dc component of (7.11) corresponding to when $k = j$, for which there are $2M$ terms

$$\overline{n^2(t)} = N_0\delta\nu 2M \tag{7.12}$$

$\overline{E^2(t)}$ can be expressed using (7.11) as

$$\overline{E^2(t)} = Gp(t) + N_0\delta\nu 2M = Gp(t) + P_{sp} \tag{7.13}$$

as there is no dc component for $s(t)n(t)$ due to the addition of the random phases cancelling out. (7.13) shows that the dc component of the SPA generated photocurrent is simply an addition of the signal and noise power, which means that the dc SPA term gives no information about the beating of the signal and noise $(s(t)n(t))$ as this term averaged out to zero.

7.4 TPA based detection of amplified spontaneous emission

The TPA generated photocurrent can be expressed as

$$i_{TPA}(t) \propto \overline{E^4(t)} \frac{e}{2h\nu} \tag{7.14}$$

which can be expressed in the same way as (7.7)

$$\overline{E^4(t)} = \overline{s^4(t)} + \overline{4s^3(t)n(t)} + \overline{6s^2(t)n^2(t)} + \overline{4s(t)n^3(t)} + \overline{n^4(t)} \tag{7.15}$$

The time averaging of (7.15) is carried out in the same way as done for the SPA case described above. This allows $\overline{4s^3(t)n(t)}$ and $\overline{4s(t)n^3(t)}$ to be neglected as they have no dc component. This allows (7.15) to be changed to

$$\overline{E^4(t)} = \overline{s^4(t)} + \overline{6s^2(t)n^2(t)} + \overline{n^4(t)} \tag{7.16}$$

with the three terms on the right hand side representing the signal term, signal-noise beat term and the noise term respectively. The terms are all calculated in the same way as for the SPA case.

The noise term $\overline{n^4(t)}$ can be expressed as

$$\overline{n^4(t)} = (2N_0\delta\nu)^2 \sum_{k=-M}^{M} cos(\beta_k) \sum_{l=-M}^{M} cos(\beta_l) \sum_{m=-M}^{M} cos(\beta_m) \sum_{n=-M}^{M} cos(\beta_n) \tag{7.17}$$

where $\beta_{k,l,m,n} = (\omega_0 + 2\pi k\delta\nu)t + \Phi_{k,l,m,n}$. As with (7.11) there are two conditions which must be satisfied in order for the terms from (7.17) to contribute to $\overline{n^4(t)}$. Firstly $k+l+m+n$ must equal zero otherwise the resultant term will be of the form $cos(2\omega_0)$ and as mentioned above $cos(2\omega_0)$ has no dc component. Secondly the random phase terms must cancel with each other or else the resulting term is of the form $cos(\Phi_p)$ with $cos(\Phi_p)$ as mentioned above also not having a dc component. (7.17) can be expressed as

$$\begin{aligned}\overline{n^4(t)} = (2N_0\delta\nu)^2 \frac{1}{8} \sum_{k=-M}^{M} \sum_{l=-M}^{M} \sum_{m=-M}^{M} \sum_{n=-M}^{M} [1cos(\beta_k + \beta_l + \beta_m + \beta_n) + \\ 4cos(\beta_k + \beta_l + \beta_m - \beta_n) + 3cos(\beta_k - \beta_l - \beta_m + \beta_n)]\end{aligned} \tag{7.18}$$

where similar cosine terms have been grouped together. (7.18) has 3 terms which contribute to the dc component of the generated signal

$$\overline{n^4(t)} = (2N_0\delta\nu)^2 \frac{1}{8} \sum_{k=-M}^{M} \sum_{l=-M}^{M} \sum_{m=-M}^{M} \sum_{n=-M}^{M} [cos(\beta_k + \beta_l - \beta_m - \beta_n) + cos(\beta_k - \beta_l + \beta_m - \beta_n) + cos(\beta_k - \beta_l - \beta_m + \beta_n)] \tag{7.19}$$

For each of the 3 cosine terms there are $2 \cdot (2M)^2$ terms which are non-zero. This comes from $cos(\beta_k + \beta_l - \beta_m - \beta_n)$ having a non-zero dc component for two cases (i) $k = m$ and $l = n$ and (ii) $k = n$ and $l = m$ with both case (i) and (ii) each have $2M$ non-zero terms

$$cos(\beta_k + \beta_l - \beta_m - \beta_n) = \sum_{k,m=-M}^{M} \sum_{l,n=-M}^{M} cos(\beta_k + \beta_l - \beta_m - \beta_n) + \sum_{k,n=-M}^{M} \sum_{l,m=-M}^{M} cos(\beta_k + \beta_l - \beta_m - \beta_n) = (2M)^2 + (2M)^2 \tag{7.20}$$

(7.20) can be subbed back into (7.19) to get

$$\overline{n^4(t)} = \frac{1}{8}(2N_0\delta\nu)^2 \cdot 3 \cdot 2 \cdot (2M)^2 = 3(N_0B_0)^2 = 3P_{sp}^2 \tag{7.21}$$

The signal noise beat term $(6s^2(t)n^2(t))$ can be expressed using (7.2, 7.8) as

$$6s^2(t)n^2(t) = 6G\overline{p(t)}^2(N_0\delta\nu) \sum_{k=-M}^{M} \sum_{j=-M}^{M} [cos(\beta_k - \beta_j) + cos(\beta_k + \beta_j)] \cdot [1 + cos(2\omega_0)] \tag{7.22}$$

which once the terms that do not contribute to the dc term have been removed can be re-expressed as

$$6\overline{s^2(t)}\,\overline{n^2(t)} = 6G\overline{p(t)}^2(N_0\delta\nu) \sum_{k=-M}^{M} \sum_{j=-M}^{M} [cos(\beta_k - \beta_j)] \tag{7.23}$$

with there being $2M$ terms which contribute to the dc term which allows it to be expressed as

$$6s^2(t)n^2(t) = 6G\overline{p(t)}^2(N_0\delta\nu)2M = G\overline{p(t)}^2P_{sp} \tag{7.24}$$

The signal term $\overline{s^4(t)}$ can be expressed using (7.2) as

$$\overline{s^4(t)} = 4G^2\overline{p^2(t)}cos^4(\omega_0 t) = \frac{3}{2}G^2\overline{p^2(t)} \tag{7.25}$$

$\overline{E^4(t)}$ can now be expressed using (7.21, 7.24, 7.25) as

$$\overline{E^4(t)} = \frac{3}{2}\left(\overline{p(t)^2} + 4\overline{p(t)}P_{sp} + 2P_{sp}^2\right) \tag{7.26}$$

where G has been set to 1 for simplicity. The important thing to note about (7.26) is that if there are two signals one of which is a CW signal and the other is an

ASE signal and both of them are independently incident on a TPA detector then the ASE signal will generate twice as much photocurrent as the CW signal. (7.26) can be expressed for a modulated signal as

$$\overline{E^4(t)} = \frac{3}{2}\left(\frac{\overline{p(t)}^2}{d_{gen}} + 4\overline{p(t)}P_{sp} + 2P_{sp}^2 \right) \tag{7.27}$$

Equations (7.26, 7.27) are investigated experimentally in section (7.5).

7.5 Experimental investigation of OSNR

The experimental setup used to investigate the dependence of TPA generated photocurrent on OSNR consisted of a signal and a noise source, see Fig. 7.1 [67]. The signal source is a tuneable laser source (TLS) which is provided by a tuneable external cavity laser (ECL). The TSL can output either a CW signal or a square wave on-off modulated signal at 200 kHz. The modulated output signal from the TLS has a value of d_{gen} = 0.5. The noise source consists of an EDFA with no input optical signal which results in the EDFA outputting a broadband ASE signal with a spectral shape similar to that of the gain spectrum of the EDFA generating it. This broadband ASE signal is then directed through a bandpass filter (BPF) with a 1 nm broad pass band. This BPF results in a smaller wavelength region needing to be amplified by the subsequent EDFA which allows higher optical powers to be accessible in the wavelength region which is being investigated (B_0). The signal and noise are combined using a 50:50 beam splitter before being passed through a manual polarisation controller and being input into a polarisation controller (PA). The manual polarisation controller consists of 3 fibre loops on 3 paddles which use stress induced birefringence to act as 3 fractional wave plates. Using the manual polarisation controller the polarisation of the signal is adjusted so as to maximise the transmission of the signal through the input polariser of the PA. As the ASE signal is un-polarised, the ASE power transmitted through the PA is unaffected by the manual

polarisation controller. The PA consists of an input polarizer and a half- and quarter-wave plate. This PA polarizes the noise and also ensures that it the BL-ASE is incident on the detectors with the same polarisation as the signal. The output of the PA is amplified using an EDFA to ensure the optical power is high enough to allow the TPA dominated absorption regime to be accessed when the signal is incident on the TPAM. The output of the second EDFA is passed through a second BPF. The purpose of this second filter is to ensure that very little optical power is present outside the 1 nm bandwidth for which the measurement is being carried out. The output of the second BPF is passed to a 50:50 beam splitter with 50 % of the power going to the TPAM and the other 50 % going to the optical spectrum analyser (OSA). The OSA is used both as an average power meter and as an OSNR monitor. The photocurrent generated in the TPAM is recorded using a picoammeter. A small amount of the ASE which is generated by the second EDFA (which is de-polarised) passes through the second BPF but the amount is negligible in comparison with the level of polarised ASE. The input signal onto the TPAM is focused using a fibre lens which results in an incident spot diameter ($1/e^2$) of 7 μm, see section 4.4.

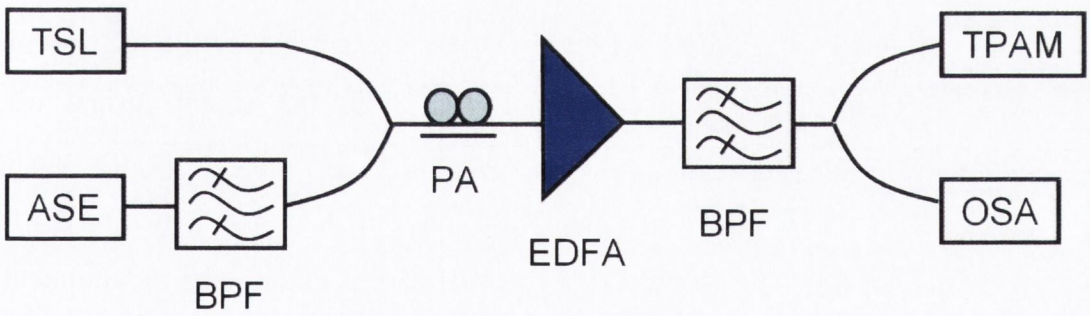

Fig. 7.1 Schematic of experimental setup. ASE is EDFA with no input signal, BPF is 1nm bandpass filter, PA is polarisation controller, OSA is optical spectrum analyser, and TPAM is TPA microcavity photodetector

The OSNR is varied by changing both the TLS and the ASE output power individually. This measurement did not allow the total average power p_{total} on the TPAM to be kept constant. The effect on the generated i_{TPA} due to the change in

power is removed by taking the ratio of $\overline{i_{TPA}(t)}/\overline{p(t)}^2$. The set OSNR value during the measurements is calculated using the OSA.

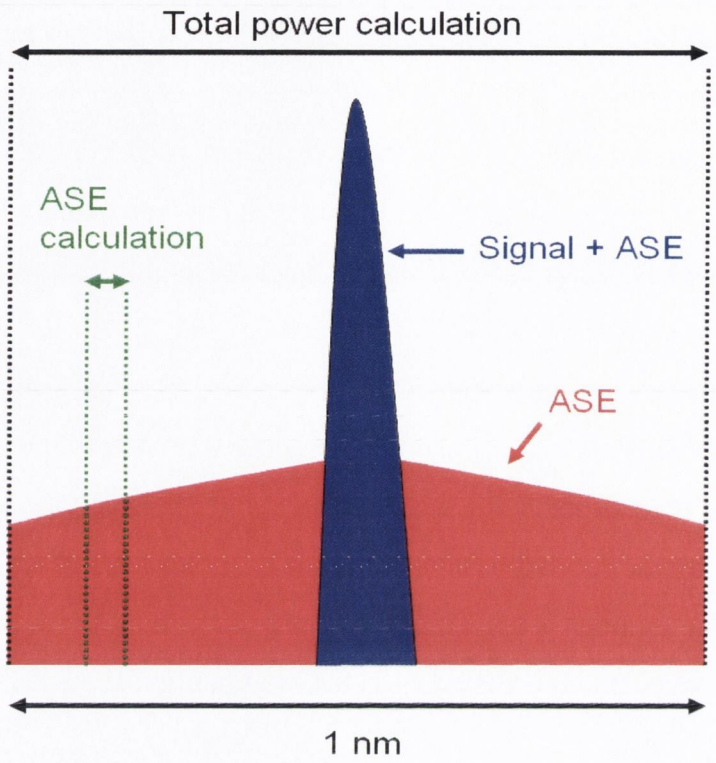

Fig. 7.2 Schematic of how OSNR calculation is made using OSA

In order to calculate the level of ASE present during the measurement the ASE spectral shape is first characterised with the signal turned off. This characterisation of the ASE spectral response is carried out because the spectral shape of the ASE in a 1 nm bandwidth once it is transmitted through the two BPF's is not flat. The spectral shape of the ASE is taken to be independent of the input signal power. Once the ASE spectral shape is recorded only one measurement of the ASE power in a narrow (0.06 nm) bandwidth was needed in order to calculate the total ASE power present (P_{sp}) with the measurement being carried out > 0.2 nm offset from the signal channel, see Fig. 7.2. The total power onto the TPAM was then calculated by setting the OSA to have a large bandwidth (i.e. 5 nm) and then measuring the power centred on the signal channel. From these two values the OSNR was calculated using (7.27). The

polarisation of the signal onto the detectors is rotated using PA so as to maximise the level of $\overline{i_{TPA}(t)}$ and is then kept constant through out each of the measurements, see chapter 6.

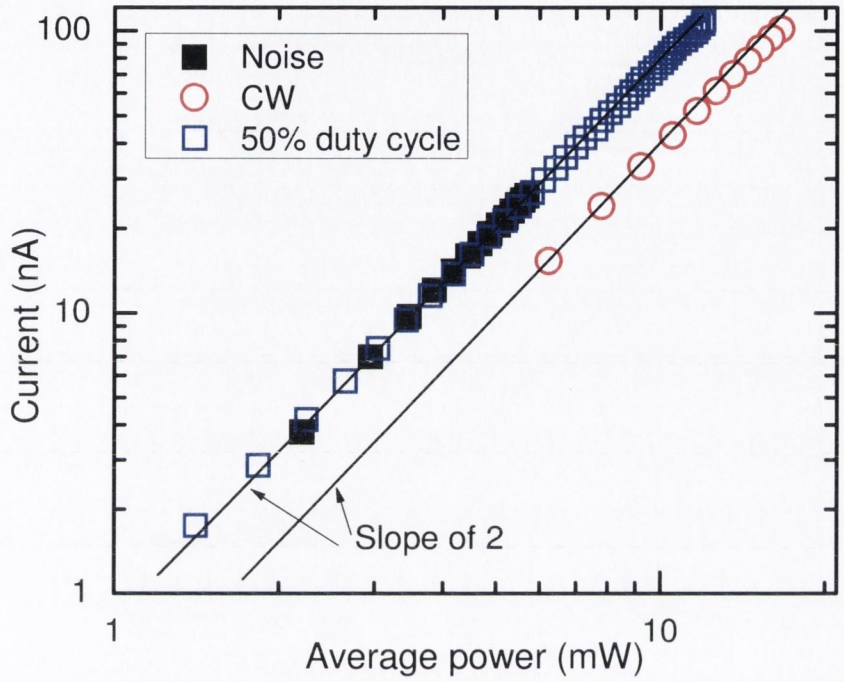

Fig. 7.3 Measured photocurrent against average power for BL-ASE, CW and 50 % on-off modulated signals (NRZ-OOK)

In order to experimentally verify equation (7.27) two separate measurements are carried out. The first measurement is to find the level of TPA generated by both the signal term and by the noise term independently. To do this power curves are carried out for the three different source types which are CW signal, modulated signal (d_{gen} = 0.5) and filtered ASE. Each signal type is independently input onto the detector and their power varied, see Fig. 7.3. Fig 7.3 is fit using a linear function and each of the fitted curves are found to have a slope of 2 on a log-log graph which indicates that each of the signals is operating in a TPA dominated regime. For the same amount of average power it also shows that the ASE signal generates twice as much TPA as is generated by the CW signal for the same average power, as predicted by (7.26). The overlapping of the ASE curve and the modulated signal (d_{gen} = 0.5) shows that ASE generates the

same level of TPA as a modulated signal (d_{gen} = 0.5) for the same average power, as is shown in (7.27). So in terms of TPA generated photocurrent both the filtered ASE and modulated signal (d_{gen} = 0.5) are equivalent.

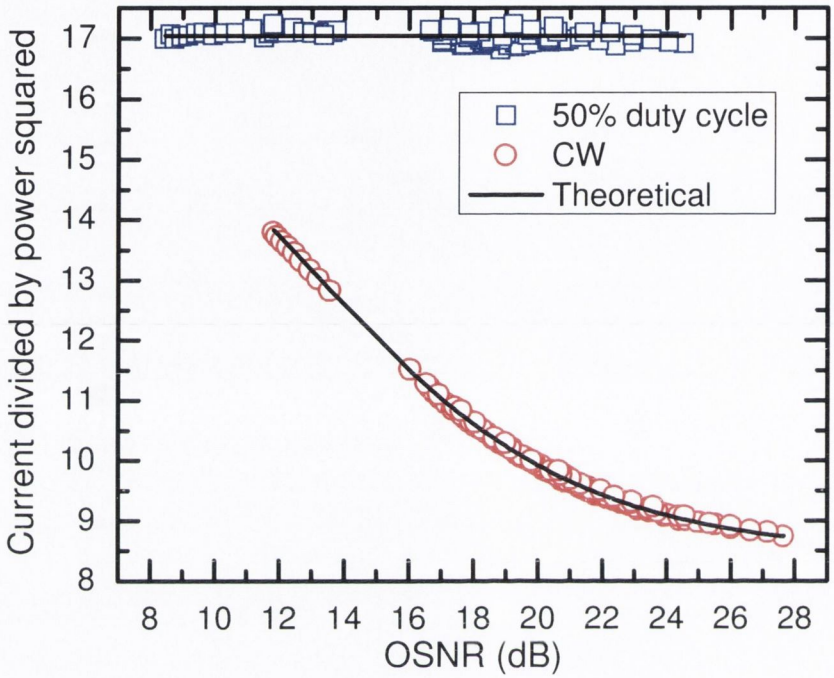

Fig. 7.4 Normalised TPA photocurrent dependence on OSNR for a modulated signal (d_{gen} = 0.5) and a CW signal

The second measurement measured the TPA dependence on OSNR both for a CW signal and a modulated signal (d_{gen} = 0.5), see Fig. 7.4. The measurement of OSNR dependence is used to verify the calculation of the beat term in (7.27). It can be seen for the modulated signal (squares in Fig. 7.4) that the generated level of i_{TPA} shows no dependence on the level of OSNR. This independence from the OSNR level is due to the modulated signal producing the same amount of TPA as a filtered ASE signal once both have the same average power. As both the modulated signal and the filtered ASE are equivalent the ratio of their combination does not affect the resultant level of TPA generated photocurrent. For the CW signal case (circles in Fig. 7.4) the dependence of the TPA generated photocurrent on OSNR can be clearly seen. The dependence on

the OSNR can be seen to be well fit by (7.26). In carrying out the fitting for both curves a constant C was used as a fitting parameter with the same value of C used to calculate both curves.

7.6 Conclusion

The TPA generated by BL-ASE noise was shown analytically and experimentally to have the same mean power dependence as an on-off modulated signal with a generalised duty cycle equal to 50 %. A simple formula is derived to describe the TPA dependence on the OSNR for an optically amplified signal with polarised BL-ASE noise. The theory was validated by carrying out an OSNR measurement using a TPAM and the theory was shown to fit the measured data very well.

8. Two-photon absorption microcavity applications

8.1 Channel identification

8.1.1 Optical channel monitoring

Optical performance monitoring (OPM) is a very general term that refers to monitoring the fidelity of the transmission of an optical signal through a network, see section 1.4.4. OPM has been receiving attention for the last number of years [48-50]. It is hoped that via the use of OPM that increased flexibility, reliability and functionality can be achieved in optical networks. A number of different monitoring techniques have been mooted based on linear detection schemes. The most common OPM usages focus around the monitoring of average signal power, channel power, channel wavelength, degree of signal polarisation and spectral OSNR [48, 54-56]. Also a number of monitoring schemes based on placing low frequency modulated signals on the transmitted signal and then monitoring these low frequencies at different points throughout the network [61]. These schemes suffer from a number of drawbacks related to the quality of the information that can be garnered from the measurement as well as the interpretation of multiple impairments resulting in problems interpreting the measured result as well as implementation cost. One very useful method of monitoring a network performance would be to detect the data being transmitted through the network at each amplification node in the network. The problem with this is that the high speed electronics required are too expensive and so lower cost monitoring schemes are needed. These schemes should give more detailed or more cost effective network performance data.

8.1.2 Need for channel identification

In addition to signal quality an important requirement for managing dense wavelength division multiplexed networks is channel identification [19]. This application is especially difficult in transparent mesh networks, which are used for transmission of channels with multiple modulation formats and bit rates. Reconfigurable networks may contain channels which have travelled across different parts of the network, so each channel must be independently monitored. Due to the small wavelength separation of channels (i.e. 0.4 nm, 0.8 nm) and the different filtering of the spectrum between channels in DWDM systems, it is vital to carry out this monitoring within the channel band. Channel loss after traversing a number of nodes can result in spectrally shaped noise peaks with average power very similar to that of a signal bearing channel, making them quite difficult to identify. As TPA is dependent on d_{gen} (see section 7.1) and as different signal types generally have different values of d_{gen}, TPA can be used as a good indication of both channel presence and channel identity.

8.1.3 Channel identification measurement

TPA measurements were carried out using cavities which were grown to have a value of $R = 0.87$ (see chapter 3) with a resonant wavelength (λ_0) of 1565 nm. A schematic of the setup used is shown in Fig. 8.1. The setup allowed for the combination of up to four signal channels using a series of 50:50 beam splitters. The channels used in this measurement were a CW signal, a 10 Gbs^{-1} signal which is encoded so as to be 33 % return to zero on off keyed (RZOOK) pseudo random binary sequence (PRBS, 2^{32}-1) signal, ASE channel (BL-ASE) and a 40 Gbs^{-1} PRBS non-return to zero (NRZ) differential phase-shift keyed (DPSK) signal. The CW signal is generated by a tuneable external cavity laser (TLS). The 43 Gbs^{-1} NRZ-DPSK signal is generated using a 2V-π driven Mach-Zehnder

amplitude modulator. Each of the signal channels (excluding the ASE channel) is taken to nominally have an OSNR value > 25 dB. The CW signal was used in order to characterise the spectral response of the TPAM, see Fig. 8.2. The ASE source comprises of an EDFA with no input optical signal and the output is passed through a 0.2 nm band pass filter (BPF). The ASE channel is of interest as it emulates the effect of a lost channel in a network after it has been transmitted through a number of nodes, which results in filtered noise that in the spectral domain looks very similar to a signal bearing channel.

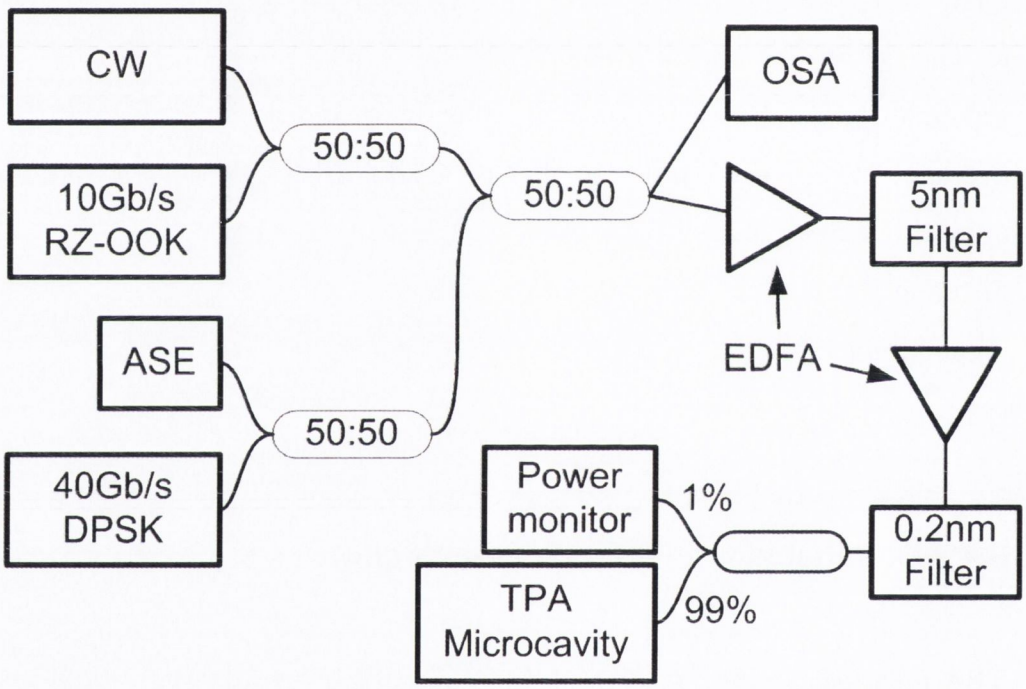

Fig. 8.1 Experimental setup for optical performance monitoring

Half of the combined signal power is passed to an OSA which is used to align the signal channel wavelengths which are set to be spaced by 0.4 nm (50 GHz). The wavelengths of the signal channels being investigated are aligned so as to be close to the peak spectral response of the TPAM, which in Fig. 8.2 is shown to be approximately 1565 nm. The combined signals are then amplified using an EDFA. The output of the EDFA is passed through a BPF with a 5 nm pass-band. The purpose of this filter is to reduce the level of power present (as

ASE or remaining EDFA pump laser) outside the wavelength region of the signals under test. During the measurement the position of this filter is kept constant at 1565.5 nm. The presence of this filter allows the output power from the subsequent EDFA to be higher as gain is not used up on wavelength regions which are not being investigated. The output of the BPF is then passed through another EDFA, and through a 0.2 nm BPF (which is used here as a channel filter). The channel filter is scanned during the channel identification measurement in order to pick out individual channels. The output of the channel filter is then passed through as 99:1 beam splitter with 99 % of the power going to the TPAM and the remaining 1 % is sent to an average power meter.

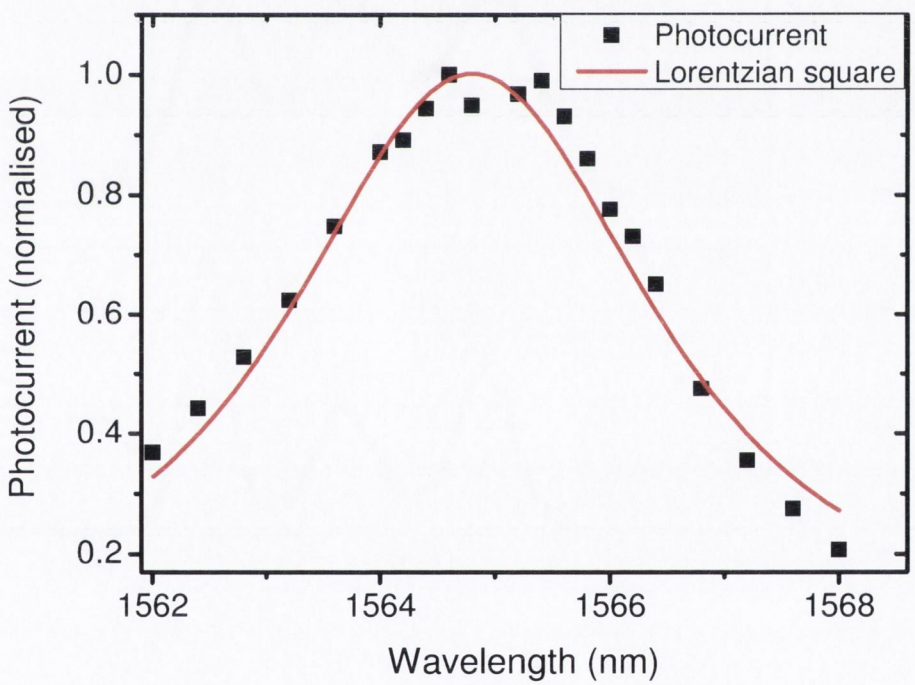

Fig. 8.2 Spectral dependence of the square root of the generated photocurrent with the photocurrent normalised to the peak response

Initially the channel filter is centred on each of the signal channels in turn and the polarisation of the signal channel is adjusted (using a manual polarisation controller which is placed on each signal arm before the signals are multiplexed together). The polarisation of each signal is rotated so as to maximise the TPA

generated photocurrent which is generated by each of the signals when they are incident on the TPAM (excluding the ASE channel which is taken to be depolarised). The polarisation of each of the signal channels is kept constant throughout the measurement so that the effect of polarisation dependence of the TPAM can be excluded from this measurement (except for the case of the ASE signal), see chapter 6. The peak average power of each of the signals within the channel filter bandwidth is adjusted so that for all signals the peak SPA response is the same (for a slow speed SPA detector which in this case is an Agilent average power meter), as is the case for DWDW systems, see Fig. 8.3 (top).

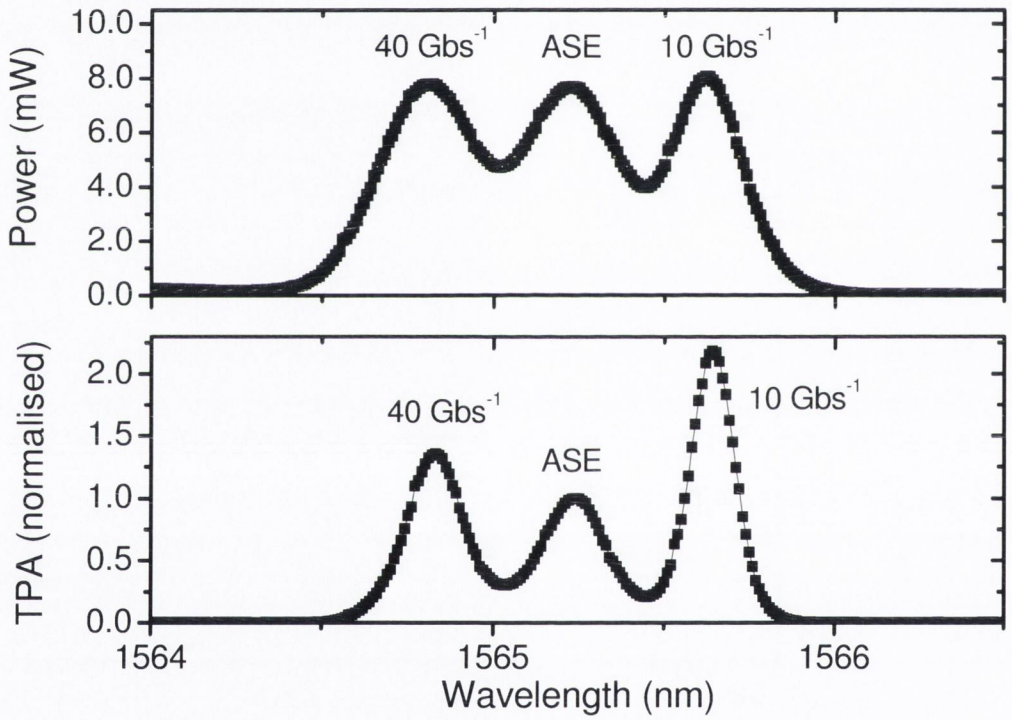

Fig. 8.3 Single photon (SPA, top) and two-photon absorption generated photocurrent (TPA, bottom) spectra for 40 Gbs^{-1} NRZ-DPSK, 0.2 nm filtered ASE noise, and 10 Gbs^{-1} 33 % RZ-OOK from short to long wavelength respectively. Spectra were scanned using a 0.2 nm tunable grating filter. The Average power is calibrated so as to report the level of optical power incident in the TPAM

Fig. 8.3 (top) shows the average power that is passed through the channel filter as it is tuned from 1564 nm to 1566.5 nm. As each of the signals have the same

peak average power in the channel filter bandwidth it is not possible to identify the channel type from the average power data. As the SPA data was taken the signal is simultaneously incident on the TPAM. The TPA signal has been scaled by the square of the average power so that all TPA responses correspond to the same average power, and the signal is then normalised by the peak ASE response, see Fig. 8.3 bottom. The TPA response is seen to be different for each of the signals under test. The 10 Gbs^{-1} signal channel is seen to have the largest TPA response followed by the 40 Gbs^{-1} signal channel and finally the filtered ASE channel with a ratio of peak response of 2.17:1.34:1 respectively. Also due to the square response of the TPA detector there is improved discrimination between each of the individual channels when compared with the SPA case.

The exact ratios of the TPA signal generated in this measurement were not fitted theoretically. For most signals this is simply a calculation of d_{gen}. The problem with such a simple calculation is that there is contribution to the TPA signal from a range of different signal impairments present in a network environment. The level of TPA signal can be affected by various amounts by contributions such as OSNR, dispersion and polarisation mode dispersion [19, 67, 86]. Also while the level of TPA generated by an ASE signal has been investigated in [67] it has yet to investigated for a depolarised ASE signal. The level of TPA generated by the NRZ-DPSK signal is also larger than one might expect. If the signal was simply an ideal NRZ-DPSK signal then it would generate the same level of TPA as a CW signal. Due to the method of creating the DSPK signal in these measurements there is a small amplitude modulation as the signal transitions from a 1 to a 0 and vice-versa which results in a larger amount of TPA generated photocurrent. It is due to these contributions that a theoretically fitting of the data shown in Fig. 8.3 has not been carried out.

8.2 Temperature tuning

8.2.1 Microcavity tuning

In order for OPM to be used in a DWDM network it must be capable of accessing a large number of channels over a broad wavelength range i.e. 1530 nm – 1565 nm (C band). In the case of a TPAM it intrinsically has a built-in filter with a spectral full-width at half-maximum (FWHM) about an order of magnitude narrower than the C band. This means that in order to use one detector to monitor several channels in a DWDM system requires that these detectors be tunable. Previously, it has been reported that these cavities can be tuned by 55 nm using angle tuning, thereby allowing one device to cover the entire C band [92]. Angle tuning, however, will cause the detector response to change, due to changes in the TPA enhancement factor and polarisation sensitivity of the photodetector response [92]. As well as this, the moving parts required to enable angular tuning in general add cost and reduce reliability and therefore its use is prohibitively expensive. Instead the use of temperature based tuning which has previously been demonstrated as a robust, cost effective means of tuning is demonstrated here [93]. In order for temperature based tuning to be used it is first necessary to fully understand the temperature dependence of the response of a TPAM [94].

8.2.2 Temperature tuning

A schematic of the experimental setup used to investigate the temperature dependence of a TPAM response is shown in Fig. 8.4. An external cavity tuneable laser source (TLS) which is internally modulated at 300 kHz ($d_{gen} = 0.5$) is used. The use of the modulation lowers the amount of optical power needed to be incident on the TPAM and still be able to access the TPA dominated

absorption regime. The signal was then passed through an EDFA and a variable optical attenuator (VOA). 1 % of the output power from the VOA was sent to a InGaAs photodiode (PD) which was calibrated so as to record the level of optical power onto the TPAM. The remainder of the optical signal (99 %) is passed through a polarisation controller (PA). The PA consists of a manual fibreised polarisation controller, a polarizer and a half- and quarter-wave plate. The manual polarisation controller allows the optical power transmitted through the polarizer to be maximized. Using the PA the polarisation of the input signal onto the TPAM was rotated so as to maximise the level of TPA generated photocurrent. The output from the PA is passed through a fibre lens before being normally incident on the TPAM. The average optical power output from the lens was measured once the setup was in place using a calibrated power meter. This recorded output power value was used to calibrate the InGaAs photodiode so that it could be used to measure the optical power output on to the TPAM.

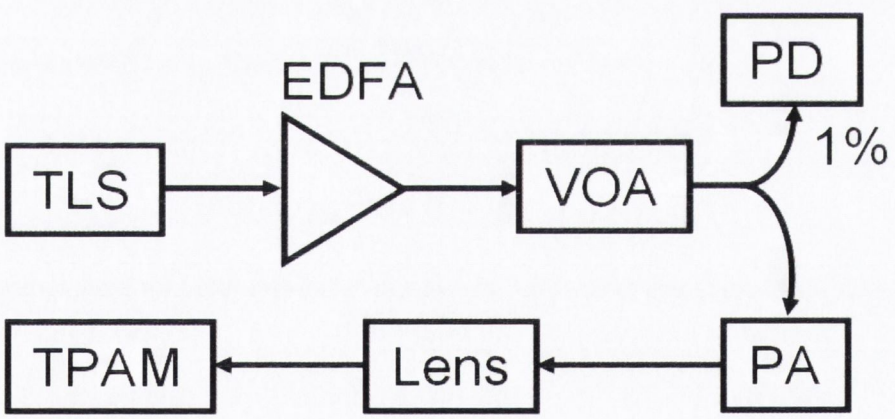

Fig. 8.4 Schematic of device used for temperature tuning, TLS is a tuneable laser source, VOA is a variable optical attenuator, PD is an average power meter, PA is a polarisation controller

The TPAM structure used for the temperature study is an 8 ps TPAM, see chapter 3. The detector is mounted on a thermo electric cooler which was mounted on a copper block which in turn was mounted on a large heat sink. The copper block on which the TPAM was mounted was covered with polystyrene in order to insulate it from the air which allowed for faster temperature tuning as

well as an increased tuning range. The temperature was controlled by the thermoelectric cooler which with these setup conditions allowed the temperature stabilization to be within ± 0.4 ^{0}C of the set temperature. The focusing of the input signal was carried out by mounting the fibre lens on a nano-max micro positional stage.

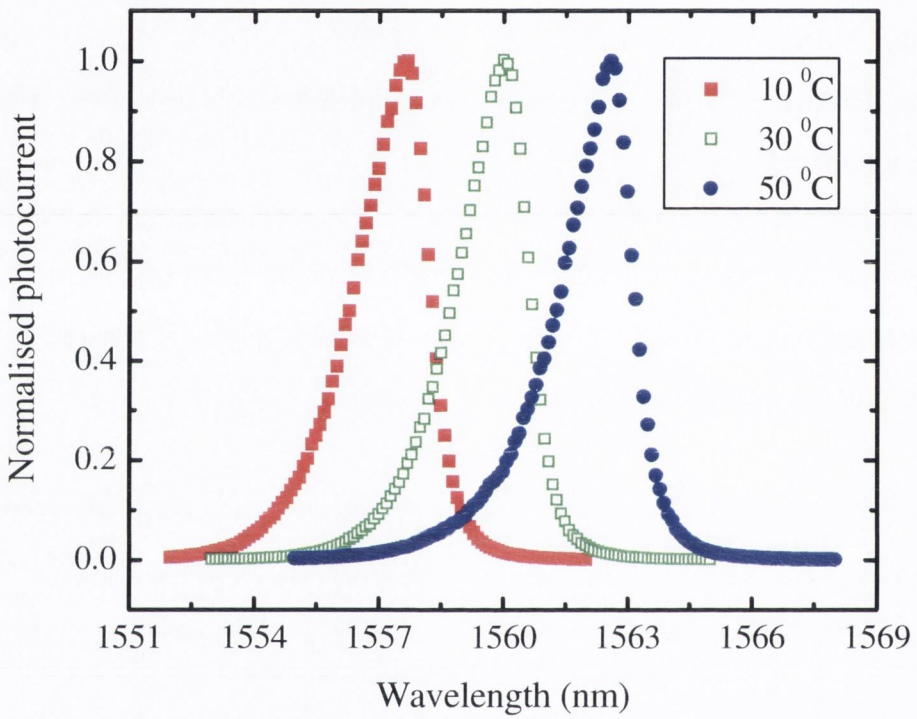

Fig. 8.5 Wavelength response of the TPAM against temperature, for three temperatures

To characterise the shift in resonance position with changing device temperature, the wavelength of the input signal is scanned across the resonance while the power onto the device is kept constant at 6 mW for a range of different temperatures, and the photocurrent is recorded as shown in Fig. 8.5. As can be seen from Fig. 8.5 both the spectral width and shape are independent of temperature in the investigated range (10 – 50 ^{0}C). The change in peak current detected at resonance is $\leq$ 6 % arising from misalignment due to thermal expansion of the block on which the detector is mounted. To minimize the influence of the misalignment the detector was realigned for each temperature. The detector was re-aligned by centring the input signal in the aperture of the

TPAM and adjusting the focus of the lens so as to maximise the TPA generated photocurrent. From the investigation of the TPA spectral dependence the dependence of the cavity resonant wavelength (λ_0) is found, see Fig. 8.6. A linear tuning rate of 0.125 nm/^{0}C (dependence of refractive index on temperature is 2.7 $\times 10^{-4}K^{-1}$) is observed as shown in Fig. 8.6.

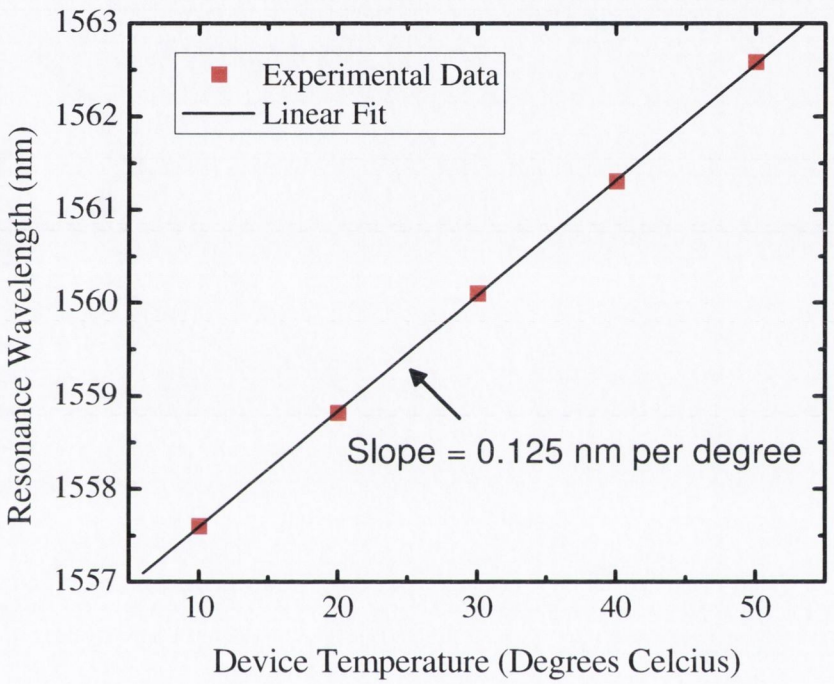

Fig. 8.6 TPAM resonance wavelength against temperature

By changing the TPAM temperature from 10 ^{0}C to 50 ^{0}C a tuning range of 5 nm has been achieved. The photocurrent vs. power has been recorded on resonance at each different temperature, see Fig. 8.7. The power is varied using the VOA, while the TLS wavelength is kept constant. The dependence of the TPA generated photocurrent for the TPAM on resonance at a number of different temperatures was also investigated. This measurement was carried out by setting the device temperature and then varying the input wavelength of the TSL until the generated TPA photocurrent was maximised. The input optical power onto the device was then varied while the input wavelength was kept constant, see Fig. 8.7. Also shown on Fig. 8.7 are two lines with slopes of 1 and 2 which on a log-

log graph corresponds to the SPA and TPA dominated regimes respectively. From Fig. 8.7 it can be seen that the photocurrent response of the detector on resonance at different temperatures remains unchanged. Both the TPA and SPA regimes remain unchanged with no noticeable change in the absolute current for a particular power level.

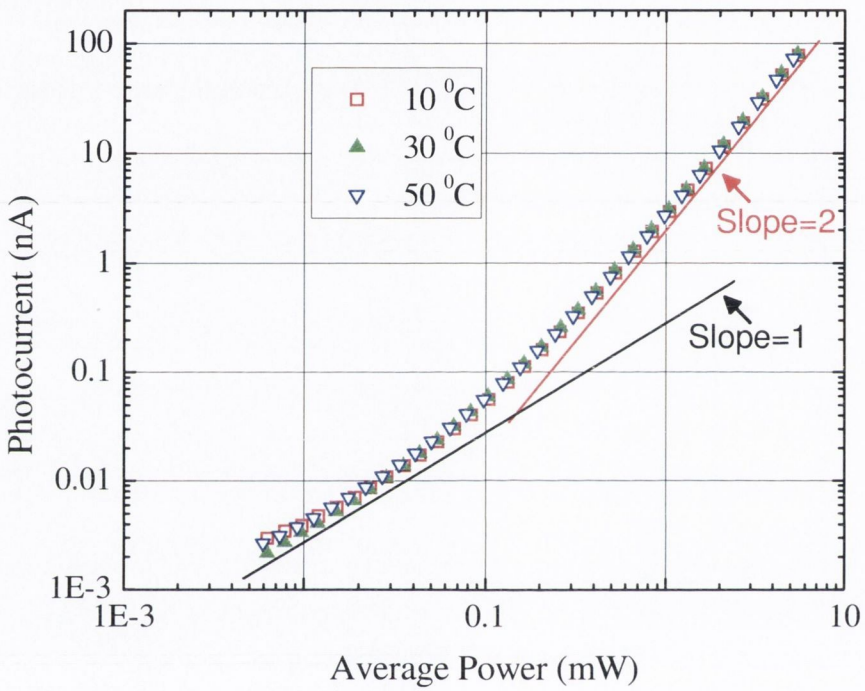

Fig. 8.7 Photocurrent dependence on incident power for different temperatures with the wavelength fixed for each scan at the resonant wavelength (for that particular temperature) of the TPAM

The demonstrated temperature dependence of the TPAM shows the detector can be tuned across a 5 nm range by changing the temperature from 10 ^{0}C to 50 ^{0}C without any difficulty. Furthermore, the detector is shown to be highly stable with varying temperature as only the resonant wavelength of the detector changes. This is unlike Silicon APDs, where the response of the detector can be highly temperature sensitive [95]. Using temperature tuning it is possible to monitor a DWDM system across the entire C band using approximately 3 - 4 detectors at fixed angles and then temperature tuning each device to pick out

individual channels. While the temperature control circuit used in this investigation allowed only a relatively narrow temperature tuning range (over 40 ^{0}C), lasers in modern networks commonly operate from -40 ^{0}C to 85 ^{0}C [96]. If a TPAM were tuned across a similar temperature range then this increased tuning range would allow the single TPAM discussed above to be tuned by > 15 nm.

8.3 Conclusion

TPA based optical channel identification is demonstrated as being capable of differentiating between different types of signals as well as between different signals and BL-ASE. It is also shown that a TPAM can easily be tuned across a 5 nm range by changing the temperature from 10 to 50 ^{0}C. Furthermore, the detector is shown to be highly stable with varying temperature as only the resonant wavelength of the detector changes. This is unlike Silicon APDs, where the response of the detector can be highly temperature sensitive [95]. Using temperature tuning it will be possible to monitor a WDM system across the entire C band using approximately 3-4 detectors at fixed angles and then temperature tuning each device to pick out individual channels. While our temperature control circuit allowed only a relatively narrow temperature tuning range of just over 40 ^{0}C, lasers in modern networks commonly operate from -40 ^{0}C to 85 ^{0}C. This increased tuning range would allow the single TPAM device discussed above to be tuned by > 15 nm.

9. Conclusions and future work

9.1 Conclusion

The most important feature of a TPAM is that of its enhancement of the optical field in order to enhance the level of TPA generated photocurrent for a particular input optical power incident on the detector. The TPAM is shown in chapter 4 to not only enhance the level of TPA but also to relatively suppress the level of residual SPA [79]. This allows a TPA dominated signal to be accessed at much lower incident optical powers than would be possible with a similar GaAs absorbing region that is not sandwiched between two highly reflective DBR mirrors. The TPA coefficient is estimated to be approximately 15 cm/GW at 1560 nm in (001) GaAs. The residual SPA coefficient in the unintentionally doped GaAs active layer of the TPAM which is grown by metal-organic chemical vapour deposition is approximately 1.0×10^{-4} cm^{-1} (which is an extremely small value).

A TPAM has previously been suggested for use as an efficient TPA detector [71, 72]. The demonstration of the use of a TPAM in autocorrelator applications [97], optical sampling [42] demultiplexing of OTDM signals [30] and in dispersion monitoring [86] has previously been shown. In order to further facilitate these applications as well as a range of other TPA based applications a characterisation of the TPAM has been carried out and detailed in this thesis.

Even with the enhancement provided by the TPAM it is still necessary to focus the input beam onto the TPAM in order to operate in the TPA dominated absorption regime at low optical input powers. A TPAM has a limited acceptance angle and so different angular components have different levels of enhancement in the cavity. For a TPAM detector, this results in an asymmetrical cavity spectral response and also an asymmetrical response to the focus position, see chapter 5. The influence of the acceptance angle on the TPA response of the

TPAM means that to optimize the level of TPA generated by a TPAM, the optimal spot size for the TPAM must be calculated. In chapter 5, an optimized incident focused spot diameter of 7 μm has been calculated as being optimal so as to maximize the generated TPA photocurrent for the R = 0.965 TPAM under test. While measurements were only carried out in chapter 5 for a TPAM with R = 0.965, it is shown that the theory described can also be used to calculate the optimal incident focused spot size for cavities with different values of R. With increasing TPAM cavity lifetime the dependence on incident angle becomes increasingly important and as such the optimal incident spot size will increase.

In chapter 6, the polarisation response of a TPAM was investigated. The deviation in the dependence of the detector response from that of bulk GaAs is shown to be due to the birefringence of the cavity. A theoretical model based on the convolution of the cavity birefringence and the polarisation dependence of two-photon absorption in GaAs is described and shown to match the measured polarisation dependence of the TPAM very well.

In chapter 7, the TPA generated by BL-ASE noise was shown analytically and experimentally to have the same mean power dependence as an on-off modulated signal with a generalised duty cycle equal to 50 %. A simple formula is derived to describe the TPA dependence on the OSNR for an optically amplified signal with polarised BL-ASE noise. The theory was validated by carrying out an OSNR measurement using a TPAM and the theory was shown to fit the measured data very well.

In chapter 8, TPA based optical channel identification is demonstrated as being capable of differentiating between different types of signals as well as between different signals and BL-ASE. It is also shown in chapter 8 that a TPAM can easily be tuned across a 5 nm range by changing the temperature from 10 to 50 ^{0}C. Furthermore, the detector is shown to be highly stable with varying temperature as only the resonant wavelength of the detector changes. This is unlike Silicon APDs, where the response of the detector can be highly temperature sensitive [95]. Using temperature tuning it will be possible to monitor a WDM system across the entire C band using approximately 3-4

detectors at fixed angles and then temperature tuning each device to pick out individual channels. While our temperature control circuit allowed only a relatively narrow temperature tuning range of just over 40 ^{0}C, lasers in modern networks commonly operate from -40 ^{0}C to 85 ^{0}C. This increased tuning range would allow the single TPAM device discussed above to be tuned by > 15 nm.

9.2. Future work

That a TPAM can be used as a TPA detector has been shown along with schemes to characterise the response of a TPAM. Future work in this field can be broken up into two directions which are firstly further device design and secondly further investigation of TPA monitoring applications.

Current TPAM have been grown using GaAs/AlAs mirror pairs. The use of GaAs/AlAs as the material system for the DBR places some limitations on how the detector response can be tailored to individual applications. If the GaAs/AlAs used for the DBR were replaced with a dielectric material system (i.e. TiO_2/SiO_2) there would be a number of advantages. The large contrast in refractive indices between mirror layers that is possible with dielectric materials would allow for fewer mirror pairs as well as making it easier to alter the shape of the reflectivity response of these mirrors [98]. The increased ability to shape the reflectivity response would make it possible to better tailor the TPAM transfer function to optimise the TPA signal for a channel in a DWDM network. The FWHM of the TPAM was tailored so as to be less than 0.4 nm and to also have stronger wavelength dependence than the current Lorentzian line shape (i.e. using a coupled cavity) [99]. This would allow a TPAM to be used without the need for a channel filter (i.e. for a 10Gbs^{-1} 50 GHz spaced DWDM network). The removal of the channel filter would reduce cost, add reliability as well as reduce the signal power necessary onto the TPAM (due to the removal of the loss associated with a filter). Another effect of the dielectric mirrors would be to

remove the influence of the electro-optic effect in the mirrors which has been associated with the complication of the polarisation dependence of TPAM.

The current TPAM absorbing region is made from GaAs. There a number of downsides associated with the choice of GaAs as the absorbing region. The primary problem is associated with creating integrated circuits in GaAs as integrated circuits are traditionally made from Silicon. A serious limitation in carrying out applications such as optical sampling using a TPAM is the low level of TPA current that is created by an individual pulse. Efforts to amplify the signal externally can introduce large amounts of noise. A way around this would be to integrate an avalanche photodiode (APD) into the detector which could provide up to 30 dB of electrical gain [100]. Integrating an APD into a GaAs structure is very difficult, but integrating it in Silicon material system is much easier. While the TPA coefficient of Silicon around 1550 nm is approximately 0.44 cm/GW (which is approximately 34 times less that the TPA coefficient in GaAs) it is thought that the low level of defects in Si will reduce the level of SPA so this low TPA coefficient will not be a problem [101]. Silicon APD's have previously been widely reported for use as a TPA detector although no work has been done to date to the best of my knowledge on combining both an APD and a microcavity as a TPA detector [44, 102].

There are also slightly modified detector structures which would allow further detection schemes with two detector design options which seem most promising. The first is to grow TPAM's with a wedged active region [103]. This wedged structure would mean devices from different parts of the wafer would result in detectors with different resonant wavelengths. By properly tailoring the slope of the wedged layer it should then be possible to process a number of devices beside each other in the wafer and process them to be an array of devices with a wavelength specific separation (i.e. 50 GHz or 100 GHz so as to line up with the ITU grid). It would also be possible to create coupled cavities which possess 2 spacer regions which are sandwiched between 3 DBR's. This results in two resonant wavelengths (with the wavelength being controlled by the individual thickness of the two spacer regions) which would allow the TPAM to

be used in a sampling measurement with both pump and probe at different wavelengths.

References

1. G. P. Agrawal, "Fiber-optic communication systems," A John Wiley & Sons, Inc (2002).
2. T. Kato, Y. Koyano, and M. Nishimura, "Temperature dependence of chromatic dispersion in various types of optical fibers," in *Optical Fiber Communication Conference*, 2000), 104-106 vol.101.
3. P. C. Noutsios, "In-service Measurements of Polarization Fluctuations on Field-installed OC-192 DWDM Systems," in *Signals, Systems and Electronics. ISSSE. International Symposium on*, 2007), 323-326.
4. V. W. S. Chan, K. L. Hall, E. Modiano, and K. A. Rauschenbach, "Architectures and technologies for high-speed optical data networks," J. Lightwave Technol. **16**, 2146-2168 (1998).
5. G. P. Agrawal, *Nonlinear fiber optics,* 4th ed. (Academic press, 2007).
6. R. W. Boyd, *Nonlinear optics,* 3rd ed. (Academic press, 2007).
7. P. N. Butcher and D. Cotter, *The elements of nonlinear optics* (Cambridge University Press, 1990).
8. T. H. Maiman, "Stimulated Optical Radiation in Ruby," Nature **187**, 493-494 (1960).
9. P. A. Franken, A. E. Hill, C. W. Peters, and G. Weinreich, "Generation of optical harmonics," Physical Review Letters **7**, 118-120 (1961).
10. G. S. He and S. H. Liu, *Physics of Nonlinear Optics: Guang S. He, Song H. Liu* (World Scientific, 1999).
11. M. D. Dvorak, W. A. Schroeder, D. R. Andersen, A. L. Smirl, and B. S. Wherrett, "Measurement of the anisotropy of two-photon absorption coefficients in Zincblende semiconductors," IEEE J. Quantum Electron **30**, 256-268 (1994).
12. C. Dorrer and I. Kang, "Complete temporal characterization of short optical pulses by simplified chronocyclic tomography," Opt. Lett. **28**, 1481-1483 (2003).

13. R. L. Jungerman, G. Lee, O. Buccafusca, Y. Kaneko, N. Itagaki, R. Shioda, and A. Technologies, "Optical Sampling Reveals Details of Very High Speed Fiber Systems," pdf document, Agilent Technologies, www.agilent.com (2004).

14. K. J. Blow, N. J. Doran, and B. P. Nelson, "Demonstration of the nonlinear fibre loop mirror as an ultrafast all-optical demultiplexer," Electron. Lett. **26**, 962-964 (1990).

15. D. J. Kane and R. Trebino, "Characterization of arbitrary femtosecond pulses using frequency-resolved optical gating," IEEE J. Quantum Electron **29**, 571-579 (1993).

16. T. Ng, J. L. Blows, M. Rochette, J. A. Bolger, I. Littler, and B. Eggleton, "In-band OSNR and chromatic dispersion monitoring using a fibre optical parametric amplifier," Optics Express **13**, 5542-5552 (2005).

17. C. Xu, J. M. Roth, W. H. Knox, and K. Bergman, "Ultra-sensitive autocorrelation of 1.5 μm light with single photon counting silicon avalanche photodiode," Electron. Lett. **38**, 86-88 (2002).

18. M. Saruwatari, "All-optical signal processing for terabit/second optical transmission," Selected Topics in Quantum Electronics, IEEE Journal of **6**, 1363-1374 (2000).

19. S. Wielandy, M. Fishteyn, and B. Zhu, "Optical performance monitoring using nonlinear detection," J. Lightwave Technol. **22**, 784-793 (2004).

20. W. Kaiser and C. G. B. Garrett, "Two-Photon Excitation in CaF_2: Eu^{2+}," Physical Review Letters **7**, 229-231 (1961).

21. F. R. Laughton, J. H. Marsh, D. A. Barrow, and E. L. Portnoi, "The two-photon absorption semiconductor waveguide autocorrelator," IEEE J. Quantum Electron **30**, 838-845 (1994).

22. H. N. Spector, "Two-photon absorption in semiconducting quantum-well structures," Phys. Rev. B **35**, 5876-5879 (1987).

23. D. C. Hutchings and B. S. Wherrett, "Theory of anisotropy of two-photon absorption in zinc-blende semiconductors," Phys. Rev. B **49**, 2418-2427 (1994).

24. D. M. Spirit, A. D. Ellis, and P. E. Barnsley, "Optical time division multiplexing: systems and networks," Communications Magazine, IEEE **32**, 56-62 (1994).

25. I. Kaminow, L. Tingye, and A. Willner, *Optical fiber telecommunications V* (Elsevier, 2008), Vol. B.

26. S. Weisser, S. Ferber, L. Raddatz, R. Ludwig, A. Benz, C. Boerner, and H. G. Weber, "Single- and alternating-polarization 170-Gb/s transmission up to 4000 km using dispersion-managed fiber and all-Raman amplification," IEEE Photon. Technol. Lett. **18**, 1320-1322 (2006).

27. H. G. Weber, S. Ferber, M. Kroh, C. Schmidt-Langhorst, R. Ludwig, V. Marembert, C. Boerner, F. Futami, S. Watanabe, and C. Schubert, "Single channel 1.28 Tbit/s and 2.56 Tbit/s DQPSK transmission," Electron. Lett. **42**, 178-179 (2006).

28. B. C. Thomsen, J. M. Dudley, J. D. Harvey, and L. P. Barry, "Demonstration of demultiplexing in high speed OTDM systems using a two photon absorption based switch," in *Optical Fiber Communication Conference and Exhibit. OFC*, 2001), WO2-1-WO2-3 vol.3.

29. P. J. Maguire, L. P. Barry, T. Krug, W. H. Guo, J. O'Dowd, M. Lynch, A. L. Bradley, J. F. Donegan, and H. Folliot, "Optical Signal Processing via Two-Photon Absorption in a Semiconductor Microcavity for the Next Generation of High-Speed Optical Communications Network," J. Lightwave Technol. **24**, 2683-2692 (2006).

30. P. Maguire, L. P. Barry, T. Krug, J. O'Dowd, M. Lynch, A. L. Bradley, J. F. Donegan, and H. Folliot, "Direct measurement of a high-speed (>100Gbit/s) OTDM data signal utilising two-photon absorption in a semiconductor microcavity," in *Lasers and Electro-Optics Society. LEOS*, 2005), 142-143.

31. P. J. Maguire, L. P. Barry, T. Krug, M. Lynch, A. L. Bradley, J. F. Donegan, and H. Folliot, "Simulation of a high-speed demultiplexer based on two-photon absorption in semiconductor devices," Optics Communications **249**, 415-420 (2005).

32. L. P. Barry, B. C. Thomsen, J. M. Dudley, and J. D. Harvey, "All optical demultiplexing based on two-photon absorption in a laser diode," in *Optical Communication. 24th European Conference on*, 1998), 111-112 vol.111.

33. L. P. Barry, B. C. Thomsen, J. M. Dudley, and J. D. Harvey, "Autocorrelation and ultrafast optical thresholding at 1.5 μm using a commercial InGaAsP 1.3 μm laser diode," Electron. Lett. **34**, 358-360 (1998).

34. L. P. Barry, P. G. Bollond, J. M. Dudley, J. D. Harvey, and R. Leonhardt, "Autocorrelation of ultrashort pulses at 1.5 μm based on nonlinear response of silicon photodiodes," Electron. Lett. **32**, 1922-1923 (1996).

35. K. Naganuma, K. Mogi, and H. Yamada, "General method for ultrashort light pulse chirp measurement," IEEE J. Quantum Electron **25**, 1225-1233 (1989).

36. Y. Takagi, T. Kobayashi, K. Yoshihara, and S. Imamura, "Multiple- and single-shot autocorrelator based on two-photon conductivity in semiconductors," Opt. Lett. **17**, 658-660 (1992).

37. T. Hattori, Y. Kawashima, M. Daikoku, H. Inouye, and H. Nakatsuka, "Autocorrelation measurement of femtosecond optical pulses based on two-photon photoemission in a photomultiplier tube," Japanese Journal of Applied Physics, Part 2: Letters **39**, L809-L811 (2000).

38. F. R. Laughton, J. H. Marsh, and A. H. Kean, "Very sensitive two-photon absorption GaAs/AlGaAs waveguide detector for an autocorrelator," Electron. Lett. **28**, 1663-1665 (1992).

39. J. K. Ranka, A. L. Gaeta, A. Baltuska, M. S. Pshenichnikov, and D. A. Wiersma, "Autocorrelation measurement of 6-fs pulses based on the two-photon-induced photocurrent in a GaAsP photodiode," Opt. Lett. **22**, 1344-1346 (1997).

40. J. D. Harvey, J. M. Dudley, B. C. Thomsen, and L. P. Barry, "Ultra-sensitive optical autocorrelation using two photon absorption," in *Optical Fiber Communication Conference, and the International Conference on*

Integrated Optics and Optical Fiber Communication. OFC/IOOC. Technical Digest, 1999), 2-4 vol.3.

41. C. Jung-Ho and A. M. Weiner, "Ambiguity of ultrashort pulse shapes retrieved from the intensity autocorrelation and the power spectrum," Selected Topics in Quantum Electronics, IEEE Journal of **7**, 656-666 (2001).
42. P. J. Maguire, L. P. Barry, T. Krug, M. Lynch, A. L. Bradley, J. F. Donegan, and H. Folliot, "All-optical sampling based on two-photon absorption in a semiconductor microcavity for high-speed OTDM," Proceedings of SPIE-The International Society for Optical Engineering **5825**, 316-325 (2005).
43. P. J. Maguire, L. P. Barry, T. Krug, M. Lynch, A. L. Bradley, J. F. Donegan, and H. Folliot, "All-optical sampling utilising two-photon absorption in semiconductor microcavity," Electron. Lett. **41**, 489-490 (2005).
44. K. Kikuchi, "Optical sampling system at 1.5 μm using two photon absorption in Si avalanche photodiode," Electron. Lett. **34**, 1354-1355 (1998).
45. G. P. Agrawal, *Lightwave technology: telecommunication systems* (Wiley, 2005).
46. R. Salem and T. E. Murphy, "Broad-band optical clock recovery system using two-photon absorption," IEEE Photon. Technol. Lett. **16**, 2141-2143 (2004).
47. R. Salem, A. A. Ahmadi, G. E. Tudury, G. M. Carter, and T. E. Murphy, "Two-Photon Absorption for Optical Clock Recovery in OTDM Networks," J. Lightwave Technol. **24**, 3353-3362 (2006).
48. D. C. Kilper, R. Bach, D. J. Blumenthal, D. Einstein, T. Landolsi, L. Ostar, M. Preiss, and A. E. Willner, "Optical performance monitoring," J. Lightwave Technol. **22**, 294-304 (2004).
49. G. R. Hill, P. J. Chidgey, F. Kaufhold, T. Lynch, O. Sahlen, M. Gustavsson, M. Janson, B. Lagerstrom, G. Grasso, F. Meli, S. Johansson,

J. Ingers, L. Fernandez, S. Rotolo, A. Antonielli, S. Tebaldini, E. Vezzoni, R. Caddedu, N. Caponio, F. Testa, A. Scavennec, M. J. O'Mahony, J. Zhou, A. Yu, W. Sohler, U. Rust, and H. Herrmann, "A transport network layer based on optical network elements," J. Lightwave Technol. **11**, 667-679 (1993).

50. S. Sygletos, I. Tomkos, and J. Leuthold, "Technological challenges on the road toward transparent networking," J. Opt. Netw. **7**, 321-350 (2008).
51. J. B. Rosolem, C. Floridia, J. A. Matiuso, J. R. F. de Oliveira, R. F. da Silva, J. C. Martins, R. Arradi, and A. Paradisi, "Intelligent optical monitoring system for integrated management of DWDM networks," in *Microwave and Optoelectronics Conference. IMOC. SBMO/IEEE MTT-S International*, 2007), 346-350.
52. C. Pinart, R. Martinez, and G. Junyent, "Experimental implementation of dynamic in-service performance monitoring for lambda services," in *ECOC*, 2005), 969–970.
53. R. Martinez, C. Pinart, F. Cugini, N. Andriolli, L. Valcarenghi, P. Castoldi, L. Wosinska, J. Cornelias, and G. Junyent, "Challenges and requirements for introducing impairment-awareness into the management and control planes of ASON/GMPLS WDM networks," Communications Magazine, IEEE **44**, 76-85 (2006).
54. D. C. Kilper and W. Weingartner, "Monitoring Optical Network Performance Degradation Due to Amplifier Noise," J. Lightwave Technol. **21**, 1171-1178 (2003).
55. M. Petersson, H. Sunnerud, B. Olsson, and M. Karlsson, "Multi-Channel OSNR Monitoring for WDM Networks," in *Optical Communication, ECOC. 28th European Conference on*, 2002), 1-2.
56. C. Konishi, T. Yoshida, S. Hamada, K. Asahi, and S. Fujita, "Dynamic gain-controlled erbium-doped fiber amplifier repeater for WDM network," in *Optical Fiber Communication. OFC, Conference on*, 1997), 18-19.

57. A. Richter, W. Fischler, H. Bock, R. Bach, and W. Grupp, "Optical performance monitoring in transparent and configurable DWDM networks," Optoelectronics, IEE Proceedings - **149**, 1-5 (2002).

58. J. H. Lee, D. K. Jung, C. H. Kim, and Y. C. Chung, "OSNR monitoring technique using polarization-nulling method," IEEE Photon. Technol. Lett. **13**, 88-90 (2001).

59. G. D. Bartolini, "Low-cost optical monitoring for DWDM systems," in *OSA Topical Meeting on Optical Amplifiers*, 2004),

60. C. Xie, D. C. Kilper, L. Moller, and R. Ryf, "Orthogonal-Polarization Heterodyne OSNR Monitoring Insensitive to Polarization-Mode Dispersion and Nonlinear Polarization Scattering (Invited Paper)," J. Lightwave Technol. **25**, 177-183 (2007).

61. K. J. Park, S. K. Shin, and Y. C. Chung, "Simple monitoring technique for WDM networks," Electron. Lett. **35**, 415-417 (1999).

62. G. Rossi, T. E. Dimmick, and D. J. Blumenthal, "Optical Performance Monitoring in Reconfigurable WDM Optical Networks Using Subcarrier Multiplexing," J. Lightwave Technol. **18**, 1639-1648 (2000).

63. M. Westlund, P. A. Andrekson, H. Sunnerud, J. Hansryd, and L. Jie, "High-performance optical-fiber-nonlinearity-based optical waveform monitoring," J. Lightwave Technol. **23**, 2012-2022 (2005).

64. I. Amat-Roldán, I. Cormack, P. Loza-Alvarez, E. Gualda, and D. Artigas, "Ultrashort pulse characterisation with SHG collinear-FROG," Opt. Express **12**, 1169-1178 (2004).

65. K. W. DeLong, R. Trebino, J. Hunter, and W. E. White, "Frequency-resolved optical gating with the use of second-harmonic generation," Journal of the Optical Society of America **11**, 2206-2206 (1994).

66. J. O'Dowd, D. C. Kilper, W. H. Guo, J. F. Donegan, and S. Chandrasekhar, "Optical Channel Monitoring Using Two Photon Absorption," in *Lasers and Electro-Optics, and the International Quantum Electronics Conference. CLEOE-IQEC. European Conference on*, 2007), 1-1.

67. W. H. Guo, J. O'Dowd, M. Lynch, A. L. Bradley, J. F. Donegan, L. P. Barry, and D. C. Kilper, "Two-photon absorption generated by optically amplified signals," Electron. Lett. **44**, 1087-1088 (2008).

68. M. Dinu, D. C. Kilper, and H. R. Stuart, "Optical performance monitoring using data stream intensity autocorrelation," J. Lightwave Technol. **24**, 1194-1202 (2006).

69. T. Inui, K. R. Tamura, K. Mori, and T. Morioka, "Bit rate flexible chirp measurement technique using two-photon absorption," Electron. Lett. **38**, 1459-1460 (2002).

70. T. Cechan and N. Takao, "Optical modulator bias monitoring with two-photon-absorption in Si-APD in advanced modulation formats optical transmitters," in *Optical Fiber Communication Conference, and the National Fiber Optic Engineers Conference. OFC*, 2006), 3 pp.

71. H. Folliot, M. Lynch, A. L. Bradley, L. A. Dunbar, J. Hegarty, J. F. Donegan, L. P. Barry, J. S. Roberts, and G. Hill, "Two-photon absorption photocurrent enhancement in bulk AlGaAs semiconductor microcavities," Appl. Phys. Lett. **80**, 1328-1330 (2002).

72. H. Folliot, M. Lynch, A. L. Bradley, T. Krug, L. A. Dunbar, J. Hegarty, J. F. Donegan, and L. P. Barry, "Two-photon-induced photoconductivity enhancement in semiconductor microcavities: a theoretical investigation," Journal of the Optical Society of America B: Optical Physics **19**, 2396-2402 (2002).

73. A. Yariv and P. Yeh, *Photonics: Optical electronics in modern communications,* 6 ed. (Oxford University Press, 2007).

74. W. H. Guo, J. O'Dowd, M. Lynch, A. L. Bradley, J. F. Donegan, and L. P. Barry, "Influence of cavity lifetime on high-finesse microcavity two-photon absorption photodetectors," IEEE Photon. Technol. Lett. **19**, 432-434 (2007).

75. L. K. Anderson and B. J. McMurtry, "High-speed photodetectors," Proceedings of the IEEE **54**, 1335-1349 (1966).

76. G. Hasnain, K. Tai, L. Yang, Y. H. Wang, R. J. Fischer, J. D. Wynn, B. Weir, N. K. Dutta, and A. Y. Cho, "Performance of gain-guided surface emitting lasers with semiconductor distributed Bragg reflectors," IEEE J. Quantum Electron **27**, 1377-1385 (1991).

77. K. Tai, L. Yang, Y. H. Wang, J. D. Wynn, and A. Y. Cho, "Drastic reduction of series resistance in doped semiconductor distributed Bragg reflectors for surface-emitting lasers," Appl. Phys. Lett. **56**, 2496-2498 (1990).

78. P. Zhou, J. Cheng, C. F. Schaus, S. Z. Sun, K. Zheng, E. Armour, C. Hains, W. Hsin, D. R. Myers, and G. A. Vawter, "Low series resistance high-efficiency GaAs/AlGaAs vertical-cavity surface-emitting lasers with continuously graded mirrors grown by MOCVD," IEEE Photon. Technol. Lett. **3**, 591-593 (1991).

79. W. H. Guo, J. O'Dowd, E. Flood, T. Quinlan, M. Lynch, A. L. Bradley, J. F. Donegan, K. Bondarczuk, P. J. Maguire, and L. P. Barry, "Suppression of residual single-photon absorption relative to two-photon absorption in high finesse planar microcavities," IEEE Photon. Technol. Lett. **20**, 1426-1428 (2008).

80. J. O'Dowd, W. H. Guo, E. Flood, M. Lynch, A. L. Bradley, L. P. Barry, and J. F. Donegan, "Polarization dependence of a GaAs-based two-photon absorption microcavity photodetector," Opt. Express **16**, 17682-17688 (2008).

81. E. W. Van Stryland, M. A. Woodall, H. Vanherzeele, and M. J. Soileau, "Energy band-gap dependence of two-photon absorption," Opt. Lett. **10**, 490-492 (1985).

82. A. Villeneuve, C. C. Yang, G. I. Stegeman, C. N. Ironside, G. Scelsi, and R. M. Osgood, "Nonlinear absorption in a GaAs waveguide just above half the band gap," IEEE J. Quantum Electron **30**, 1172-1175 (1994).

83. J. O'Dowd, W. H. Guo, E. Flood, M. Lynch, A. L. Bradley, and J. F. Donegan, "Influence of acceptance angle on high-finesse microcavity two photon absorption photodetectors," in *Photon08*, 2008), MD-7881-7104.

84. M. P. van Exter, A. K. Jansen van Doorn, and J. P. Woerdman, "Electro-optic effect and birefringence in semiconductor vertical-cavity lasers," Phys. Rev. A **56**, 845-853 (1997).

85. D. W. Winston, Simwindows, free software (http://www-ocs.colorado.edu/SimWindows/simwin.html), 1999.

86. K. Bondarczuk, P. J. Maguire, L. P. Barry, J. O'Dowd, W. H. Guo, M. Lynch, A. L. Bradley, J. F. Donegan, and H. Folliot, "Chromatic dispersion monitoring of 80-Gb/s OTDM data signal via two-photon absorption in a semiconductor microcavity," IEEE Photon. Technol. Lett. **19**, 21-23 (2007).

87. K. Bondarczuk, P. J. Maguire, L. P. Barry, J. O'Dowd, W. H. Guo, M. Lynch, A. L. Bradley, J. F. Donegan, and H. Folliot, "Wavelength tuneable pulse monitoring using a Two-Photon-Absorption microcavity," in *Lasers and Electro-Optics, and the International Quantum Electronics Conference. CLEOE-IQEC. European Conference on*, 2007), 1-1.

88. K. Asahi, M. Yamashita, T. Hosoi, K. Nakaya, C. Konishi, and S. Fujita, "Optical performance monitor built into EDFA repeaters for WDM networks," in *Optical Fiber Communication Conference and Exhibit, 1998. OFC '98., Technical Digest*, 1998), 318-319.

89. L. Mei, J. P. Graeme, and J. E. Rob, "Extracting OSNR From Low-Resolution Optical Channel Monitors," IEEE Photon. Technol. Lett. **19**, 303-305 (2007).

90. D. C. Kilper, S. Chandrasekhar, L. Buhl, A. Agarwal, and D. Maywar, "Spectral Monitoring of OSNR in High-Speed Networks," in *Optical Communication. ECOC. 28th European Conference on*, 2002), 1-2.

91. N. A. Olsson, "Lightwave Systems With Optical Amplifiers," J. Lightwave Technol. **7**, 1071-1082 (1989).

92. T. Krug, W. H. Guo, J. O'Dowd, M. Lynch, A. L. Bradley, J. F. Donegan, P. J. Maguire, L. P. Barry, and H. Folliot, "Resonance tuning of two-photon absorption microcavities for wavelength-selective pulse monitoring," IEEE Photon. Technol. Lett. **18**, 433-435 (2006).

93. B. Pezeshki, A. Mathur, S. Zou, H. S. A. J. H. S. Jeon, V. A. A. V. Agrawal, and R. L. A. L. R. L. Lang, "12 nm tunable WDM source using an integrated laser array," Electron. Lett. **36**, 788-789 (2000).

94. J. O'Dowd, W. H. Guo, E. Flood, M. Lynch, A. L. Bradley, J. F. Donegan, and L. P. Barry, "Temperature tuning of two-photon absorption microcavity photodetectors for wavelength selective pulse monitoring," Electron. Lett. **44**, 989-991 (2008).

95. S. Imoto, N. Sako, Y. Tanaka, and T. A. K. T. Kurokawa, "Accuracy improvement of two-photon absorption based measurement by temperature controlled Si-photodetector," in *Lasers and Electro-Optics. CLEO/Pacific Rim. The 5th Pacific Rim Conference on*, 2003), 396 vol.392.

96. N. M. Margalit, K. A. Black, Y. J. Chiu, E. R. Hegblom, K. Streubel, P. Abraham, M. Anzlowar, J. E. Bowers, and E. L. Hu, "Top-emitting double-fused 1.5 μm vertical cavity lasers," Electron. Lett. **34**, 285-287 (1998).

97. T. Krug, M. Lynch, A. L. Bradley, J. F. Donegan, L. P. Barry, H. Folliot, J. S. Roberts, and G. Hill, "High-Sensitivity Two-Photon Absorption Microcavity Autocorrelator," IEEE Photon. Technol. Lett. **16**, 1543-1545 (2004).

98. D. Sun, W. Fan, P. Kner, J. Boucart, T. Kageyama, R. Pathak, D. Zhang, W. Yuen, and F. Bandwidth, "Sub-mA threshold 1.5-μm VCSELs with epitaxial and dielectric DBR mirrors," IEEE Photon. Technol. Lett. **15**, 1677-1679 (2003).

99. J. Goldstone and E. Garmire, "On the dynamic response of nonlinear Fabry-Perot interferometers," IEEE J. Quantum Electron **17**, 366-374 (1981).

100. S. Cova, M. Ghioni, A. Lotito, I. Rech, and F. Zappa, "Evolution and prospects for single-photon avalanche diodes and quenching circuits," Journal of Modern Optics **51**, 1267-1288 (2004).

101. R. Claps, D. Dimitropoulos, V. Raghunathan, Y. Han, and B. Jalali, "Observation of stimulated Raman amplification in silicon waveguides," Opt. Express **11**, 1731-1739 (2003).

102. K. Kikuchi, "Highly sensitive interferometric autocorrelator using Si avalanche photodiode as two-photon absorber," Electron. Lett. **34**, 123-125 (1998).

103. C. J. Chang-Hasnain, J. P. Harbison, C. E. Zah, M. W. Maeda, L. T. Florez, N. G. Stoffel, and T. P. Lee, "Multiple wavelength tunable surface-emitting laser arrays," IEEE J. Quantum Electron **27**, 1368-1376 (1991).